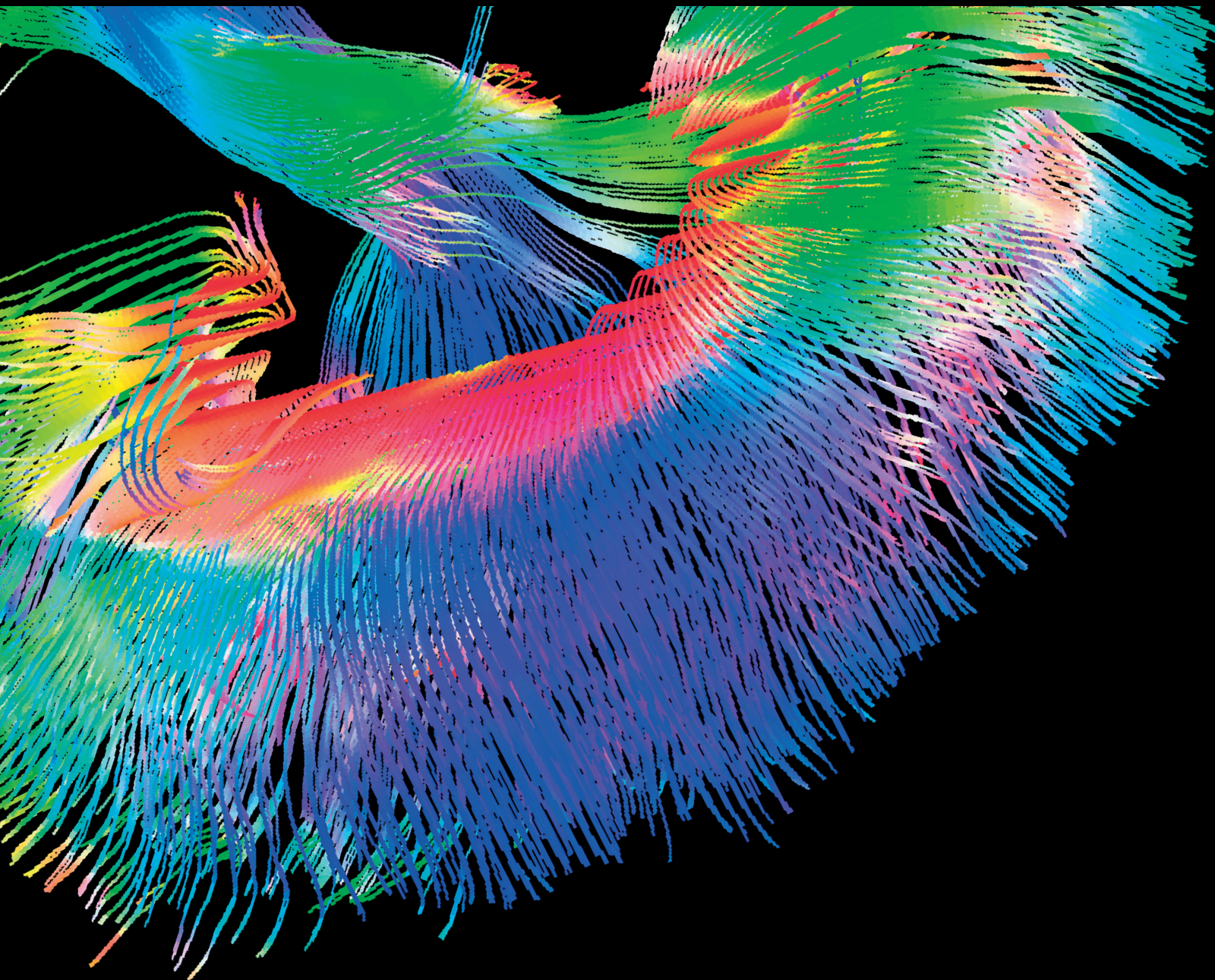


# In Vivo Imaging of Inflammation and Infection 2019

Special Issue Editor in Chief: Anne Roivainen

Guest Editors: Xiang-Guo Li, Sarah Ohrndorf, and Conny J. van der Laken





---

**In Vivo Imaging of Inflammation and Infection  
2019**

Contrast Media & Molecular Imaging

---

**In Vivo Imaging of Inflammation and Infection  
2019**

Special Issue Editor in Chief: Anne Roivainen

Guest Editors: Xiang-Guo Li, Sarah Ohrndorf, and Conny J.  
van der Laken



---

Copyright © 2020 Hindawi Limited. All rights reserved.

This is a special issue published in "Contrast Media & Molecular Imaging." All articles are open access articles distributed under the Creative Commons Attribution License, which permits unrestricted use, distribution, and reproduction in any medium, provided the original work is properly cited.

# Chief Editor

Luc Zimmer, France

---

## Editorial Board

Ali Azhdarinia, USA  
Peter Bannas, Germany  
Giorgio Biasiotto, Italy  
André L. B. de Barros, Brazil  
Dinesh K. Deelchand, USA  
Paul Edison, United Kingdom  
Michael J. Evans, USA  
Samer Ezziddin, Germany  
Guillermina Ferro-Flores, Mexico  
Luca Filippi, Italy  
Filippo Galli, Italy  
María L. García-Martín, Spain  
Alexander R. Haug, Germany  
Hao Hong, USA  
Alexey P. Kostikov, Canada  
Françoise Kraeber-Bodéré, France  
Kuo-Shyan Lin, Canada  
Gaurav Malviya, United Kingdom  
Barbara Palumbo, Italy  
Giancarlo Pascali, Australia  
Maria Joao Ribeiro, France  
Laurent M. Riou, France  
Anne Roivainen, Finland  
Pedro Rosa-Neto, Canada  
Barbara Salvatore, Italy  
Ralf Schirmacher, Canada  
Enza Torino, Italy  
Giorgio Treglia, Switzerland  
Reza Vali, Canada  
Mattia Veronese, United Kingdom  
Changning Wang, USA  
Habib Zaidi, Switzerland

## Contents

### **In Vivo Imaging of Inflammation and Infection 2019**

Anne Roivainen , Xiang-Guo Li , Sarah Ohrndorf, and Conny J. van der Laken   
Editorial (2 pages), Article ID 6824583, Volume 2020 (2020)

### **Radiolabeled Cationic Peptides for Targeted Imaging of Infection**

Tolulope A. Aweda , Zumrut F. B. Muftuler , Adriana V. F. Massicano , Dhruval Gadhia , Kelly A. McCarthy , Stacy Queern, Anupam Bandyopadhyay, Jianmin Gao , and Suzanne E. Lapi   
Research Article (11 pages), Article ID 3149249, Volume 2019 (2019)

### **The Clinical Impact of Using 18F-FDG-PET/CT in the Diagnosis of Suspected Vasculitis: The Effect of Dose and Timing of Glucocorticoid Treatment**

Kirsi Taimen , Soile P. Salomäki, Ulla Hohenthal, Markku Mali, Sami Kajander, Marko Seppänen, Pirjo Nuutila, Antti Palomäki, Anne Roivainen , Laura Pirilä, and Jukka Kemppainen  
Clinical Study (8 pages), Article ID 9157637, Volume 2019 (2019)

### **Diagnostic Performance of 18F-FDG PET/CT in Infectious and Inflammatory Diseases according to Published Meta-Analyses**

Giorgio Treglia   
Review Article (12 pages), Article ID 3018349, Volume 2019 (2019)

### **Neutrophil Elastase Activity Imaging: Recent Approaches in the Design and Applications of Activity-Based Probes and Substrate-Based Probes**

Natacha Jugniot, Pierre Voisin, Abderrazzak Bentaher, and Philippe Mellet   
Review Article (12 pages), Article ID 7417192, Volume 2019 (2019)

### **Renal Allograft Rejection: Noninvasive Ultrasound- and MRI-Based Diagnostics**

Ulrich Jehn , Katharina Schuette-Nuetgen, Dominik Kentrup, Verena Hoerr, and Stefan Reuter   
Review Article (9 pages), Article ID 3568067, Volume 2019 (2019)

### **Comparative Evaluation of 68Ga-Citrate PET/CT and 18F-FDG PET/CT in the Diagnosis of Type II Collagen-Induced Arthritis in Rats**

Zi Wang , Liang Cai, Tingting Xu, Dan Tang, Lin Liu, and Yue Chen   
Research Article (8 pages), Article ID 2353658, Volume 2019 (2019)

### **Dynamic Contrast-Enhanced MR with Quantitative Perfusion Analysis of Small Bowel in Vascular Assessment between Inflammatory and Fibrotic Lesions in Crohn's Disease: A Feasibility Study**

Davide Ippolito , Sophie Lombardi, Cammillo Talei Franzesi, Silvia Girolama Drago, Giulia Querques, Alessandra Casiraghi, Anna Pecorelli, Luca Riva, and Sandro Sironi  
Research Article (12 pages), Article ID 1767620, Volume 2019 (2019)

## Editorial

# In Vivo Imaging of Inflammation and Infection 2019

**Anne Roivainen** <sup>1,2,3</sup> **Xiang-Guo Li** <sup>1,4</sup> **Sarah Ohrndorf**<sup>5</sup> and **Conny J. van der Laken** <sup>6</sup>

<sup>1</sup>Turku PET Centre, University of Turku, FI-20521 Turku, Finland

<sup>2</sup>Turku PET Centre, Turku University Hospital, FI-20521 Turku, Finland

<sup>3</sup>Turku Center for Disease Modeling, University of Turku, FI-20521 Turku, Finland

<sup>4</sup>Turku PET Centre, Åbo Akademi University, FI-20521 Turku, Finland

<sup>5</sup>Charité – Universitätsmedizin, Berlin, Germany

<sup>6</sup>Department of Rheumatology, Amsterdam University Medical Center Location VU University Medical Center, Amsterdam, Netherlands

Correspondence should be addressed to Anne Roivainen; [anne.roivainen@utu.fi](mailto:anne.roivainen@utu.fi)

Received 20 January 2020; Accepted 21 January 2020; Published 11 February 2020

Copyright © 2020 Anne Roivainen et al. This is an open access article distributed under the Creative Commons Attribution License, which permits unrestricted use, distribution, and reproduction in any medium, provided the original work is properly cited.

Inflammation is involved in a number of medical conditions, and imaging-based diagnosis is frequently used for timely identification and localization of inflammatory foci. Inflammation is closely related to infection, and it is necessary to take inflammation into account in the imaging process of infection. Conventional imaging techniques (computed tomography, magnetic resonance imaging, and ultrasound) may detect such pathology but mainly rely on anatomical changes and are not fully capable of discriminating active inflammatory pathology from the anatomical changes resulting from prior successful therapy or surgery. In addition, inflammatory foci cannot be detected in the early phase of development because of the lack of substantial anatomical changes at this time. Nuclear imaging with radiotracers that accumulate at the site of inflammation has become an established tool in the evaluation of several inflammatory and infectious conditions. They can reveal molecular and cellular changes and provide sensitive detection of even small inflammatory and/or infectious foci at an early stage of disease.

This special issue consists of totally seven articles (72 pages) including three review articles, three research articles, and one clinical study. Although most of the articles are dealing with positron emission tomography/computed tomography (PET/CT) (four articles), magnetic resonance imaging (MRI, two articles) and ultrasound, as well as optical imaging techniques are discussed. The contents of

this special issue cover from early phases of ligand design, chemistry development, and preclinical evaluations to clinical imaging protocols and techniques.

Because during inflammation glucose consumption is raised due to active inflammatory cells, such as macrophages, and rapidly proliferating healing tissues, glucose analog 2-deoxy-2-[<sup>18</sup>F]fluoroglucose (<sup>18</sup>F-FDG) facilitates PET imaging of inflammation. <sup>18</sup>F-FDG is very sensitive and useful to detect both acute and chronic inflammation although it is not an inflammation-specific agent. The clinical study by K. Taimen et al. “The Clinical Impact of Using <sup>18</sup>F-FDG-PET/CT in the Diagnosis of Suspected Vasculitis: The Effect of Dose and Timing of Glucocorticoid Treatment” pointed at a clinically relevant issue of the impact of timing and dose of glucocorticoids on the diagnostic value of <sup>18</sup>F-FDG-PET/CT for large vessel vasculitis. They demonstrated that <sup>18</sup>F-FDG-PET/CT positivity of large vessels was significantly associated with a lower dose and shorter duration of glucocorticoid medication and higher CRP level in vasculitis patients. The review article by G. Treglia “Diagnostic Performance of <sup>18</sup>F-FDG PET/CT in Infectious and Inflammatory Diseases according to Published Meta-Analyses” presents on the basis of the current evidence—taking 36 meta-analyses into account—a good diagnostic performance of <sup>18</sup>F-FDG PET/CT for several inflammatory and infectious diseases, in particular, cardiovascular infectious and inflammatory diseases and some musculoskeletal

infections. In future, more prospective multicenter studies and cost-effective analyses are warranted. Although  $^{67}\text{Ga}$ -citrate has been used for decades in single-photon emission computed tomography (SPECT) imaging of inflammation, it has largely been replaced by  $^{18}\text{F}$ -FDG PET. However, positron-emitting analog  $^{68}\text{Ga}$ -citrate may also be useful in certain indications. The research article by Z. Wang et al. "Comparative Evaluation of  $^{68}\text{Ga}$ -Citrate PET/CT and  $^{18}\text{F}$ -FDG PET/CT in the Diagnosis of Type II Collagen-Induced Arthritis in Rats" suggests that  $^{68}\text{Ga}$ -citrate PET/CT may be helpful for detecting inflammatory activity of affected joints, e.g., in patients with rheumatoid arthritis.

It is very important to distinguish between infection and sterile inflammation although there are always inflammatory components also in the infection. Novel imaging agents are being developed in order to distinguish infection and inflammation. The research article by T. A. Aweda et al. "Radiolabeled Cationic Peptides for Targeted Imaging of Infection" has described a bacterial membrane targeting strategy with peptide-based imaging ligands. For example, in the structure of one of the ligands, an unnatural amino acid AB1 has been used to form covalent bonds with the amino group containing bacterial membrane lipids.

The review article by N. Jugniot et al. "Neutrophil Elastase Activity Imaging: Recent Approaches in the Design and Applications of Activity-Based Probes and Substrate-Based Probes" describes the recent progress of ligand development for imaging neutrophil elastase activity. The protease neutrophil elastase has a role in diseases including lung inflammation. The imaging probes are designed based on the corresponding mechanisms of enzyme-ligand interactions for imaging with different modalities.

The article by U. Jehn et al. "Renal Allograft Rejection: Noninvasive Ultrasound- and MRI-Based Diagnostics" reviews the current state-of-the-art approaches for noninvasive diagnostics of acute renal transplant inflammation, i.e., rejection, especially focusing on nonradiation-based methods using MRI and ultrasound. Another MRI-related paper, the research article by D. Ippolito et al. "Dynamic Contrast-Enhanced MR with Quantitative Perfusion Analysis of Small Bowel in Vascular Assessment between Inflammatory and Fibrotic Lesions in Crohn's Disease: A Feasibility Study" suggests that functional MRI with quantitative and semiquantitative measurements may represent a complementary diagnostic tool for evaluation of local inflammation activity in patients with Crohn's disease.

This special issue presents novel imaging probes, pre-clinical imaging evidences, and clinical applications of imaging-based diagnosis in inflammatory and infectious conditions, in addition to comprehensive, systematic, but concise overviews in this field. We hope that this issue will serve as a small forum in this specific field, and further research will be carried out in the research community.

## Conflicts of Interest

The editors declare that they have no conflicts of interest regarding the publication of the special issue.

## Acknowledgments

We would like to thank all the authors for their excellent contributions and the reviewers for their kind co-operation and critical comments in achieving this special issue.

Anne Roivainen  
Xiang-Guo Li  
Sarah Ohrndorf  
Conny J. van der Laken

## Research Article

# Radiolabeled Cationic Peptides for Targeted Imaging of Infection

Tolulope A. Aweda <sup>1</sup>, Zumurat F. B. Muftuler <sup>2</sup>, Adriana V. F. Massicano <sup>1</sup>,  
Dhruval Gadhia <sup>1</sup>, Kelly A. McCarthy <sup>3</sup>, Stacy Queern,<sup>1</sup> Anupam Bandyopadhyay,<sup>4</sup>  
Jianmin Gao <sup>3</sup> and Suzanne E. Lapi <sup>1</sup>

<sup>1</sup>Department of Radiology, University of Alabama at Birmingham, Birmingham, AL, USA

<sup>2</sup>Institute of Nuclear Sciences, The University of Ege at Izmir, Izmir, Turkey

<sup>3</sup>Department of Chemistry, Boston College, Chestnut Hill, Newton, MA 02467, USA

<sup>4</sup>Department of Chemistry, Indian Institute of Technology, Ropar, Punjab, India

Correspondence should be addressed to Suzanne E. Lapi; [lapi@uab.edu](mailto:lapi@uab.edu)

Received 23 February 2019; Revised 20 May 2019; Accepted 16 June 2019; Published 29 October 2019

Guest Editor: Xiang-Guo Li

Copyright © 2019 Tolulope A. Aweda et al. This is an open access article distributed under the Creative Commons Attribution License, which permits unrestricted use, distribution, and reproduction in any medium, provided the original work is properly cited.

Molecular probes targeting bacteria provide opportunities to target bacterial infections in vivo for both imaging and therapy. In the current study, we report the development of positron emission tomography (PET) probes for imaging of live bacterial infection based on the small molecules HLys-DOTA, a polycationic peptide synthesized as the D-isomer (RYWVAWRNRG) conjugated to 1, 4, 7, 10-tetraazacyclododecane-N',N'',N''',N-tetraacetic acid (DOTA) and AB1-HLys-DOTA, which includes an unnatural amino acid AB1 that preferentially binds to bacteria membrane lipids with amine groups via formation of imino-boronates. HLys-DOTA and AB1-HLys-DOTA peptides were radiolabeled with <sup>64</sup>Cu and investigated as PET imaging agents to track bacterial infection in vitro and in intramuscularly infected (IM) mice models. Cell uptake studies at 37°C in *Staphylococcus aureus* (SA) show higher uptake of <sup>64</sup>Cu-AB1-HLys-DOTA; 98.47 ± 3.54% vs <sup>64</sup>Cu-HLys-DOTA; 39.12 ± 3.27% at 24 h. Standard uptake values (SUV) analysis of the PET images resulted in mean SUV of 0.70 ± 0.08, 0.49 ± 0.04, and 0.31 ± 0.01 for <sup>64</sup>Cu-AB1-HLys-DOTA and 0.17 ± 0.06, 0.16 ± 0.02, and 0.13 ± 0.01 for <sup>64</sup>Cu-HLys-DOTA at 1, 4, and 24 h post injection, respectively, in the infected muscles. Similarly, in the biodistribution studies, dose uptake in the infected muscles was 4 times higher in the targeted <sup>64</sup>Cu-AB1-HLys-DOTA group than in the <sup>64</sup>Cu-HLys-DOTA group and 2-3 times higher than in the PBS control group at 1, 4, and 24 h post injection. <sup>64</sup>Cu-AB1-HLys-DOTA was able to distinguish between SA-infected muscle and *Pseudomonas aeruginosa* (PA) infected muscle with lower mean SUV of 0.28 ± 0.10 at 1 h post injection. This illustrates the utility of the AB1 covalently targeting group in synergy with the HLys peptide, which noncovalently binds to bacterial membranes. These results suggest that <sup>64</sup>Cu-labeled AB1-HLys-DOTA peptide could be used as an imaging probe for detection of bacterial infection in vivo with specificity for Gram-positive bacteria.

## 1. Introduction

Infectious diseases are one of the top ten leading causes of death in the world and the number one cause of death in low-income developing countries. Current diagnostic methods for bacterial infections are time-consuming as they require samples from the patient to be cultured for hours to weeks before enough bacteria are isolated to run destructive diagnostic tests [1, 2]. As proper identification of the disease often requires long diagnostic processes and bacterial infections tend to progress rapidly, fast diagnostic techniques

would allow physicians to identify what types of antimicrobial therapy may help a patient in a clinically relevant timeframe. The ability to image bacterial disease would permit rapid and specific diagnosis of infection. In addition, the ability to image infections would allow clinicians to determine whether a therapy is effective and to monitor patient response to therapy.

Recently, there has been an increase in research into noninvasive imaging of bacterial infection using PET/CT, SPECT, MRI, and other imaging modalities in preclinical studies of infectious diseases using natural and synthetic

molecules [3]. The use of radionuclides for detecting and localizing infection has been employed for decades [4, 5]. Ideally, the radiopharmaceutical for detecting infection should be specific, sensitive, and clear from the body rapidly to facilitate early image acquisition and clear delineation of the infected area. These radionuclides have been utilized as salts or small molecules such as  $^{99m}\text{Tc}$ -methylene diphosphonate,  $^{67}\text{Ga}$ -citrate, and  $^{18}\text{F}$ -FDG [6–10].  $^{111}\text{In}$ -oxine and  $^{99m}\text{Tc}$ -exametazime have also been used to label leukocytes for imaging in diagnosis of infection [7, 11, 12]. This approach, though valuable, has some drawbacks, requiring high levels of leukocytes, and detection of non-infectious inflammations and is thus not specific to the infection or bacteria [13, 14].

Another radioisotope of interest is  $^{68}\text{Ga}$ , with a shorter half-life of 68 min compared to its counterpart  $^{67}\text{Ga}$ : half-life of 78.3 h (used in SPECT), has undergone an increased utilization in preclinical and clinical PET imaging particularly in oncology. Although, [ $^{68}\text{Ga}$ ]citrate PET-CT of bone and joint infection offered lower radiation dose, as well as earlier and shorter imaging times, and its sensitivity and specificity was found to be lower than [ $^{67}\text{Ga}$ ]citrate [15]. In other infection and inflammation imaging studies,  $^{68}\text{Ga}$  has been used to radiolabel ligands, small molecules, and peptides to target a host of receptors, inhibitors, leukocytes, and pathways [16].  $^{68}\text{Ga}$ -apo-transferrin ([ $^{68}\text{Ga}$ ]TF) has been used to image *Staphylococcus aureus* (SA) and found to detect the infected lesions better than [ $^{68}\text{Ga}$ ]Cl<sub>3</sub>; additionally, [ $^{68}\text{Ga}$ ]TF was also found to detect the Gram-negative bacteria, *Proteus mirabilis* [17]. In other studies, the antibiotic ciprofloxacin was labeled with  $^{68}\text{Ga}$  and used to distinguish inflamed muscle from SA-infected muscle [18].

The use of  $^{64}\text{Cu}$  radioisotope for imaging purposes has increased over the years, and several studies have utilized this isotope to label compounds for detecting regions of infection [19]. In order to label these compounds, several suitable chelators for  $^{64}\text{Cu}$  have been developed with significant progress over the years; these chelates range from acyclic to cage-like bifunctional chelators [20, 21].  $^{64}\text{Cu}$ , with its relatively long half-life (12.7 hours) compared to  $^{18}\text{F}$  or  $^{99m}\text{Tc}$  has been used to label peptides, antibody fragments, and whole antibodies for imaging [22]. For instance, necrotic pulmonary tuberculosis lesions in chronically infected mice were detected and demonstrated to be hypoxic using  $^{64}\text{Cu}$ (II)-diacetyl-bis( $\text{N}^4$ -methyl-thiosemicarbazone), [ $^{64}\text{Cu}$ ]ATSM [23]. In mice models of *S. aureus* endocarditis (heart valve infection), robust localization of [ $^{64}\text{Cu}$ ]DTPA-prothrombin was used to noninvasively detect infection lesions as compared to the bacteria-free control mice, which had no accumulation at the site of endothelial trauma [24].

Radiolabeled molecular probes specifically targeting bacterial lipids provide opportunities to target bacterial infections in vivo for both imaging and therapy. In this study, synthetic peptides that preferentially bind to bacterial surfaces with amine-presenting lipids were radiolabeled and studied in vitro and in vivo. Two phospholipids abundant on Gram-positive bacteria, phosphatidylethanolamine (PE) and lysylphosphatidylglycerol (Lys-PG), were targeted for recognition by appropriately constructed short peptides used as

low molecular weight probes [25]. For our studies, the D-isomer of a polycationic peptide HLys (RYW-VAWRNRG), which binds noncovalently to bacteria surfaces, was conjugated to 1, 4, 7, 10-tetraazacyclododecane- $\text{N}'$ ,  $\text{N}''$ ,  $\text{N}'''$ , N-tetraacetic acid (DOTA) to make HLys-DOTA. To improve the binding of the peptide to the bacterial surface, an unnatural amino acid AB1, which preferentially binds covalently to lipids with amine groups via formation of iminoboronates under physiological conditions, was conjugated to HLys-DOTA, as shown in Figure 1 [26]. By targeting PE and Lys-PG with AB1, the iminoboronate chemistry allows potent labeling of Gram-positive bacteria such as *Staphylococcus aureus* (SA) even in the presence of serum proteins, while bypassing mammalian cells and Gram-negative bacteria [26]. HLys-DOTA and AB1-HLys-DOTA peptide conjugates were radiolabeled with  $^{64}\text{Cu}$  and studied as PET imaging agents to track bacterial infection in vitro and in intramuscularly infected (IM) mice models.

## 2. Materials and Methods

$^{64}\text{Cu}$  was produced in-house on an ACSI TR-24 Cyclotron (Richmond, Canada) located in the UAB Cyclotron facility. 2-deoxy-2-[ $^{18}\text{F}$ ]fluoro-d-glucose ([ $^{18}\text{F}$ ]FDG) was purchased from PETNET (Birmingham, AL). All solvents and reagents were obtained from Sigma-Aldrich Company unless otherwise specified. *Staphylococcus aureus* (SA), ATCC 6538, and *Pseudomonas aeruginosa* (PA), ATCC 47085, were purchased from ATCC (Manassas, VA), and Whatman 3 M silica gel thin-layer chromatography (TLC) plates were purchased from Fisher Scientific (Pittsburgh, PA). Diethylenetriaminepentaacetic acid (DTPA) was purchased from Sigma (St. Louis, MO). 1,4,7,10-Tetraazacyclododecane-1,4,7,10-tetraacetic acid mono-N-hydroxysuccinimide ester (DOTA-NHS-ester) was purchased from MacroCyclics (Dallas, Texas). C18 SepPak cartridges were obtained from Waters Corporation (Milford, MA). Radiometric instant thin-layer chromatography measurements were accomplished using a TLC scanner (Bioscan AR-2000 Scanner). Reverse-phase chromatography analysis was performed on a C18 column (PA) with an infinity diode-array UV detector (Agilent, Lake Forest, CA) and a PMT/NaI remote radioactive detector (LabLogic Systems Ltd, Brandon, FL). Laura radiochromatography software (LabLogic Systems Ltd, Brandon, FL) was used to quantify chromatograms by integration. Radioactive samples were counted using a 2480 Wizard II automatic gamma counter (PerkinElmer, Downers Grove, IL). Imaging studies were done by using GNEXT PET-CT (Sofie BioSciences) [CT-80 Kvp, 5 min (approximately 100  $\mu\text{m}$ ), PET-Resolution  $\leq 1$  mm]. Acquired PET/CT images were analyzed with Inveon™ Research Workplace (IRW) (Siemens).

**2.1. Synthesis and Structural Analysis of HLys-DOTA and AB1-HLys-DOTA Peptides.** HLys-DOTA and AB1-HLys-DOTA were synthesized by following a previously described protocol for solid-phase peptide synthesis [26], and the

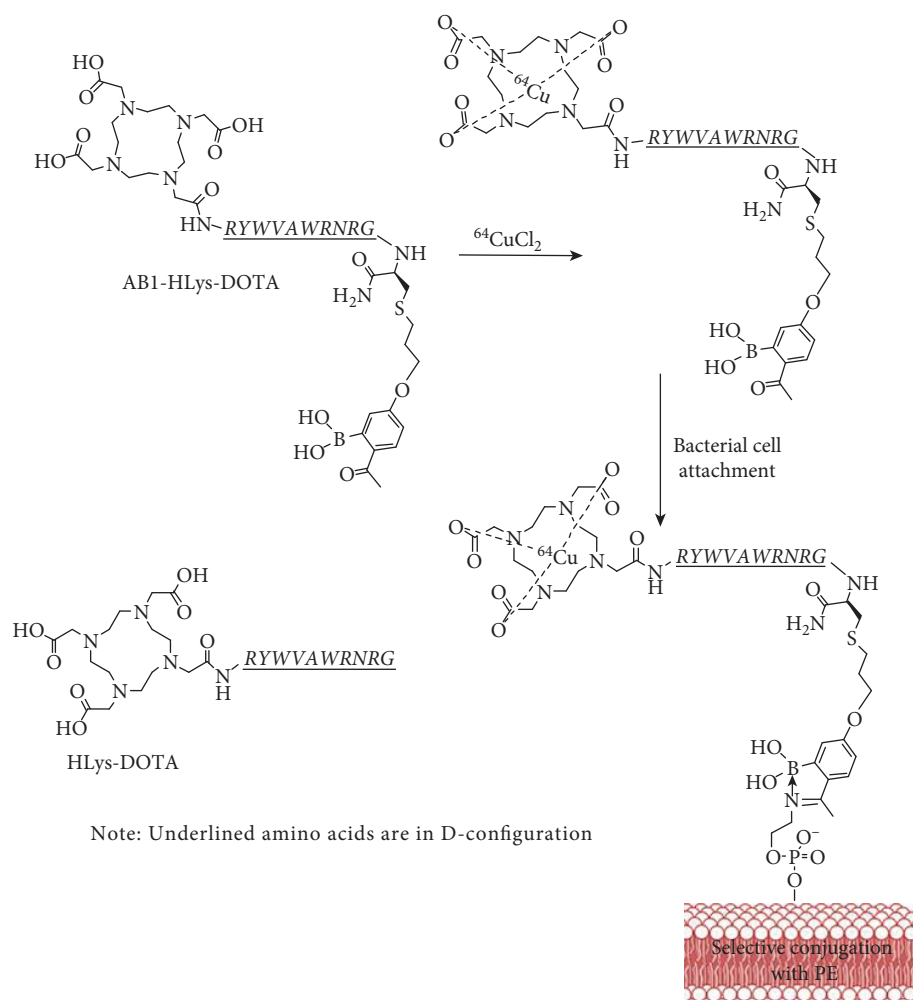


FIGURE 1: Illustration of  $^{64}\text{Cu}$ -radiolabeled AB1-HLys-DOTA peptide for targeting PE on bacterial cell surfaces.

DOTA moiety was conjugated to the N-terminus of peptides on resin using DOTA-NHS-ester as a precursor [27]. To ensure in vivo stability of the peptides, the D-isomer of all amino acids except AB1 was used for peptide synthesis. Literature reports have shown that the D-isomers of antimicrobial peptides behave similarly to their L-counterparts in bacterial binding [28]. The peptides were purified using HPLC, and their purity and integrity was confirmed by LC-MS (Supporting Information Figure 1).

**2.2. Production of  $^{64}\text{Cu}$ .**  $^{64}\text{Cu}$  ( $t_{1/2}=12.7$  h,  $\beta^+=17\%$ ,  $\beta^-=39\%$ ,  $EC=43\%$ ,  $E_{\text{max}}=0.656$  MeV) was produced in-house at the University of Alabama at Birmingham Cyclotron facility via the  $^{64}\text{Ni}(p,n)^{64}\text{Cu}$  nuclear reaction. Production and purification of  $^{64}\text{Cu}$  was conducted using modified methods from literature [29, 30] via bombardment of enriched  $^{64}\text{Ni}$  targets at  $40\ \mu\text{A}$  with an incident proton beam of 19 MeV degraded to 12 MeV with a 1 mm Al degrader.

**2.3. Radiolabeling of HLys-DOTA and AB1-HLys-DOTA Peptides.** The two peptides, HLys-DOTA and AB1-HLys-DOTA, were radiolabeled with  $^{64}\text{CuCl}_2$  buffered in 0.1 M

$\text{NH}_4\text{OAc}$ , pH 6, at  $56^\circ\text{C}$  according to modified previously published methods [31, 32]. Briefly, radiolabeling of the peptides was achieved by adding  $50\ \mu\text{g}$  of HLys-DOTA or AB1-HLys-DOTA into 120–130 MBq (3.2–3.5 mCi) of  $^{64}\text{CuCl}_2$  in  $1450\ \mu\text{L}$  of 0.1 M  $\text{NH}_4\text{OAc}$ , pH 6. The reactions were incubated on a mixer with 800 rpm agitation at  $56^\circ\text{C}$  for 45 min, and radiolabeling was also attempted at lower temperature. Radiolabeling yield and radiochemical purity were assessed using silica gel plates developed in 50:50 of methanol: 1 M ammonium acetate and high-performance liquid chromatography, respectively, with gradient: 0–12 min: 95% A to 20% A (A=water, 0.1% TFA, B=acetonitrile, 0.1% TFA), 12–15 min: 20% A to 95% A.  $^{64}\text{Cu}$ -AB1-HLys-DOTA was purified according to the Jacobson method [33]. A SepPak C18-cartridge was activated with 5 mL of ethanol and 10 mL of water. The reaction mixture of  $^{64}\text{Cu}$ -AB1-HLys-DOTA was diluted with 5 mL of water and loaded slowly onto the activated SepPak C18-cartridge using a syringe. The cartridge was washed with 10 mL of water followed by elution of the desired labeled peptide with 1 mL of 10 mM HCl in ethanol. The ethanol was evaporated, and the radiolabeled peptide was reformulated with saline.

**2.4. Serum Stability Studies.** An aliquot of 10  $\mu\text{L}$  of 3.3 MBq ( $\sim 90 \mu\text{Ci}$ ) of  $^{64}\text{Cu}$ -labeled AB1-HLys-DOTA compound was added to 90 mL of PBS, human serum (HSA), or mouse serum and incubated at 37°C with agitation (500 rpm) separately. Aliquots were removed at time points 0, 0.17, 1, 2, 4, and 24 h and analyzed using radio-TLC. All reactions were conducted in triplicate.

## 2.5. In Vitro Studies

**2.5.1. Bacterial Cell Culture.** Bacterial in vitro uptake and imaging experiments were performed using Gram-positive bacteria, *Staphylococcus aureus* (SA), and Gram-negative bacteria, *Pseudomonas aeruginosa* (PA), as control. Bacterial cells from a single colony were grown overnight in LB broth at 37°C with agitation until the cells reached the mid logarithmic phase ( $\text{OD}_{600} \sim 0.6\text{--}0.7$ ). For the in vitro experiments, 750–1000  $\mu\text{L}$  of the bacterial cell culture was spun down at 7000 rpm for 7 min in a 1.5 mL centrifuge tube.

**2.5.2. Uptake Studies of  $^{64}\text{Cu}$ -Labeled Peptides in *Staphylococcus aureus* (SA) and *Pseudomonas aeruginosa* (PA).** Bacteria cell uptake studies of  $^{64}\text{Cu}$ -HLys-DOTA and  $^{64}\text{Cu}$ -AB1-HLys-DOTA in SA and PA bacteria were performed at 37°C. LB broth was inoculated with SA or PA bacteria and after 18–22 hours, cells were harvested by spinning down and washing twice in 750–1000  $\mu\text{L}$  of PBS (50 mM sodium phosphate, pH = 7.4), and the  $\text{OD}_{600}$ ,  $\text{OD}_{230}$ , and  $\text{OD}_{260}$  determined. 750  $\mu\text{L}$  of the PBS suspended bacteria ( $0.9\text{--}1.3 \times 10^7$  CFU/mL) was incubated with 0.925–0.999 MBq (25–27  $\mu\text{Ci}$ ) of  $^{64}\text{Cu}$ -HLys-DOTA and  $^{64}\text{Cu}$ -AB1-HLys-DOTA at 37°C in triplicates at different time points: 5, 40, 60, 240, and 1440 min. At each time point, the mixture was spun down, washed twice with PBS, and the final bacterial pellets were measured using a gamma counter to determine the percent of associated radiolabeled peptide. Mammalian cell uptake was verified by following a similar procedure in a nonbacterial cell, SKBR3 breast cancer cell line.

**2.5.3. Small Animal Imaging and Biodistribution Studies.** All animal experiments were performed according to animal use protocols approved by the University of Alabama at Birmingham Institutional Animal Care and Use Committee (IACUC). Animals were housed under controlled conditions with a natural light-dark cycle. They were allowed to adapt to the housing environment for at least 48 h prior to study. Biodistribution and PET imaging studies with  $^{64}\text{Cu}$ -HLys-DOTA and  $^{64}\text{Cu}$ -AB1-HLys-DOTA were conducted in mice intramuscularly (IM) infected in the thigh muscle with SA and PBS as a control. Thirty-six male mice (25–30 g, 4–5 weeks old) infected with SA were used for animal studies. For each peptide, 4 mice were used for small animal PET imaging at 1, 4, and 24 h, and then sacrificed at 24 h for a post-PET biodistribution. Another set of 4 mice each was used for biodistribution studies at 1 and 4 h. A similar set of mice was used for blocking studies with  $^{64}\text{Cu}$ -AB1-HLys-DOTA peptide. In order to check the specificity of  $^{64}\text{Cu}$ -

AB1-HLys-DOTA for Gram-positive bacteria, imaging and post-PET biodistribution studies were conducted in another set of mice (four) intramuscularly (IM) infected in the thigh muscle with PA and PBS.

**2.5.4. Infection Animal Model.** Mice for infection studies were anesthetized prior to the intramuscular infection of SA or PA. Animals were immobilized with isoflurane. Bacteria cells concentrated in sterile PBS were injected into the thigh muscle and the site of injection pinched to minimize bleeding. SA or PA suspension (50  $\mu\text{L}$ ,  $2.6\text{--}2.8 \times 10^7$  CFU per mouse) was intramuscularly injected into the right thigh muscle, and sterile PBS (50  $\mu\text{L}$ ) was injected into the left thigh muscle as control. Mice were placed back into the cages and allowed to recover with frequent monitoring to identify any sign of extreme distress. The infection was allowed to develop for 3–5 days before intravenous injection of the radiolabeled probe. The muscles on the left and right thighs were harvested, homogenized, and plated on mannitol agar plates or cultured in LB broth to verify the presence of infection. In addition, [ $^{18}\text{F}$ ]FDG imaging was also performed in infected animal models as described in the PET imaging section below to further confirm the existence of infection in the right thigh and the absence thereof in the left thigh.

**2.5.5. Biodistribution Studies.** For biodistribution studies, 3.3–3.7 MBq (90–100  $\mu\text{Ci}$ ) of  $^{64}\text{Cu}$ -HLys-DOTA or  $^{64}\text{Cu}$ -AB1-HLys-DOTA was injected into prewarmed tail vein of the animals under anesthesia. Animals were euthanized at 1 and 4 h after radiotracer administration ( $n = 4$  for each tracer at each time point). At 24 h after small animal PET imaging, the mice were also euthanized for a post-PET biodistribution. In a similar set of experiment, excess of the unlabeled peptide, 150 nmol, was coinjected with the radiolabeled peptides per mouse. The organs of interest were collected, weighed, and measured for radioactivity content using a gamma counter. The data were background-corrected and decay-corrected. The biodistribution data were expressed as percentage of injected radioactive dose per gram of tissue (%ID/g) for selected organs as the mean value of four mice.

**2.5.6. PET/CT Imaging Studies.** Small animal PET/CT imaging studies were conducted in SA-infected and PA-infected animal models. Each radiolabeled peptide, 3.3–3.7 MBq (90–100  $\mu\text{Ci}$ ), was administered via tail vein injection of prewarmed mice under anesthesia. The inflammatory response caused by the infection was confirmed by intravenous injection of [ $^{18}\text{F}$ ]FDG, 3.7 MBq (100  $\mu\text{Ci}$ ), into mice infected on the right thigh muscle with SA or PA and on the left with PBS as control. For this small animal PET imaging, 1 and 4 h post-injection static scans were collected. Following imaging studies, the mice were sacrificed for biodistribution. Mice were allowed to recover from anesthesia until the time of imaging. Mice were anesthetized with 2–3% isoflurane/oxygen and imaged on the small animal PET/CT scanner. Static images were collected at 1, 4, and 24 h for 15, 20, and 30 min, respectively. PET images were coregistered with CT image for anatomical colocalization.

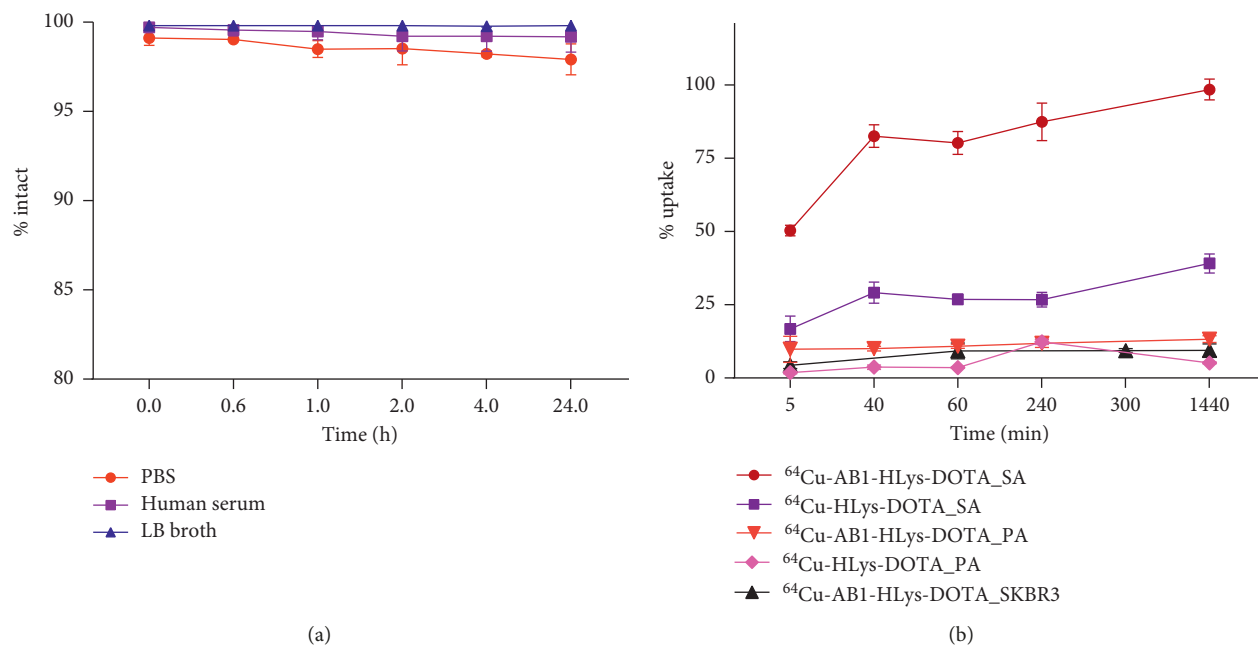


FIGURE 2: Stability of (a)  $^{64}\text{Cu}$ -AB1-HLys-DOTA in PBS, human serum, and LB broth at 0–24 h and 37°C. (b) Cell uptake of  $^{64}\text{Cu}$ -AB1-HLys-DOTA and  $^{64}\text{Cu}$ -HLys-DOTA peptides in *S. aureus* (SA) and *P. aeruginosa* (PA), and  $^{64}\text{Cu}$ -AB1-HLys-DOTA in mammalian SKBR3 cells.

Regions of interest (ROI) were manually drawn over organs of interest with CT anatomical guidelines, and the associated radioactivity was measured using Inveon Research Workstation software. Standard uptake values (SUV) were calculated as  $\text{nCi/cc} \times \text{animal weight/injected dose}$ , and comparisons in pharmacokinetics of radiolabeled peptides were assessed.

**2.6. Statistical Analysis.** Statistical calculations were carried out using Prism 7 (GraphPad Software) and expressed as mean  $\pm$  SD. One-way analysis of standard deviation at 95% confidence level ( $p < 0.05$ ) were considered statistically significant.

### 3. Results

**3.1. HLys-DOTA and AB1-HLys-DOTA Peptide Synthesis, Characterization, and Stability.** The analysis of HLys-DOTA and AB1-HLys-DOTA peptides was performed using LC-MS in positive mode  $[\text{M}+\text{H}]$  allowing detection of their corresponding molecular ion at  $m/z$  1691.92 and  $m/z$  2074.15, respectively [26]. HLys-DOTA and AB1-HLys-DOTA peptides were radiolabeled with  $^{64}\text{Cu}$  at molar activities of  $3873 \pm 398$  and  $3809 \pm 943$  MBq/ $\mu\text{mol}$  ( $105 \pm 11$  and  $103 \pm 25$  mCi/ $\mu\text{mol}$ ), respectively, at 56°C. Incubations at lower temperature resulted in lower yields (See Supporting Information Table 1 for radiolabeling kinetics). Radiochemical and labeling yield of  $^{64}\text{Cu}$ -HLys-DOTA was  $\geq 95\%$  after TLC and HPLC analysis but  $^{64}\text{Cu}$ -AB1-HLys-DOTA required purification through a C18 SepPak to achieve  $\geq 95\%$  radiochemical purity. The need for extra purification of  $^{64}\text{Cu}$ -AB1-HLys-DOTA in order to achieve  $\geq 95\%$  radiochemical purity could be due to the extra benzyl

group and the hydrophobic portion of AB1 preventing good complexation of radiocopper ions.

**3.2. Stability and In Vitro Cell Uptake Studies.** Excellent stability of  $^{64}\text{Cu}$ -AB1-HLys-DOTA was observed in the PBS, human serum, and LB broth with  $>98\%$  intact peptide observed at 24 h post incubation in all solutions, as shown in Figure 2(a). Bacteria cell uptake of  $^{64}\text{Cu}$ -AB1-HLys-DOTA conjugate at 37°C in *Staphylococcus aureus* (SA) was significantly higher than that of  $^{64}\text{Cu}$ -HLys-DOTA at all time points: 0.08, 0.67, 1, 4, and 24 h;  $98.5 \pm 3.5\%$  vs  $39.1 \pm 3.3\%$  at 24 h, Figure 2(b). Specific uptake in Gram-positive bacteria SA was confirmed by the lower uptake of the peptides in *Pseudomonas aeruginosa* (PA), a Gram-negative bacterium. At 5 min after incubation, the uptake of  $^{64}\text{Cu}$ -AB1-HLys-DOTA and  $^{64}\text{Cu}$ -HLys-DOTA showed  $9.8 \pm 4.4\%$  and  $1.9 \pm 0.4\%$  binding to PA, respectively, which increased slightly to  $13.3 \pm 1.1\%$  and  $5.2 \pm 0.3\%$ , respectively, at 24 h after incubation. This indicates a 5–10 times lower uptake of the peptides in PA as compared to SA confirming the specificity of AB1 for Gram-positive bacteria. Specific bacterial cell uptake was confirmed by the low uptake ( $9.4 \pm 2.3\%$ ) of  $^{64}\text{Cu}$ -AB1-HLys-DOTA in mammalian SKBR3 breast cancer cells at 24 h post incubation.

**3.3. Confirmation of Infection in Animal Model.** The development of infection was evident by presence of a palpable mass filled with abscess observed during dissection and harvesting. The infected muscle and control muscle were harvested, homogenized, and the CFU of bacteria counted. In the infected muscle,  $4.8 \pm 2.5 \times 10^6$  cfu/g of bacteria was found and only one

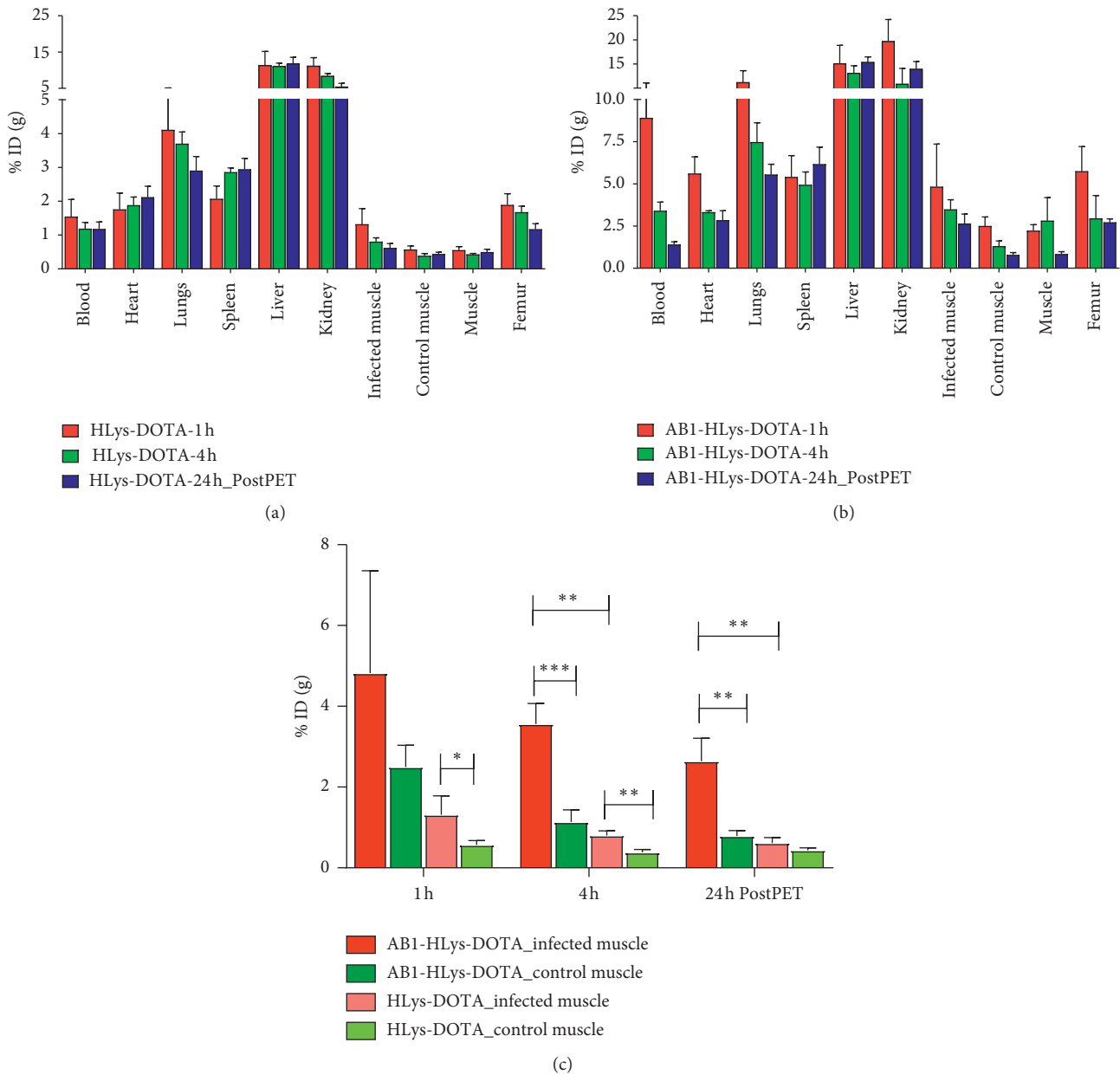


FIGURE 3: Biodistribution of (a)  $^{64}\text{Cu}$ -HLys-DOTA and (b)  $^{64}\text{Cu}$ -AB1-HLys-DOTA in intramuscularly infected mice model at 1, 4, and 24 h post injection. (c) Comparison of dose uptake of  $^{64}\text{Cu}$ -HLys-DOTA and  $^{64}\text{Cu}$ -AB1-HLys-DOTA in the infected and PBS-injected control muscle.  $n=4$  for each time point, \*, \*\*, and \*\*\* show significant statistical analysis at  $p < 0.05$ .

PBS-control muscle was positive with colony at  $1.8 \times 10^5$  cfu/g cfu. [ $^{18}\text{F}$ ]FDG in vivo characterization of the infection site verified high uptake in the SA-infected muscle versus the control muscle at 1 and 4 h post injection,  $p < 0.005$ .

**3.4. Biodistribution Studies.** The biodistribution and pharmacokinetics of the peptides  $^{64}\text{Cu}$ -AB1-HLys-DOTA and  $^{64}\text{Cu}$ -HLys-DOTA were assessed in mice intramuscularly infected with *S. aureus* on the right thigh muscle and PBS injected in the left thigh muscle as control. The biodistribution showed that the uptake of both peptides in the infected muscle was significantly higher than the PBS-

injected control muscle of the same mouse at all time points: 1, 4, and 24 h post injection, as shown in Figure 3. The uptake of  $^{64}\text{Cu}$ -AB1-HLys-DOTA conjugate in the infected thigh was 2-3 times higher than the control muscle at later time points, although no significant difference was observed at 1 h ( $4.8 \pm 2.5$  %ID/g vs.  $2.5 \pm 0.5$  %ID/g). At 4 h, the dose uptake of  $^{64}\text{Cu}$ -AB1-HLys-DOTA in the infected muscle was  $3.6 \pm 0.5$  %ID/g vs.  $1.1 \pm 0.4$  %ID/g in the control muscle,  $p < 0.0005$ . Similarly, at 24 h, the uptake of  $^{64}\text{Cu}$ -AB1-HLys-DOTA in the infected muscle was  $2.6 \pm 0.6$  %ID/g vs.  $0.8 \pm 0.1$  %ID/g in the control muscle,  $p < 0.005$ . In contrast, the dose accumulation of  $^{64}\text{Cu}$ -HLys-DOTA in the infected muscle was only 1- or 2-fold higher than the control muscle

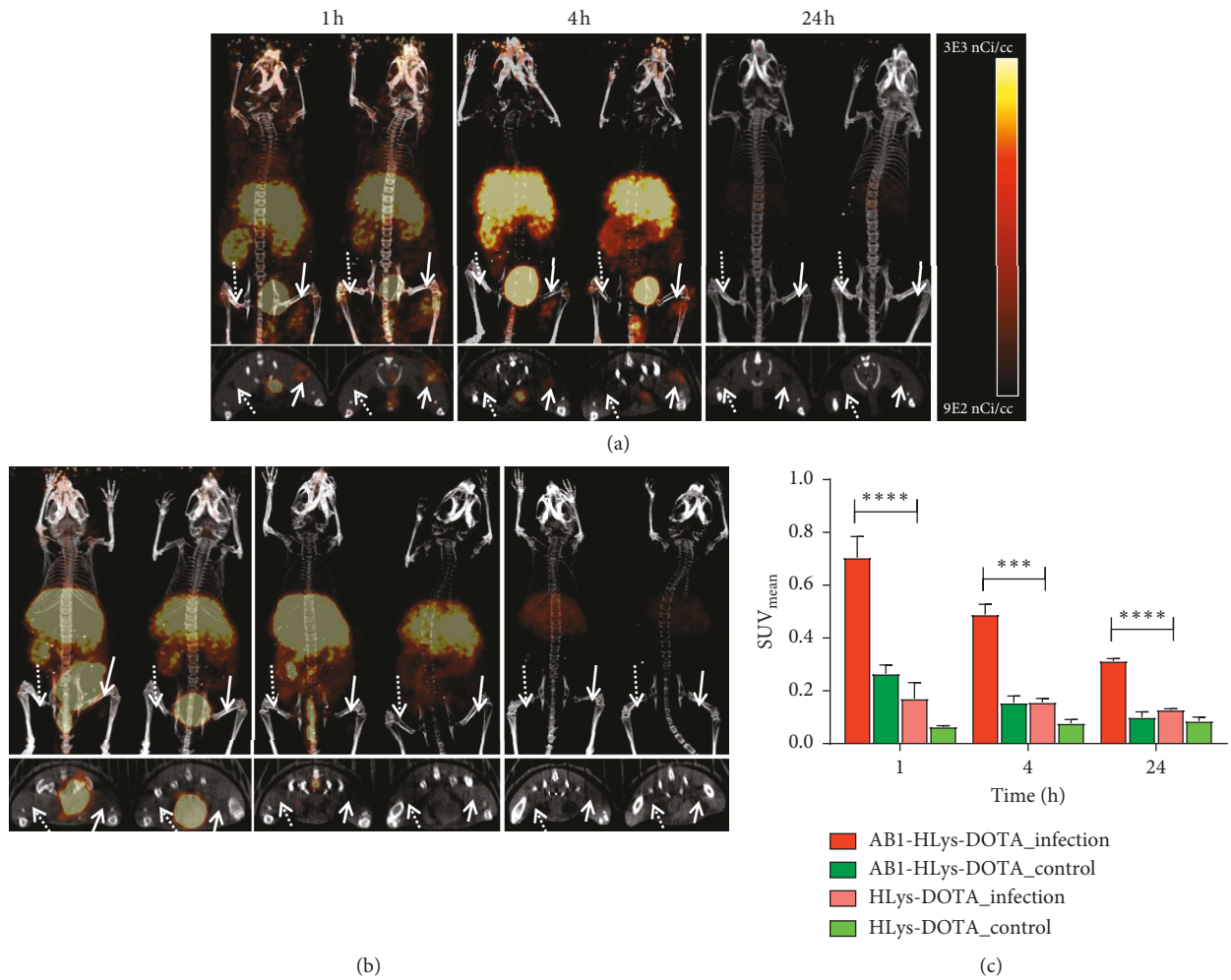


FIGURE 4: Small animal PET/CT images of (a)  $^{64}\text{Cu}$ -HLys-DOTA, (b)  $^{64}\text{Cu}$ -AB1-HLys-DOTA, and (c) mean SUV values calculated from infected and PBS-control muscle. Dashed arrow indicates the PBS-control muscle, and solid arrow indicates the infected right muscle.  $n = 4$  for each time point, \*\*\* and \*\*\*\* show significant statistical analysis at  $p < 0.0005$  and  $p < 0.0001$ , respectively.

in the same mouse, except at 24 h where no significant difference was observed between them. At 1 and 4 h, the uptake of  $^{64}\text{Cu}$ -HLys-DOTA in the infected muscle vs. control muscle was  $1.3 \pm 0.5\% \text{ID/g}$  vs.  $0.6 \pm 0.1\% \text{ID/g}$ ,  $p < 0.05$ , and  $0.8 \pm 0.1\% \text{ID/g}$  vs.  $0.4 \pm 0.1\% \text{ID/g}$ ,  $p < 0.005$ , respectively. We also observed that uptake in the infected muscle was 4 times higher in the targeted  $^{64}\text{Cu}$ -AB1-HLys-DOTA group compared to that in the  $^{64}\text{Cu}$ -HLys-DOTA group, as shown in Figure 3(c). The uptake of  $^{64}\text{Cu}$ -AB1-HLys-DOTA in the infected muscle was  $4.8 \pm 2.5$ ,  $3.6 \pm 0.5$ , and  $2.6 \pm 0.6\% \text{ID/g}$  vs.  $1.3 \pm 0.5$ ,  $0.8 \pm 0.1$ , and  $0.6 \pm 0.1\% \text{ID/g}$  for  $^{64}\text{Cu}$ -HLys-DOTA, respectively, at 1, 4, and 24 h post injection,  $p < 0.005$  at 4 and 24 h. The highest accumulation of the radiolabeled peptides was observed in the liver and kidney with  $^{64}\text{Cu}$ -AB1-HLys-DOTA also showing some uptake in the lungs.  $^{64}\text{Cu}$ -AB1-HLys-DOTA also showed higher retention in the blood and heart than  $^{64}\text{Cu}$ -HLys-DOTA at 1 and 4 h post injection but at 24 h, both peptides had similar activity in the blood. A similar experiment using an excess of the unlabeled peptides, 150 nmol, did not show a statistical difference (data not shown) in the uptake of the

peptides at the infection site. This may indicate that the binding sites at the bacterial surface cannot be saturated.

**3.5. PET/CT Imaging.** The uptake of  $^{64}\text{Cu}$ -AB1-HLys-DOTA in the infected muscle was visibly observed via small animal PET/CT imaging as early as 1 and 4 h post injection, Figure 4. The uptake in the infected muscle was higher in the PET images of  $^{64}\text{Cu}$ -AB1-HLys-DOTA than in the images of  $^{64}\text{Cu}$ -HLys-DOTA at 1 and 4 h post injection in agreement with the biodistribution data. SUV analysis of the PET images showed 2.4 to 4-fold increase in accumulation of  $^{64}\text{Cu}$ -AB1-HLys-DOTA vs.  $^{64}\text{Cu}$ -HLys-DOTA at the infection. The mean SUV of  $^{64}\text{Cu}$ -AB1-HLys-DOTA and  $^{64}\text{Cu}$ -HLys-DOTA in the infected muscle was  $0.70 \pm 0.08$  vs.  $0.17 \pm 0.06$ ,  $p < 0.0001$ ,  $0.49 \pm 0.04$  vs.  $0.16 \pm 0.02$ ,  $p < 0.0005$ , and  $0.31 \pm 0.01$  vs.  $0.13 \pm 0.01$ ,  $p < 0.0001$  at 1, 4, and 24 h post injection, respectively. There was no statistical difference between mean SUV uptake of  $^{64}\text{Cu}$ -HLys-DOTA in the infected muscle and  $^{64}\text{Cu}$ -AB1-HLys-DOTA uptake in the control muscles at all time points. This indicates  $^{64}\text{Cu}$ -HLys-

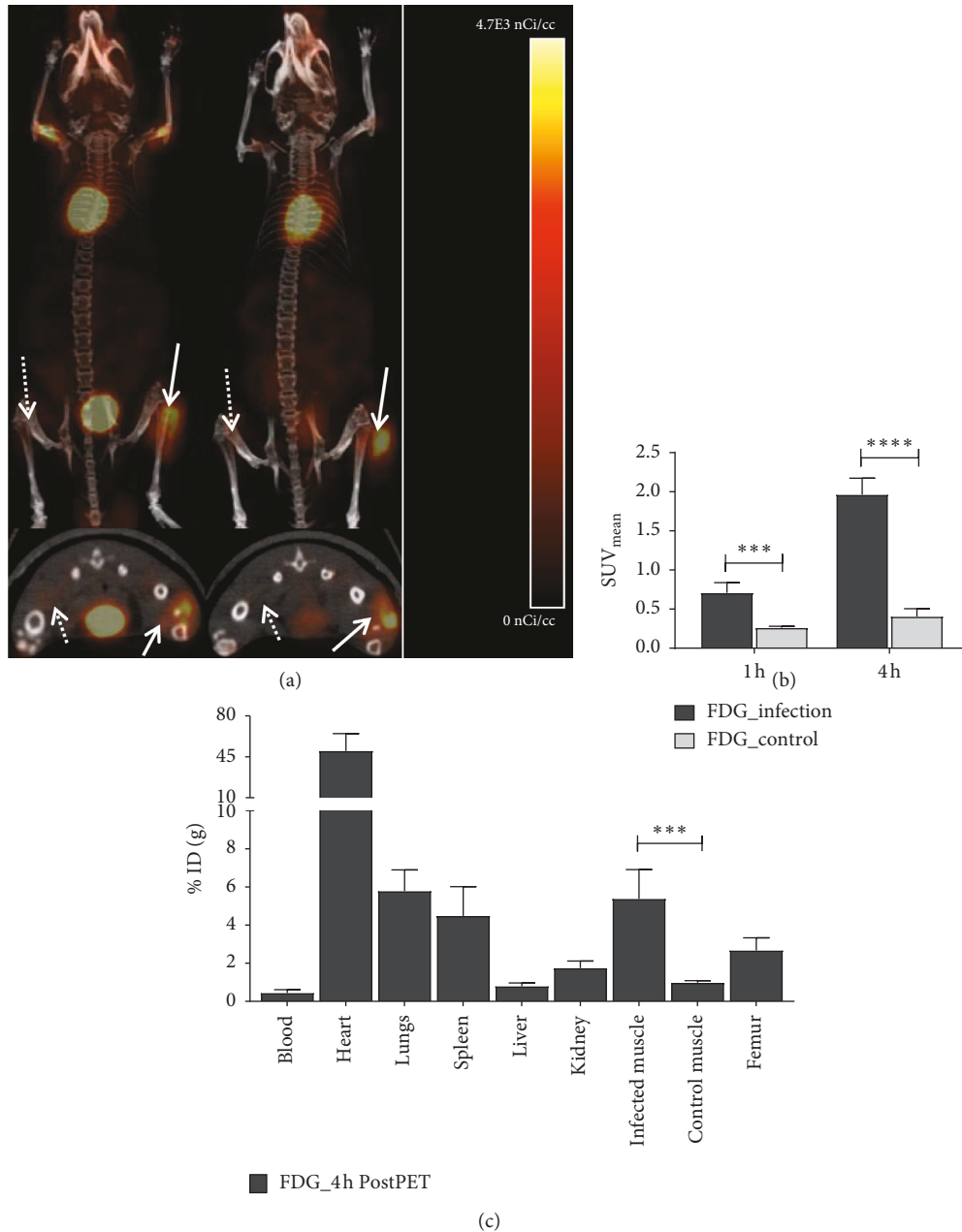


FIGURE 5: Small animal PET/CT images of (a) [ $^{18}\text{F}$ ]FDG, 4 h post injection, (b) mean SUV values calculated from infected and PBS-control muscle, and (c) post-PET biodistribution of [ $^{18}\text{F}$ ]FDG at 4 h after i.v. injection. Dashed arrow indicates the PBS-control muscle, and solid arrow indicates the infected right muscle.  $n = 6$ , \*\*\* and \*\*\*\* show significant statistical analysis at  $p < 0.0005$  and  $p < 0.0001$ , respectively.

DOTA uptake in the infected muscle is as low as the background uptake of  $^{64}\text{Cu}$ -AB1-HLys-DOTA observed in the control muscle. Mean SUV analysis of the heart supports the trend in the biodistribution study with blood retention of  $^{64}\text{Cu}$ -AB1-HLys-DOTA at  $0.65 \pm 0.08$  vs.  $0.25 \pm 0.05$  for  $^{64}\text{Cu}$ -HLys-DOTA,  $p < 0.0005$ , at 1 h. At 24 h post injection, both peptides had similar dose retention in the heart:  $0.26 \pm 0.04$  and  $0.21 \pm 0.04$  for  $^{64}\text{Cu}$ -AB1-HLys-DOTA and  $^{64}\text{Cu}$ -HLys-DOTA, respectively. The images also showed high signal in the liver and kidney possibly due to the fast clearance of the cationic peptides through these organs.

Specificity of  $^{64}\text{Cu}$ -AB1-HLys-DOTA peptide for Gram-positive bacteria was confirmed by low uptake in the Gram-negative bacteria *Pseudomonas aeruginosa* (PA) as observed in the PET images and the 4 h post-PET biodistribution, shown in Supporting Information Figure 3.  $^{64}\text{Cu}$ -AB1-HLys-DOTA uptake in the SA-infected muscle at 1 and 4 h was significantly higher than that in the PA-infected muscle:  $0.70 \pm 0.08$  vs.  $0.28 \pm 0.10$ ,  $p = 0.0052$ , and  $0.49 \pm 0.04$  vs.  $0.19 \pm 0.10$ ,  $p = 0.0288$ , respectively. A similar trend was observed in the 24 h post-PET biodistribution with percent uptake of  $^{64}\text{Cu}$ -AB1-HLys-DOTA in the SA-infected muscle

at  $2.64 \pm 0.57$  %ID/g vs.  $0.49 \pm 0.11$  %ID/g in the PA-infected muscle,  $p = 0.0039$ .

[ $^{18}\text{F}$ ]FDG uptake in the SA-infected muscle was significantly higher than that in the control muscle at 4 h post injection with mean SUV of  $1.96 \pm 0.19$  vs.  $0.41 \pm 0.09$ ,  $p < 0.0001$ , which confirmed the presence of the SA infection [34–36], as shown in Figures 5(a) and 5(b). The higher uptake of [ $^{18}\text{F}$ ]FDG in the SA-infected muscles was also confirmed with post-PET imaging biodistribution data at 4 h ( $5.4 \pm 1.3$  %ID/g vs.  $1.0 \pm 0.1$  %ID/g,  $p = 0.0009$ ), as shown in Figure 5(c).

#### 4. Discussion

Antimicrobial peptides produced by phagocytes and other cell types in the body are part of the innate immunity systems against infection resulting from pathogens. The cationic domains of these peptides interact with the negatively charged surface of the microorganisms eliciting an antimicrobial reaction when the peptide is inserted into the microbial membranes [37]. Antimicrobial peptides, due to their diversity, elicit antimicrobial activity through other mechanisms such as the Shai-Matsuzaki-Huang, albeit at micromolar concentration [38]. These peptides and other synthetic peptide can be radiolabeled with specificity for detecting localized infections using a variety of chemistries [39]. In this study, by targeting the membrane lipids enriched in bacterial cells, namely PE and Lys-PG, the iminoboronate chemistry allows selective labeling of bacterial cells over mammalian cells [26]. Radiolabeling of AB1-HLys-DOTA and HLys-DOTA peptides with  $^{64}\text{Cu}$  allowed monitoring of the infection up to 24 h and observation of their biological clearance. This was evident in the superior uptake of  $^{64}\text{Cu}$ -AB1-HLys-DOTA conjugate in *Staphylococcus aureus* bacteria in comparison to  $^{64}\text{Cu}$ -HLys-DOTA. Specific bacterial cell uptake of  $^{64}\text{Cu}$ -AB1-HLys-DOTA was also confirmed by the low uptake (less than 10%) in mammalian SKBR3 breast cancer cells, while specificity in Gram-positive bacteria was confirmed with lower uptake in *Pseudomonas aeruginosa*. Previous studies have shown specific uptake of  $^{68}\text{Ga}$ -radiolabeled probes at sites of infection [17]. Similarly, in this study, the biodistribution numbers show that  $^{64}\text{Cu}$ -AB1-HLys-DOTA has higher affinity to the infection and persists within the infection longer than  $^{64}\text{Cu}$ -HLys-DOTA that lacks the AB1 group.

The difference in accumulation of the peptides shows that the noncovalent attraction of HLys for bacterial cell surface was greatly enhanced by the covalent binding of AB1 to the lipids on the surface. In the biodistribution and PET images, clear uptake of  $^{64}\text{Cu}$ -AB1-HLys-DOTA was observed at 1 h post injection, which may be due in part to its higher bioavailability (higher %ID/g in the blood) and slower clearance.

$^{64}\text{Cu}$ -AB1-HLys-DOTA was able to distinguish between Gram-positive bacterial infection and Gram-negative bacterial infection. This class of peptides offers selective synthetic targets for bacterial lipids, which may give rise to new imaging methods of bacterial infection [26]. Although

we are yet to ascertain its utility in distinguishing infection from sterile inflammation, but as reported by Sellmyer et al., it is possible to distinguish infection from background and other noninfection inflammation sites.  $^{18}\text{F}$ -labeled small-molecule antibiotic trimethoprim [ $^{18}\text{F}$ ]FPTMP showed high uptake at the infection and low background signal in normal tissues and other noninfection inflammation sites but did not differentiate between Gram-negative and Gram-positive strains [40]. Thus, future effort in work would focus on using the peptide to distinguish sterile inflammation from bacterial infection. Additionally, optimizing the peptides with functional groups that can modulate their clearance rates and therefore increase uptake at the infection sites would be implemented in future work.

#### 5. Conclusion

The purpose of this study was to investigate the potential of AB1-HLys-DOTA peptide to image and distinguish infection due to Gram-positive bacteria from Gram-negative bacteria with higher specificity than HLys-DOTA peptide.  $^{64}\text{Cu}$ -AB1-HLys-DOTA showed higher uptake in *S. aureus* bacteria cells in vitro and improved accumulation at the infection site of SA-inoculated mice compared with the noncovalently targeting  $^{64}\text{Cu}$ -HLys-DOTA. In the small-animal PET images, the dose uptake of  $^{64}\text{Cu}$ -AB1-HLys-DOTA at the infected site was distinguishable as early as 1 h after administration, indicating its potential for fast detection of infection. These results illustrate that the  $^{64}\text{Cu}$ -labeled AB1-HLys-DOTA peptide could be used as imaging probe for detection of bacterial infection in vivo with specificity for Gram-positive bacterial infection.

#### Data Availability

The cell uptake, biodistribution, and small animal PET/CT data used to support the findings of this study are included within the article.

#### Conflicts of Interest

The authors do not have any conflicts of interest to declare.

#### Acknowledgments

Funding for the project was provided by UAB Department of Radiology and UAB Comprehensive Cancer Center's Preclinical Imaging shared facility grant (P30CA013148). Funding for Dr. Gao and coworkers was provided by the US National Institutes of Health grant (GM102735). Funding support for postdoctoral fellowship (BIDEP-2219) of Dr. F. Zumrut B. Muftuler was provided by Scientific and Technological Research Council of Turkey (TUBITAK). The authors would like to acknowledge Solana Fernandez, Sheila Bright, and Caroline Baker for animal imaging and dissection and Jennifer Bartels and Lauren Radford for  $^{64}\text{Cu}$  production.

## Supplementary Materials

Supporting Information Figure 1: (a) HPLC chromatogram of HLys-DOTA and (b) LC-MS of HLys-DOTA with  $m/z$  values at 423.7,  $m/z+ = 4$ ; 846.4,  $m/z+ = 2$ ; 1692.8,  $m/z+ = 1$ ; (c) HPLC chromatogram of AB1-HLys-DOTA and (d) LC-MS of AB1-HLys-DOTA with  $m/z$  values at 519.0,  $m/z+ = 4$ ; 691.6,  $m/z+ = 3$ ; 1037.0,  $m/z+ = 2$ . Supporting Information Table 1: radiolabeling kinetics of AB1-HLys-DOTA with  $^{64}\text{Cu}$  at different temperature and labeling ratio. Supporting Information Figure 2: HPLC chromatogram showing the radioactive peak of (a)  $^{64}\text{Cu}$ -AB1-HLys-DOTA and (b)  $^{64}\text{Cu}$ -HLys-DOTA and UV absorbance at 280 nm of (c)  $^{64}\text{Cu}$ -AB1-HLys-DOTA and (d)  $^{64}\text{Cu}$ -HLys-DOTA. Supporting Information Figure 3: small-animal PET/CT images of (a)  $^{64}\text{Cu}$ -AB1-HLys-DOTA in mice infected on the right thigh muscle with *Pseudomonas aeruginosa*, PA, (b) mean SUV values calculated from PA infected and PBS control muscle, and (c) post-PET biodistribution of  $^{64}\text{Cu}$ -AB1-HLys-DOTA at 24 h after i.v. injection. Dashed arrow indicates the PBS-control muscle, and solid arrow indicates the infected right muscle ( $n = 4$ ). (Supplementary Materials)

## References

- [1] R. P. Peters, M. A. van Agtmael, S. A. Danner, P. H. Savelkoul, and C. M. Vandembroucke-Grauls, "New developments in the diagnosis of bloodstream infections," *The Lancet Infectious Diseases*, vol. 4, no. 12, pp. 751–760, 2004.
- [2] S. Mignard and J. P. Flandrois, "16S rRNA sequencing in routine bacterial identification: a 30-month experiment," *Journal of Microbiological Methods*, vol. 67, no. 3, pp. 574–581, 2006.
- [3] L. A. Jelicks, M. P. Lisanti, F. S. Machado, L. M. Weiss, H. B. Tanowitz, and M. S. Desruisseaux, "Imaging of small-animal models of infectious diseases," *The American Journal of Pathology*, vol. 182, no. 2, pp. 296–304, 2013.
- [4] R. Kumar, S. Basu, D. Torigian, V. Anand, H. Zhuang, and A. Alavi, "Role of modern imaging techniques for diagnosis of infection in the era of 18F-fluorodeoxyglucose positron emission tomography," *Clinical Microbiology Reviews*, vol. 21, no. 1, pp. 209–224, 2008.
- [5] S. J. Goldsmith and S. Vallabhajosula, "Clinically proven radiopharmaceuticals for infection imaging: mechanisms and applications," *Seminars in Nuclear Medicine*, vol. 39, no. 1, pp. 2–10, 2009.
- [6] C. Bleeker-Rovers, F. Vos, F. Corstens, and W. Oyen, "Imaging of infectious diseases using [18F] fluorodeoxyglucose PET," *The Quarterly Journal of Nuclear Medicine and Molecular Imaging*, vol. 52, 2008.
- [7] D. K. Hughes, "Nuclear medicine and infection detection: the relative effectiveness of imaging with  $^{111}\text{In}$ -oxine-,  $^{99\text{m}}\text{Tc}$ -HMPAO-, and  $^{99\text{m}}\text{Tc}$ -stannous fluoride colloid-labeled leukocytes and with  $^{67}\text{Ga}$ -citrate," *Journal of Nuclear Medicine Technology*, vol. 31, no. 4, pp. 196–201, 2003.
- [8] J. Malamitsi, H. Giamarellou, K. Kanellakopoulou et al., "Infecton: a  $^{99\text{m}}\text{Tc}$ -ciprofloxacin radiopharmaceutical for the detection of bone infection," *Clinical Microbiology and Infection*, vol. 9, no. 2, pp. 101–109, 2003.
- [9] R. Weiner, P. B. Hoffer, and M. L. Thakur, "Lactoferrin: its role as a Ga-67-binding protein in polymorphonuclear leukocytes," *Journal of Nuclear Medicine*, vol. 22, no. 1, pp. 32–37, 1981.
- [10] C. P. Bleeker-Rovers, F. J. Vos, and F. H. M. Corstens, "Scintigraphic detection of infection and inflammation," in *Clinical Nuclear Medicine*, pp. 347–359, Springer, Berlin, Germany, 2007.
- [11] M. Charron, J. F. del Rosario, and S. Kocoshis, "Use of technetium-tagged white blood cells in patients with Crohn's disease and ulcerative colitis: is differential diagnosis possible?," *Pediatric Radiology*, vol. 28, no. 11, pp. 871–877, 1998.
- [12] C. Love and C. J. Palestro, "Radionuclide imaging of infection," *Journal of Nuclear Medicine Technology*, vol. 32, no. 2, pp. 47–57, 2004.
- [13] C. J. Palestro, "Radionuclide imaging of infection: in search of the grail," *Journal of Nuclear Medicine*, vol. 50, no. 5, pp. 671–673, 2009.
- [14] Y. Sugawara, T. D. Gutowski, S. J. Fisher, R. S. Brown, and R. L. Wahl, "Uptake of positron emission tomography tracers in experimental bacterial infections: a comparative biodistribution study of radiolabeled FDG, thymidine, l-methionine,  $^{67}\text{Ga}$ -citrate, and  $^{125}\text{I}$ -HSA," *European Journal of Nuclear Medicine and Molecular Imaging*, vol. 26, no. 4, pp. 333–341, 1999.
- [15] T. Segard, L. M. J. A. Morandau, M. L. Dunne et al., "Comparison between gallium-68 citrate PET-CT and gallium-67 citrate scintigraphy for infection imaging," *Internal Medicine Journal*, vol. 49, no. 8, pp. 1016–1022, 2019.
- [16] I. Veliky, "Prospective of  $^{68}\text{Ga}$  radionuclide contribution to the development of imaging agents for infection and inflammation," *Contrast Media & Molecular Imaging*, vol. 2018, Article ID 9713691, 24 pages, 2018.
- [17] V. Kumar, D. K. Boddeti, S. G. Evans, F. Roesch, and R. Howman-Giles, "Potential use of  $^{68}\text{Ga}$ -apo-transferrin as a PET imaging agent for detecting *Staphylococcus aureus* infection," *Nuclear Medicine and Biology*, vol. 38, no. 3, pp. 393–398, 2011.
- [18] D. Satpati, C. Arjun, R. Krishnamohan, G. Samuel, and S. Banerjee, " $^{68}\text{Ga}$ -labeled ciprofloxacin conjugates as radiotracers for targeting bacterial infection," *Chemical Biology & Drug Design*, vol. 87, no. 5, pp. 680–686, 2016.
- [19] H. Eggleston and P. Panizzi, "Molecular imaging of bacterial infections in vivo: the discrimination between infection and inflammation," *Informatics*, vol. 1, no. 1, pp. 72–99, 2014.
- [20] Z. Cai and C. J. Anderson, "Chelators for copper radionuclides in positron emission tomography radiopharmaceuticals," *Journal of Labelled Compounds and Radiopharmaceuticals*, vol. 57, no. 4, pp. 224–230, 2014.
- [21] E. W. Price and C. Orvig, "Matching chelators to radiometals for radiopharmaceuticals," *Chemical Society Reviews*, vol. 43, no. 1, pp. 260–290, 2014.
- [22] P. J. Blower, J. S. Lewis, and J. Zweit, "Copper radionuclides and radiopharmaceuticals in nuclear medicine," *Nuclear Medicine and Biology*, vol. 23, no. 8, pp. 957–980, 1996.
- [23] J. Harper, C. Skerry, S. L. Davis et al., "Mouse model of necrotic tuberculosis granulomas develops hypoxic lesions," *The Journal of Infectious Diseases*, vol. 205, no. 4, pp. 595–602, 2011.
- [24] P. Panizzi, M. Nahrendorf, J.-L. Figueiredo et al., "In vivo detection of *Staphylococcus aureus* endocarditis by targeting pathogen-specific prothrombin activation," *Nature Medicine*, vol. 17, no. 9, pp. 1142–1146, 2011.
- [25] J. Gao and H. Zheng, "Illuminating the lipidome to advance biomedical research: peptide-based probes of membrane

- lipids," *Future Medicinal Chemistry*, vol. 5, no. 8, pp. 947–959, 2013.
- [26] A. Bandyopadhyay, K. A. McCarthy, M. A. Kelly, and J. Gao, "Targeting bacteria via iminoboronate chemistry of amine-presenting lipids," *Nature Communications*, vol. 6, no. 1, p. 6561, 2015.
- [27] L. M. De León-Rodríguez and Z. Kovacs, "The synthesis and chelation chemistry of DOTA-peptide conjugates," *Bioconjugate Chemistry*, vol. 19, no. 2, pp. 391–402, 2008.
- [28] D. Wade, A. Boman, B. Wahlin et al., "All-D amino acid-containing channel-forming antibiotic peptides," *Proceedings of the National Academy of Sciences*, vol. 87, no. 12, pp. 4761–4765, 1990.
- [29] D. W. McCarthy, R. E. Shefer, R. E. Klinkowstein et al., "Efficient production of high specific activity  $^{64}\text{Cu}$  using a biomedical cyclotron," *Nuclear Medicine and Biology*, vol. 24, no. 1, pp. 35–43, 1997.
- [30] M. A. Avila-Rodriguez, J. A. Nye, and R. J. Nickles, "Simultaneous production of high specific activity  $^{64}\text{Cu}$  and  $^{61}\text{Co}$  with 11.4MeV protons on enriched  $^{64}\text{Ni}$  nuclei," *Applied Radiation and Isotopes*, vol. 65, no. 10, pp. 1115–1120, 2007.
- [31] B. V. Marquez, O. F. Ikotun, J. J. Parry, B. E. Rogers, C. F. Meares, and S. E. Lapi, "Development of a radiolabeled irreversible peptide ligand for PET imaging of vascular endothelial growth factor," *Journal of Nuclear Medicine*, vol. 55, no. 6, pp. 1029–1034, 2014.
- [32] N. Bandara, A. Zheleznyak, K. Cherukuri et al., "Evaluation of  $\text{Cu-64}$  and  $\text{Ga-68}$  radiolabeled glucagon-like peptide-1 receptor agonists as PET tracers for pancreatic  $\beta$  cell imaging," *Molecular Imaging and Biology*, vol. 18, no. 1, pp. 90–98, 2016.
- [33] O. Jacobson, I. D. Weiss, L. P. Szajek et al., "PET imaging of CXCR4 using copper-64 labeled peptide antagonist," *Theranostics*, vol. 1, pp. 251–262, 2011.
- [34] C. Love, M. B. Tomas, G. G. Tronco, and C. J. Palestro, "FDG PET of infection and inflammation," *Radiographics*, vol. 25, no. 5, pp. 1357–1368, 2005.
- [35] M. J. Kim, C.-H. Lee, Y. Lee et al., "Glucose-6-phosphatase expression-mediated  $^{18}\text{F}$  FDG efflux in murine inflammation and cancer models," *Molecular Imaging and Biology*, vol. 21, no. 5, pp. 917–925, 2019.
- [36] D. Pellegrino, A. A. Bonab, S. C. Dragotakes, J. T. Pitman, G. Mariani, and E. A. Carter, "Inflammation and infection: imaging properties of  $^{18}\text{F}$ -FDG-labeled white blood cells versus  $^{18}\text{F}$ -FDG," *Journal of Nuclear Medicine*, vol. 46, no. 9, pp. 1522–1530, 2005.
- [37] R. M. Eband and H. J. Vogel, "Diversity of antimicrobial peptides and their mechanisms of action," *Biochimica et Biophysica Acta (BBA)-Biomembranes*, vol. 1462, no. 1–2, pp. 11–28, 1999.
- [38] M. Zasloff, "Antimicrobial peptides of multicellular organisms," *Nature*, vol. 415, no. 6870, pp. 389–395, 2002.
- [39] M. M. Welling, P. H. Nibbering, A. Paulusma-Annema, P. S. Hiemstra, E. K. Pauwels, and W. Calame, "Imaging of bacterial infections with  $^{99\text{m}}\text{Tc}$ -labeled human neutrophil peptide-1," *Journal of Nuclear Medicine*, vol. 40, no. 12, pp. 2073–2080, 1999.
- [40] M. A. Sellmyer, I. Lee, C. Hou et al., "Bacterial infection imaging with  $^{18}\text{F}$ fluoropropyl-trimethoprim," *Proceedings of the National Academy of Sciences*, vol. 114, no. 31, pp. 8372–8377, 2017.

## Clinical Study

# The Clinical Impact of Using $^{18}\text{F}$ -FDG-PET/CT in the Diagnosis of Suspected Vasculitis: The Effect of Dose and Timing of Glucocorticoid Treatment

Kirsi Taimen <sup>1,2</sup>, Soile P. Salomäki,<sup>2,3</sup> Ulla Hohenthal,<sup>2,3</sup> Markku Mali,<sup>1,2</sup> Sami Kajander,<sup>4,5</sup> Marko Seppänen,<sup>4,6</sup> Pirjo Nuutila,<sup>2,4</sup> Antti Palomäki,<sup>1,2</sup> Anne Roivainen <sup>4</sup>, Laura Pirilä,<sup>1,2</sup> and Jukka Kemppainen<sup>2,4,6</sup>

<sup>1</sup>Center for Rheumatology and Clinical Immunology, Division of Medicine, Turku University Hospital, Turku, Finland

<sup>2</sup>Department of Medicine, University of Turku, Turku, Finland

<sup>3</sup>Department of Infectious Diseases, Division of Medicine, Turku University Hospital, Turku, Finland

<sup>4</sup>Turku PET Center, Turku University Hospital and University of Turku, Turku, Finland

<sup>5</sup>Department of Radiology, Turku University Hospital, Turku, Finland

<sup>6</sup>Department of Clinical Physiology and Nuclear Medicine, Turku University Hospital, Turku, Finland

Correspondence should be addressed to Kirsi Taimen; [kirsi.taimen@tyks.fi](mailto:kirsi.taimen@tyks.fi)

Received 22 May 2019; Accepted 7 August 2019; Published 29 August 2019

Academic Editor: Guillermina Ferro-Flores

Copyright © 2019 Kirsi Taimen et al. This is an open access article distributed under the Creative Commons Attribution License, which permits unrestricted use, distribution, and reproduction in any medium, provided the original work is properly cited.

$^{18}\text{F}$ -Fluorodeoxyglucose positron-emission tomography ( $^{18}\text{F}$ -FDG-PET) with computed tomography (CT) is effective for diagnosing large vessel vasculitis, but its usefulness in accurately diagnosing suspected, unselected vasculitis remains unknown. We evaluated the feasibility of  $^{18}\text{F}$ -FDG-PET/CT in real-life cohort of patients with suspicion of vasculitis. The effect of the dose and the timing of glucocorticoid (GC) medication on imaging findings were in special interest. 82 patients with suspected vasculitis were evaluated by whole-body  $^{18}\text{F}$ -FDG-PET/CT. GC treatment as prednisolone equivalent doses at the scanning moment and before imaging was evaluated. 38/82 patients were diagnosed with vasculitis. Twenty-one out of 38 patients had increased  $^{18}\text{F}$ -FDG accumulation in blood vessel walls indicating vasculitis in various sized vessels. Vasculitis patients with a positive vasculitis finding in  $^{18}\text{F}$ -FDG-PET/CT had a significantly shorter duration of GC use (median = 4.0 vs 7.0 days,  $P = 0.034$ ), and they used lower GC dose during the PET scan (median dose = 15.0 mg/day vs 40.0 mg/day,  $p = 0.004$ ) compared to  $^{18}\text{F}$ -FDG-PET/CT-negative patients. Vasculitis patients with a positive  $^{18}\text{F}$ -FDG-PET/CT result had significantly higher C-reactive protein (CRP) than patients with a negative  $^{18}\text{F}$ -FDG-PET/CT finding (mean value = 154.5 vs 90.4 mg/L,  $p = 0.018$ ). We found that  $^{18}\text{F}$ -FDG-PET/CT positivity was significantly associated with a lower dose and shorter duration of GC medication and higher CRP level in vasculitis patients.  $^{18}\text{F}$ -FDG-PET/CT revealed clinically significant information in over half of the patients and was effective in confirming the final diagnosis.

## 1. Introduction

The diagnosis of vasculitis is a challenge, especially when vasculitis affects vital organs, and the patient presents nonspecific symptoms [1]. Vasculitis requires prompt recognition and initiation of treatment even if the diagnosis is uncertain.

The diagnostic process is often laborious. A biopsy is considered as a gold standard for diagnosing vasculitis, but in many cases, the optimal biopsy location is unavailable. The combination of  $^{18}\text{F}$ -fluorodeoxyglucose-positron emission tomography ( $^{18}\text{F}$ -FDG-PET) with computed tomography (CT) is a promising diagnostic tool in the workup for vasculitis [2–4].

The accuracy and usefulness of  $^{18}\text{F}$ -FDG-PET/CT in the diagnostic procedure of vasculitis are still under debate.  $^{18}\text{F}$ -FDG-PET/CT has showed good performance in detecting large-vessel vasculitis (LVV) [4–7]. European League Against Rheumatism (EULAR) recommendation for the use of imaging in LVV in clinical practice recommends an early imaging test with ultrasound or MRI as first choices. PET may be used alternatively especially considering its ability to identify other serious differential diagnostic conditions [8]. In 2018, nuclear medicine interest committees gave a joint procedural recommendation on  $^{18}\text{F}$ -FDG-PET/CTA (angiography) imaging advising in data acquisition and interpretation in LVV and polymyalgia rheumatica [9]. Less is known about how  $^{18}\text{F}$ -FDG-PET/CT performs in other types of vasculitis than LVV. There is some evidence that PET may be useful in detecting small-vessel vasculitis [10, 11]. The ongoing multinational Diagnostic and Classification Criteria for Vasculitis (DCVAS) study aims to validate diagnostic criteria and to improve classification criteria for primary systemic vasculitis [12].

With a strong suspicion of vasculitis, rapid initiation of treatment is necessary. Glucocorticoids (GCs) are the most important first-line immunosuppressive treatment of non-infectious vasculitides [13, 14]. Unfortunately, the use of immunosuppressive medication probably deteriorates the diagnostic accuracy of  $^{18}\text{F}$ -FDG-PET [7]. GC may attenuate  $^{18}\text{F}$ -FDG-uptake as early as after three days, but more confirmation is needed, since this is clinically a crucial question [15–18].

Here, we evaluated the impact of using  $^{18}\text{F}$ -FDG-PET/CT for accurately diagnosing vasculitis in real-life cohort of patients. We had a special interest in observing the effect of GC treatment prior to the  $^{18}\text{F}$ -FDG-PET/CT scan. We evaluated also differential diagnostic findings in patients with vasculitis suspicion.

## 2. Materials and Methods

**2.1. Patients and Study Design.** Eighty-two patients with suspected vasculitis were evaluated by whole-body  $^{18}\text{F}$ -FDG-PET/CT. The enrolment was done prospectively among inpatients. All diagnostic procedures were done at Turku University Hospital, Turku, Finland, between May 2011 and June 2015. The hospital is a tertiary-care centre for a population of 470 000. The institutional ethical committee approved the study protocol. All patients gave a written informed consent, according to the Declaration of Helsinki. This study is part of the Positron Emission Tomography of Infection and Vasculitis (PETU) study, which is registered as a clinical trial (NCT01878721). The PETU study researched different branches of infectious and inflammatory diseases which are reported separately [19–22]. Our series of vasculitis patients are previously unpublished.

The inclusion criterion of this study was vasculitis suspicion. Vasculitis suspicion was raised by an experienced specialist based on the clinical symptoms and signs of the patient. Vasculitis was confirmed or excluded by a consensus-based decision made by the specialists, while taking notice of the medical history, results of clinical examination,

extensive laboratory work,  $^{18}\text{F}$ -FDG-PET/CT result, other imaging modalities, response to GC therapy, and follow-up. A minimum of 6 months clinical follow-up was considered sufficient to establish the diagnosis.

Special attention was paid to examine features and GC use in patients with diagnosed vasculitis in relation to  $^{18}\text{F}$ -FDG-PET/CT results. The cumulative GC dose was calculated from patients with a history of continuous GC use. GC use was evaluated as prednisolone equivalent doses.

**2.2. Evaluation of the Diagnoses.** The final diagnosis was based on the clinical picture as well as on the imaging findings of different sizes of affected vessels and histology. Based on the diagnosis, we divided the vasculitis patients into the following groups: LVV, medium- and small-vessel vasculitis, and unspecified vasculitis or antineutrophilic cytoplasmic antibodies- (ANCA-) associated vasculitis (AAV). Due to a low number of patients, vasculitis patients with granulomatous polyangiitis (GPA), eosinophilic granulomatous polyangiitis (EGPA), and microscopic polyangiitis (MPA) were combined into a group called AAV. In this group, five out of six patients were ANCA-positive, and an ANCA-negative patient had a histological finding of vasculitis.

All patients were evaluated by using the clinical criteria for vasculitis by American College of Rheumatology (ACR) 1990 [23, 24]. We evaluated the ACR criteria for GCA, GPA, EGPA, MPA, and polyarteritis nodosa (PAN). Due to a limited number of patients, cases from GPA, EGPA, and MPA formed a single group.

**2.3.  $^{18}\text{F}$ -FDG-PET/CT Imaging Protocol.** A whole-body  $^{18}\text{F}$ -FDG-PET/CT scan (64-slice Discovery VCT, General Electric Medical Systems, Milwaukee, WI, USA) was performed in all patients. Patients fasted at least 10 hours before the study. The mean injected radioactive dose of  $^{18}\text{F}$ -FDG was 273 MBq (range = 197–390 MBq). After an average of 57 minutes (range = 44–79 minutes), a whole-body PET acquisition (3 min/bed position) was performed following low-dose CT (kV 120, Smart mA range 10–80). In some patients, this was followed by a diagnostic contrast-enhanced CT scan (kV 120, Smart mA range 100–440) during the arterial phase after an automated i.v. injection of contrast agent.

Blood glucose levels were  $<10\text{ mmol}\cdot\text{L}^{-1}$  prior to injection of the tracer in all patients. PET images were reconstructed in  $128 \times 128$  matrix size in full 3D mode using maximum-likelihood reconstruction with an ordered-subset expectation maximization algorithm (VUE Point, GE Healthcare).

Visual analysis of the images was performed by an experienced nuclear medicine specialist, and the results were re-evaluated by the research team for a consensus-based diagnosis. All image analyses were done blinded with respect to patient's clinical details.  $^{18}\text{F}$ -FDG-PET/CT scans were considered positive, when a linear uptake pattern was found in the large arterial walls and/or its branches with an intensity similar or higher than the liver [25]. A positive finding for small- to medium-sized vasculitis was considered, when

activity was higher than the vascular background activity and showed a tree-root-like uptake pattern [21] (Figure 1).

**2.4. Statistical Analysis.** Normally distributed continuous data were expressed as mean (standard deviation, SD), and for skewed distributions, data were expressed as median (interquartile range, IQR), unless stated otherwise. Categorical variables were described with absolute and relative (percentage) frequencies. An independent sample *t* test or Mann–Whitney *U* test was applied to determine the significance of differences for continuous variables as appropriate and a chi-squared or Fischer’s exact test for categorical variables. All statistical analyses were calculated using SPSS Software Package (IBM SPSS Statistics Version 24). *P* values  $\leq 0.05$  were considered significant.

### 3. Results

**3.1. Patients’ Characteristics, Diagnosis, and  $^{18}\text{F}$ -FDG-PET/CT Findings.** A total of 82 patients with a clinical suspicion of vasculitis were referred for  $^{18}\text{F}$ -FDG-PET/CT and prospectively screened for this study (38 males and 44 females) (Figure 2). The mean age for patients was 62.7 years (age range = 19–89 years, SD = 16.0 years). An abnormal or clinically significant  $^{18}\text{F}$ -FDG-PET/CT finding was encountered in 46/82 patients (56%) (Table 1). A clinically significant  $^{18}\text{F}$ -FDG-PET/CT finding in different diagnostic subgroups is depicted in Table 1.

The vasculitis diagnosis was confirmed in 38 (46%) of the patients (Table 2). Most common cases of vasculitis were LVV ( $n = 14$ , 37%) and unspecified vasculitis ( $n = 10$ , 26%). Increased  $^{18}\text{F}$ -FDG accumulation in blood vessels suitable for vasculitis was detected in 21 of these 38 (55%) patients (Tables 2 and 3).  $^{18}\text{F}$ -FDG-PET/CT-positive patients fulfilled the ACR criteria for GCA significantly more often than  $^{18}\text{F}$ -FDG-PET/CT-negative patients (38% vs 8%,  $p = 0.015$ ). No accumulation of  $^{18}\text{F}$ -FDG in blood vessels was detected in 44 patients who did not fulfil the vasculitis diagnosis. Among patients without vasculitis diagnosis, the most common diagnostic groups were autoimmune diseases other than vasculitis (not including polymyalgia rheumatica, PM) ( $n = 18$ , 41%), infection ( $n = 12$ , 27%), PM ( $n = 5$ , 11%), and malignancy ( $n = 4$ , 9%) (Figure 2). In the PM group, one patient had  $^{18}\text{F}$ -FDG accumulation in the shoulder area relating to PM. One patient had a biopsy proven panniculitis which was clinically significant but not related to PM. Rest of the three patients did not have significant  $^{18}\text{F}$ -FDG-PET/CT findings.

**3.2. Effect of Glucocorticoid Treatment on  $^{18}\text{F}$ -FDG-PET/CT Findings among the Vasculitis Patients.** The duration and dose of GC treatment had a significant effect on the outcomes of the  $^{18}\text{F}$ -FDG-PET/CT scans. Out of 38 vasculitis patients, 9 patients (24%) had no GC treatment previously and 8 (21%) had used GC over 31 days.

Vasculitis patients with positive  $^{18}\text{F}$ -FDG-PET/CT had significantly fewer days of GC use before imaging than patients with negative  $^{18}\text{F}$ -FDG-PET/CT (median = 4.0 (IQR 9)



FIGURE 1: PET scan showing  $^{18}\text{F}$ -FDG-uptake in large- and medium- sized vessels. Maximum intensity projection (MIP) image of a whole-body PET-image of a 67-year-old male with high fever, mild headache, and a CRP value of 300 mg/l. After an extensive clinical workup, suspicion of vasculitis occurred, when there was no response to antibiotics. Whole-body CT showed no infection or malignant focus. Temporal arterial biopsy was equivocal. A PET/CT scan confirmed the vasculitis diagnosis by showing a tree-root-like  $^{18}\text{F}$ -FDG uptake pattern in large- and medium-sized arteries in the lower limbs. Physiological tracer uptake is noted in the brain, the neck muscles, the myocardium, the kidneys, and the bladder.

vs 7.0 (IQR 154) days,  $p = 0.034$ ) (Table 3). In patients scanned within 3 days of GC treatment, 77% had vascular  $^{18}\text{F}$ -FDG uptake suitable for vasculitis in comparison to 42% after one week of treatment (Figure 3). Among these 38 vasculitis patients, there was a significant association of  $^{18}\text{F}$ -FDG-PET/CT positivity with a lower GC dose on the scanning day with a median dose 15.0 (IQR 40.0) mg/day vs 40.0 (IQR 30.0) mg/day ( $p = 0.004$ ) (Table 3).

Patients with vasculitis used a higher GC dose during  $^{18}\text{F}$ -FDG-PET/CT scan than patients without vasculitis having a median prednisolone use of 30.0 (IQR 33.0) mg/day vs 0 (IQR 20.0) mg/day ( $p = 0.001$ ). Among vasculitis patients, 9 patients (24%) used no GC on the scanning day in comparison to the nonvasculitis group, where 24 patients (55%) used no GC on the scanning day.

**3.3. Laboratory and Clinical Findings of the Patients.** Among all 82 patients with suspicion of vasculitis, C-reactive protein (CRP) was elevated in 75 patients (91.5%), with a mean CRP value of 129.0 mg/L (SD = 89.5 mg/L). Vasculitis patients with a positive  $^{18}\text{F}$ -FDG-PET/CT scan had significantly higher CRP values than vasculitis patients with a negative  $^{18}\text{F}$ -FDG-PET/CT scan (mean CRP = 154.5 mg/L;

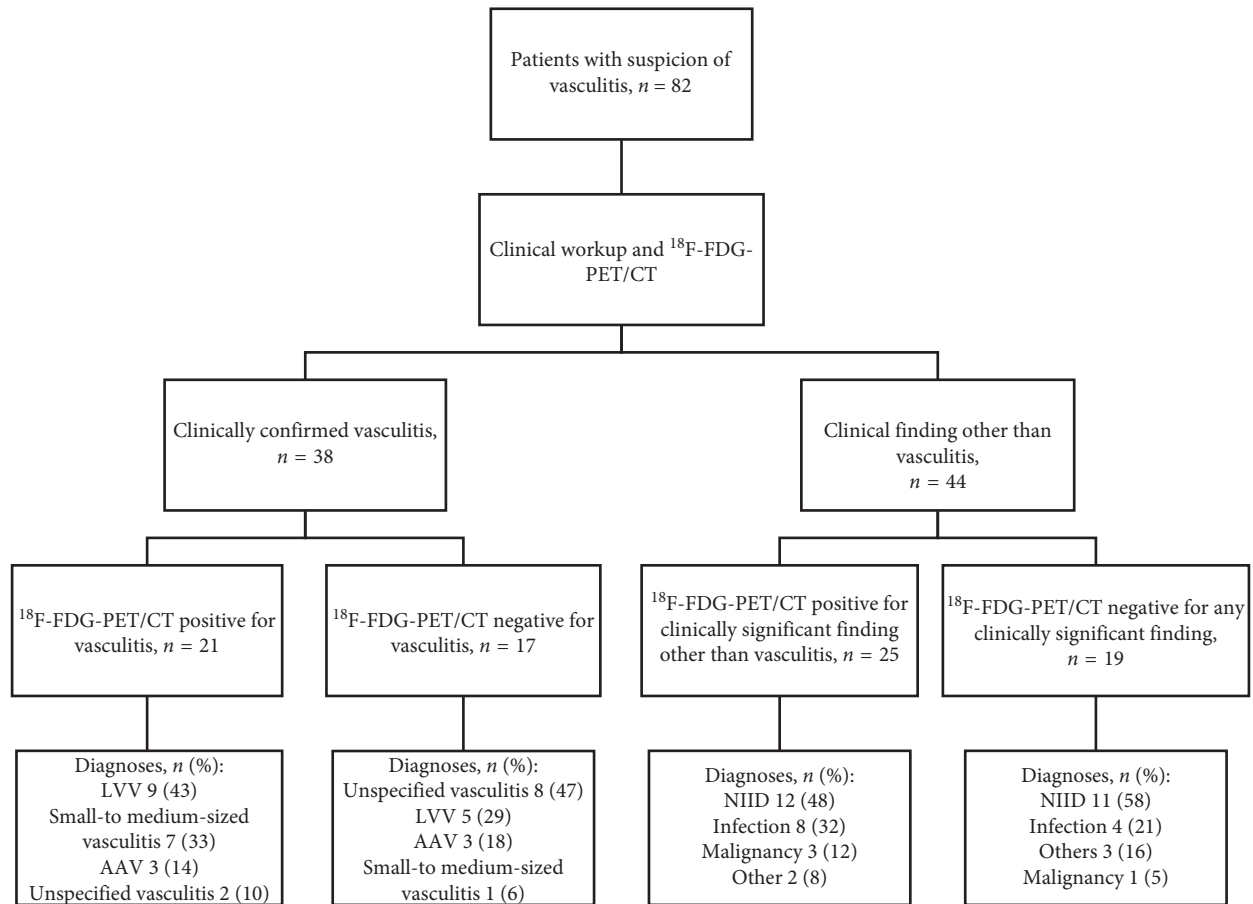


FIGURE 2: Diagram of the study design. 82 patients with a clinical suspicion of vasculitis referred for  $^{18}\text{F}$ -FDG-PET/CT were included. Diagnoses were confirmed by consensus-based decisions made by specialists after evaluation of a standard extensive workup,  $^{18}\text{F}$ -FDG-PET/CT scan, and a minimum of 6 months follow-up. Vasculitis patients with a negative  $^{18}\text{F}$ -FDG-PET/CT for vasculitis had other minor findings in PET/CT: mild infection ( $n = 2$ , 12%), pericarditis ( $n = 1$ , 6%), and pleuritis ( $n = 1$ , 6%). Among nonvasculitis patients, clinically significant  $^{18}\text{F}$ -FDG-PET/CT findings were as follows: NIID ( $n = 12$ ), infection ( $n = 8$ ), malignancy ( $n = 3$ ), and miscellaneous ( $n = 2$ ). LVV = large-vessel vasculitis. AAV = antineutrophil cytoplasmic antibody- (ANCA-) associated vasculitis. NIID = noninfectious inflammatory disease other than vasculitis.

SD 100.2 mg/L vs 90.4 mg/L; SD 55.6 mg/L, respectively;  $p = 0.018$ ) (Table 3). No difference was found in procalcitonin (PCT) values (data available from 62 patients) between vasculitis patients with positive or negative  $^{18}\text{F}$ -FDG-PET/CT findings (Table 3). There was no difference in CRP or PCT values between vasculitis and nonvasculitis patients (Table 2).

Forty-eight (out of 79) patients (60.8%) had a fever over  $38^\circ\text{C}$ . Other common clinical symptoms were haematuria ( $n = 38/75$ , 46.3%), myalgia ( $n = 36/79$ , 43.9%), hip pain ( $n = 24/76$ , 29.3%), bilateral shoulder pain ( $n = 18/78$ , 22%), a new headache ( $n = 14/78$ , 17.1%), and new neuropathy ( $n = 11/79$ , 13.3%). When comparing vasculitis with nonvasculitis patients, vasculitis patients had significantly more often a new headache (29% vs 7%,  $p = 0.008$ ).

#### 4. Discussion

The spectrum of conditions causing vasculitis-like symptoms is wide. We found that in real-life cohort of patients,  $^{18}\text{F}$ -FDG-PET/CT was effective in confirming the

final diagnosis among inpatients with vasculitis suspicion.  $^{18}\text{F}$ -FDG-PET/CT showed vasculitis in 26% of all patients and revealed clinically significant information in over half of the patients.

We found that among vasculitis patients, a shorter duration of prednisolone use is significantly associated with positive  $^{18}\text{F}$ -FDG-PET/CT vasculitis findings (Table 3). Vasculitis patients with positive  $^{18}\text{F}$ -FDG-PET/CT imaging had a median of 4 days of prednisolone treatment versus 7 days in the negative  $^{18}\text{F}$ -FDG-PET/CT group. This implicates that withholding diagnostic imaging for over one week during GC treatment increases the risk of a false-negative diagnosis. In the vasculitis group, a lower GC dose at the scanning moment was significantly associated with an  $^{18}\text{F}$ -FDG-PET/CT-based vasculitis diagnosis (Table 3).

In a previous study, good sensitivity, at 80%, and specificity, at 79%, have been reported for  $^{18}\text{F}$ -FDG-PET/CT in patients with GCA receiving GC less than 3 days [6]. In another study, Fuchs et al. reported that the sensitivity of  $^{18}\text{F}$ -FDG-PET/CT lowers from 99% to 53% in patients with GCA receiving an immunosuppressant [7]. A reduction of

TABLE 1: Final clinical diagnosis and significance of PET/CT by each diagnosis.

Category	Number of cases	Clinically significant PET/CT finding
Other autoimmune diseases	18	10/18
Adult-onset Still's disease	3	0/3
Sarcoidosis	2	1/2
Collagenosis	2	2/2
Pericarditis	2	1/2
Morbus Crohn/IBD	2	1/2
Myositis	2	2/2
SLE	2	1/2
Unspecified	2	1/2
Rheumatoid arthritis	1	1/1
Large vessel vasculitis	14	9/14
Giant cell arteritis	13	9
Takayasu arteritis	1	0
Infection	12	8/12
Infection NAS/FUO	3	2/3
Deep abscess	3	2/3
Septic arthritis	1	1/1
Septic spondylodiscitis	1	1/1
Pneumonia	1	1/1
Urinary tract infection	1	0/1
Cholecystitis	1	1/1
Tuberculosis	1	0/1
Unspecified vasculitis*	10	2/10
Vasculitis NAS	8	2
Secondary vasculitis	2	0
Small- and medium-sized vasculitis (other than ANCA-associated vasculitis)	8	7/8
ANCA-associated vasculitis**	6	3/6
EGPA	3	1/3
GPA	2	2/2
MPA	1	0/1
Polymyalgia rheumatica	5	2/5
Malignancy	4	3/4
Lymphoma	3	2/3
Lung cancer	1	1/1
Miscellaneous	4	1/4
Cardiac disease	2	0/2
Calciphylaxis	1	0/1
Leg ulcers	1	1/1
Unknown diagnosis	1	1/1

ANCA, antineutrophil cytoplasmic antibody; EGPA, eosinophilic granulomatosis with polyangiitis; GPA, granulomatosis with polyangiitis; MPA, microscopic polyangiitis; FUO, fever of unknown origin. \* Vasculitis diagnosis confirmed by either imaging or biopsy. \*\* 5/6 patients were ANCA-positive. The ANCA-negative patient had biopsy confirmed diagnosis.

$^{18}\text{F}$ -FDG accumulation under treatment has been reported in follow-up studies [16, 26]. A study by Imfeld et al. shows that prednisone treatment  $\geq 10$  days significantly reduced  $^{18}\text{F}$ -FDG-PET/CT sensitivity. The first effect of lowered sensitivity was seen as early as 3 days after treatment initiation in the abdominal aorta [17] and in supra-aortic vessels [15]. Surprisingly, a study by Clifford et al. [18] did not find a correlation. Clifford et al. explained that their study subject number was low ( $n=28$ ), patients had received treatment over long time (on an average of 11.9 days), and doses were similarly high among all patients.

In a real clinical setting, withholding the treatment initiation until imaging is often impossible, so the knowledge of the GC effect on  $^{18}\text{F}$ -FDG-PET diagnostic

performance is important. Our study supports the data that GC treatment reduces the diagnostic power of  $^{18}\text{F}$ -FDG-PET/CT after one week. Thus, there is a need for fast  $^{18}\text{F}$ -FDG-PET/CT availability for suspected vasculitis patients. These patients represent often a diffuse clinical picture. Ultrasound, which nowadays is the recommended standard protocol in LVV, performs poorly in thoracic aorta area or in small, deep vessels without focal symptoms. In our material,  $^{18}\text{F}$ -FDG-PET/CT was useful also in other vasculitis than LVV and performs well in thoracic vessels. A lower GC dose during PET/CT scanning was associated with vasculitis findings in  $^{18}\text{F}$ -FDG-PET/CT, but our study cannot answer the question that, if lowering temporarily the GC dose helps avoid false-negative results. In few patients,  $^{18}\text{F}$ -FDG-PET/CT showed

TABLE 2: Patients' characteristics based on vasculitis diagnosis.

	Vasculitis ( <i>n</i> = 38)	No vasculitis ( <i>n</i> = 44)	<i>P</i> value
Female sex, <i>n</i> (%)	23 (60.5)	21 (47.7)	0.246
Age, years, mean (SD)	66.3 (13.4)	59.5 (17.5)	0.056
CRP max, mg/l, mean (SD)	125.8 (88.3)	131.8 (91.4)	0.765
PCT max, µg/l, mean (SD)	0.16 (0.16), <i>n</i> = 29	0.16 (0.18), <i>n</i> = 33	0.872
Prednisolone at scanning moment, mg, median (IQR)	30.0 [33]	1.0 [20]	0.001*
Patients using prednisolone	29/38	20/44	
Prednisolone prior scanning, <i>d</i> , median (IQR)	6.0 [11]	0.0 [52]	0.135
Prednisolone cumulative dose, mg, median (IQR)	260.0 [1500]	1.00 [1706]	0.075
Fulfills ACR criteria for GCA, <i>n</i> (%)	10 (26.3)	3 (6.8)	0.016*
Fulfills ACR criteria for EGPA, GPA, or MPA, <i>n</i> (%)	12 (31.6)	8 (18.2)	0.159
Fulfills ACR criteria for PAN, <i>n</i> (%)	5 (13.2)	2 (4.5)	0.164
Fever over 38°C, <i>n</i> = 79, <i>n</i> (%)	22 (57.9)	26 (63.4)	0.616

SD, standard deviation; CRP, C-reactive protein; PCT, procalcitonin; IQR, interquartile range; ACR, American College of Rheumatology; GCA, giant cell arteritis; EGPA, eosinophilic granulomatous polyangiitis; GPA, granulomatous polyangiitis; MPA, microscopic polyangiitis; PAN, polyarteritis nodosa. \*Significant at *P* value <0.05.

TABLE 3: Characteristics of vasculitis patients.

	<sup>18</sup> F-FDG-PET/CT positive ( <i>n</i> = 21)	<sup>18</sup> F-FDG-PET/CT negative ( <i>n</i> = 17)	<i>P</i> value
Female sex, <i>n</i> (%)	14 (66.7)	9 (52.9)	0.389
Age, years, mean (SD)	68.0 (12.1)	64.2 (15.0)	0.390
CRP max, mg/l, mean (SD)	154.5 (100.2)	90.4 (55.6)	0.018*
PCT max, µg/l, mean (SD)	0.12 (0.09), <i>n</i> = 17	0.22 (0.02), <i>n</i> = 12	0.137
ANCA positive, <i>n</i> (%)	3 (14.3)	4 (23.5)	0.478
Prednisolone at scanning moment, mg, median [IQR]	15.0 [40.0]	40.0 [30.0]	0.004*
Prednisolone prior scanning, <i>d</i> , median [IQR]	4.0 [9]	7.0 [154]	0.034*
Prednisolone cumulative dose, mg, median [IQR]	120 [1120]	360 [1965]	0.096
Fever over 38°C	14 (66.7)	8 (47.1)	0.224

SD, standard deviation; CRP, C-reactive protein; PCT, procalcitonin; IQR, interquartile range; ANCA, antineutrophil cytoplasmic antibody. \*Significant at *P* value <0.05.

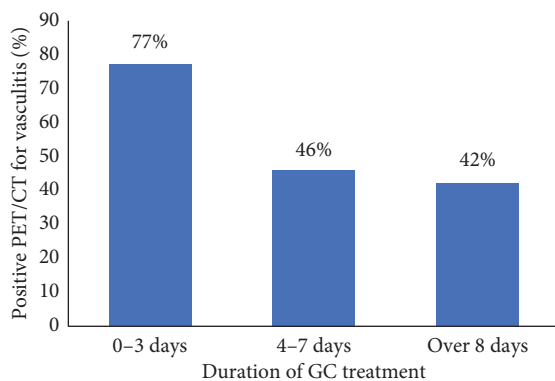


FIGURE 3: Positive <sup>18</sup>F-FDG-PET/CT scans (%) for vasculitis and the duration of glucocorticoid (GC) treatment (days). In our study population, 21 of 38 vasculitis patients had positive <sup>18</sup>F-FDG-PET/CT finding. In patients scanned within 3 days of GC treatment, 77% had vascular <sup>18</sup>F-FDG uptake suitable for vasculitis in comparison to 42% after 8 days of treatment.

vascular uptake suitable for vasculitis even after long GC treatment. In our cohort, the duration of use and dosage of GC treatment varied in patients at the <sup>18</sup>F-FDG-PET/CT imaging due to the study design.

We found a significant correlation between higher CRP value and <sup>18</sup>F-FDG-PET/CT positivity in patients diagnosed with vasculitis. A high CRP value might reflect more active inflammation and less use of GC at the scanning moment. There are several studies testing the correlation of laboratory parameters and diagnostic performance of <sup>18</sup>F-FDG-PET/CT in GCA, in fever of unknown origin (FUO), or in inflammation of unknown origin (IUO) [17, 27–29]. FUO and IUO are essential differential diagnostic challenges for vasculitis. Schönau et al. reported that an age over 50 years, a CRP level over 30 mg/L, and the absence of fever predicted the helpfulness of <sup>18</sup>F-FDG-PET/CT [27] in FUO and IUO. Papatheanasiou et al. noticed a significant positive association between maximal aortic <sup>18</sup>F-FDG uptake and inflammatory markers [29].

Our study had limitations that should be considered. The study was done in a real clinical setting, and the inclusion criterion was vasculitis suspicion; therefore, the vasculitis patient group was heterogeneous. The vasculitis diagnosis was confirmed later, and the spectrum of different vasculitis was detected. Our study did not exclude patients who did not fulfil the ACR inclusion criteria. This might be a limitation when comparing the results to previous studies with more restricted inclusion criteria.

## 5. Conclusions

We found that in patients with confirmed vasculitis diagnosis,  $^{18}\text{F}$ -FDG-PET/CT positivity was significantly related to a lower dose and shorter duration of GC medication and a higher CRP level. In real-life circumstances,  $^{18}\text{F}$ -FDG-PET/CT revealed different types of vasculitides as well as other clinically significant information in over half of the patients and had an impact in confirming the final diagnosis.

## Data Availability

The data included in this study are available upon request from the corresponding author.

## Conflicts of Interest

The authors declare that they have no conflicts of interest.

## Acknowledgments

The authors wish to thank Mia Koutu and Laura Kontto for helping with  $^{18}\text{F}$ -FDG-PET/CT imaging and the staff of Department of Rheumatology for recruiting study subjects. Robert M. Badeau, M.Sc., Ph.D., of Aura Professional English Language Consulting, Ltd. (<http://auraenglish.com>) performed this manuscript's English language checking and proofreading service. This study was supported by the State Research Funds of Turku University Hospital and the Finnish Society for Rheumatology.

## References

- [1] C. M. Weyand and J. J. Goronzy, "Giant-cell arteritis and polymyalgia rheumatica," *New England Journal of Medicine*, vol. 371, no. 17, pp. 1652–1653, 2014.
- [2] S. Prieto-González, P. Arguis, and M. C. Cid, "Imaging in systemic vasculitis," *Current Opinion in Rheumatology*, vol. 27, no. 1, pp. 53–62, 2015.
- [3] C. Puppo, M. Massollo, F. Paparo et al., "Giant cell arteritis: a systematic review of the qualitative and semiquantitative methods to assess vasculitis with  $^{18}\text{F}$ -fluorodeoxyglucose positron emission tomography," *BioMed Research International*, vol. 2014, Article ID 574248, 11 pages, 2014.
- [4] F. L. Besson, J.-J. Parienti, B. Bienvenu et al., "Diagnostic performance of  $^{18}\text{F}$ -fluorodeoxyglucose positron emission tomography in giant cell arteritis: a systematic review and meta-analysis," *European Journal of Nuclear Medicine and Molecular Imaging*, vol. 38, no. 9, pp. 1764–1772, 2011.
- [5] M. Soussan, P. Nicolas, C. Schramm et al., "Management of large-vessel vasculitis with FDG-PET," *Medicine*, vol. 94, no. 14, p. e622, 2015.
- [6] S. Prieto-González, M. Depetris, A. García-Martínez et al., "Positron emission tomography assessment of large vessel inflammation in patients with newly diagnosed, biopsy-proven giant cell arteritis: a prospective, case-control study," *Annals of the Rheumatic Diseases*, vol. 73, no. 7, pp. 1388–1392, 2014.
- [7] M. Fuchs, M. Briel, T. Daikeler et al., "The impact of  $^{18}\text{F}$ -FDG PET on the management of patients with suspected large vessel vasculitis," *European Journal of Nuclear Medicine and Molecular Imaging*, vol. 39, no. 2, pp. 344–353, 2012.
- [8] C. Dejaco, S. Ramiro, C. Duftner et al., "EULAR recommendations for the use of imaging in large vessel vasculitis in clinical practice," *Annals of the Rheumatic Diseases*, vol. 77, no. 5, pp. 636–643, 2018.
- [9] R. H. J. A. Slart, Writing Group, Reviewer Group et al., "FDG-PET/CT(A) imaging in large vessel vasculitis and polymyalgia rheumatica: joint procedural recommendation of the EANM, SNMMI, and the PET interest group (PIG), and endorsed by the ASNC," *European Journal of Nuclear Medicine and Molecular Imaging*, vol. 45, no. 7, pp. 1250–1269, 2018.
- [10] M. Soussan, N. Abisror, S. Abad et al., "FDG-PET/CT in patients with ANCA-associated vasculitis: case-series and literature review," *Autoimmunity Reviews*, vol. 13, no. 2, pp. 125–131, 2014.
- [11] M. J. Kemna, F. Vanderghenst, S. Vöö et al., "Positron emission tomography scanning in anti-neutrophil cytoplasmic antibodies-associated vasculitis," *Medicine*, vol. 94, no. 20, p. e747, 2015.
- [12] R. A. Luqmani, R. Suppiah, P. C. Grayson, P. A. Merkel, and R. Watts, "Nomenclature and classification of vasculitis—update on the ACR/EULAR diagnosis and classification of vasculitis study (DCVAS)," *Clinical and Experimental Immunology*, vol. 164, no. 1, pp. 11–13, 2011.
- [13] F. Buttgereit, C. Dejaco, E. L. Matteson, and B. Dasgupta, "Polymyalgia rheumatica and giant cell arteritis," *JAMA*, vol. 315, no. 22, p. 2442, 2016.
- [14] F. Muratore, G. Pazzola, A. Soriano et al., "Unmet needs in the pathogenesis and treatment of vasculitides," *Clinical Reviews in Allergy and Immunology*, vol. 54, no. 2, pp. 244–260, 2018.
- [15] B. D. Nielsen, L. C. Gormsen, I. T. Hansen, K. K. Keller, P. Therkildsen, and E.-M. Hauge, "Three days of high-dose glucocorticoid treatment attenuates large-vessel  $^{18}\text{F}$ -FDG uptake in large-vessel giant cell arteritis but with a limited impact on diagnostic accuracy," *European Journal of Nuclear Medicine and Molecular Imaging*, vol. 45, no. 7, pp. 1119–1128, 2018.
- [16] D. Blockmans, L. De Ceuninck, S. Vanderschueren, D. Knockaert, L. Mortelmans, and H. Bobbaers, "Repetitive  $^{18}\text{F}$ -fluorodeoxyglucose positron emission tomography in giant cell arteritis: a prospective study of 35 patients," *Arthritis and Rheumatism*, vol. 55, no. 1, pp. 131–137, 2006.
- [17] S. Imfeld, C. Rottenburger, E. Schegk et al., "[ $^{18}\text{F}$ ]FDG positron emission tomography in patients presenting with suspicion of giant cell arteritis—lessons from a vasculitis clinic," *European Heart Journal-Cardiovascular Imaging*, vol. 19, no. 8, pp. 933–940, 2017.
- [18] A. H. Clifford, E. M. Murphy, S. C. Burrell et al., "Positron emission tomography/computerized tomography in newly diagnosed patients with giant cell arteritis who are taking glucocorticoids," *The Journal of Rheumatology*, vol. 44, no. 12, pp. 1859–1866, 2017.
- [19] S. P. Salomäki, A. Saraste, J. Kemppainen et al., " $^{18}\text{F}$ -FDG positron emission tomography/computed tomography in infective endocarditis," *Journal of Nuclear Cardiology*, vol. 24, no. 1, pp. 195–206, 2017.
- [20] S. P. Salomäki, U. Hohenthal, J. Kemppainen, L. Pirila, and A. Saraste, "Visualization of pericarditis by fluorodeoxyglucose PET," *European Heart Journal-Cardiovascular Imaging*, vol. 15, no. 3, p. 291, 2014.
- [21] S. P. Salomäki, J. Kemppainen, H. Aho et al., "Widespread vascular inflammation in a patient with antineutrophil cytoplasmic antibody-associated vasculitis as detected by positron emission tomography," *European Journal of Nuclear*

- Medicine and Molecular Imaging*, vol. 41, no. 11, pp. 2167-2168, 2014.
- [22] S. P. Salomäki, J. Kemppainen, U. Hohenthal et al., "Head-to-head comparison of  $^{68}\text{Ga}$ -citrate and  $^{18}\text{F}$ -FDG PET/CT for detection of infectious foci in patients with *Staphylococcus aureus* bacteraemia," *Contrast Media & Molecular Imaging*, vol. 2017, Article ID 3179607, 8 pages, 2017.
- [23] G. G. Hunder, D. A. Bloch, B. A. Michel et al., "The American college of rheumatology 1990 criteria for the classification of giant cell arteritis," *Arthritis and Rheumatism*, vol. 33, no. 8, pp. 1122-1128, 1990.
- [24] J. F. Fries, G. G. Hunder, D. A. Bloch et al., "The American college of rheumatology 1990 criteria for the classification of vasculitis: summary," *Arthritis and Rheumatism*, vol. 33, no. 8, pp. 1135-1136, 1990.
- [25] F. Jamar, J. Buscombe, A. Chiti et al., "EANM/SNMMI guideline for  $^{18}\text{F}$ -FDG use in inflammation and infection," *Journal of Nuclear Medicine*, vol. 54, no. 4, pp. 647-658, 2013.
- [26] I. Martínez-Rodríguez, M. Jiménez-Alonso, R. Quirce et al., " $^{18}\text{F}$ -FDG PET/CT in the follow-up of large-vessel vasculitis: a study of 37 consecutive patients," *Seminars in Arthritis and Rheumatism*, vol. 47, no. 4, pp. 530-537, 2018.
- [27] V. Schönau, K. Vogel, M. Englbrecht et al., "The value of  $^{18}\text{F}$ -FDG-PET/CT in identifying the cause of fever of unknown origin (FUO) and inflammation of unknown origin (IUO): data from a prospective study," *Annals of the Rheumatic Diseases*, vol. 77, no. 1, pp. 70-77, 2018.
- [28] H. Balink, N. J. G. M. Veeger, R. J. Bennink et al., "The predictive value of C-reactive protein and erythrocyte sedimentation rate for  $^{18}\text{F}$ -FDG PET/CT outcome in patients with fever and inflammation of unknown origin," *Nuclear Medicine Communications*, vol. 36, no. 6, pp. 604-609, 2015.
- [29] N. D. Papatasiou, Y. Du, L. J. Menezes et al., " $^{18}\text{F}$ -fluorodeoxyglucose PET/CT in the evaluation of large-vessel vasculitis: diagnostic performance and correlation with clinical and laboratory parameters," *The British Journal of Radiology*, vol. 85, no. 1014, pp. e188-e194, 2012.

## Review Article

# Diagnostic Performance of $^{18}\text{F}$ -FDG PET/CT in Infectious and Inflammatory Diseases according to Published Meta-Analyses

Giorgio Treglia <sup>1,2,3</sup>

<sup>1</sup>Clinic of Nuclear Medicine and PET/CT Center, Imaging Institute of Southern Switzerland, Ente Ospedaliero Cantonale, Bellinzona and Lugano, Switzerland

<sup>2</sup>Health Technology Assessment Unit, Ente Ospedaliero Cantonale, Bellinzona, Switzerland

<sup>3</sup>Department of Nuclear Medicine and Molecular Imaging, Lausanne University Hospital, University of Lausanne, Lausanne, Switzerland

Correspondence should be addressed to Giorgio Treglia; [giorgiomednuc@libero.it](mailto:giorgiomednuc@libero.it)

Received 20 January 2019; Revised 4 April 2019; Accepted 14 July 2019; Published 25 July 2019

Guest Editor: Sarah Ohrndorf

Copyright © 2019 Giorgio Treglia. This is an open access article distributed under the Creative Commons Attribution License, which permits unrestricted use, distribution, and reproduction in any medium, provided the original work is properly cited.

**Purpose.** To date, several meta-analyses have reported data about the diagnostic performance of  $^{18}\text{F}$ -FDG PET/CT in infectious and inflammatory diseases. This article aims to summarize the published evidence-based data about the diagnostic performance of  $^{18}\text{F}$ -FDG PET/CT in this setting. **Methods.** A comprehensive computer literature search of meta-analyses published in PubMed/MEDLINE and Cochrane library database from January 2009 through December 2018 and regarding the diagnostic performance of  $^{18}\text{F}$ -FDG PET/CT in infectious and inflammatory diseases was carried out. This combination of key words was used: (i) “PET” OR “positron emission tomography” OR “FDG” OR “fluorodeoxyglucose” AND (ii) meta-analysis. Only records on inflammatory or infectious diseases were selected. **Results.** The diagnostic performance of  $^{18}\text{F}$ -FDG PET/CT in detecting inflammatory and infectious diseases has been summarized taking into account 36 meta-analyses published in the literature. Evidence-based data demonstrated good diagnostic performance of  $^{18}\text{F}$ -FDG PET/CT for several inflammatory and infectious diseases, in particular cardiovascular infectious and inflammatory diseases and some musculoskeletal infections. **Conclusions.** Evidence-based data about the diagnostic performance of  $^{18}\text{F}$ -FDG PET/CT in infectious and inflammatory diseases are increasing, with good diagnostic performance of this imaging method for some indications. More prospective multicenter studies and cost-effective analyses are warranted.

## 1. Introduction

Nuclear medicine techniques are noninvasive tools that can early detect pathophysiological changes in affected tissues in patients with inflammatory or infectious diseases. These changes usually occur before clinical onset of symptoms and before the development of anatomical changes detected by radiological techniques [1, 2]. Currently, hybrid imaging techniques as positron emission tomography/computed tomography (PET/CT) may provide functional and morphological information for early diagnosis of infectious and inflammatory diseases [1, 2].

Fluorine-18 fluorodeoxyglucose ( $^{18}\text{F}$ -FDG) is a radio-labelled glucose analogue taken up by cells via cell membrane

glucose transporters and subsequently phosphorylated with hexokinase inside most cells [3]. The ability of  $^{18}\text{F}$ -FDG PET/CT to identify sites of inflammation and infection is mainly related to the glycolytic activity of the cells involved in the inflammatory response [3].

$^{18}\text{F}$ -FDG PET/CT has been proposed for imaging of infectious or inflammatory diseases (Figure 1) because it has been demonstrated that cells involved in infection and inflammation, especially neutrophils and the monocyte/macrophage family, are able to express high levels of glucose transporters and hexokinase activity [3–5].

Enough evidence in the literature already exists about the usefulness of  $^{18}\text{F}$ -FDG PET/CT in the diagnosis and management of several infectious and inflammatory diseases [5].

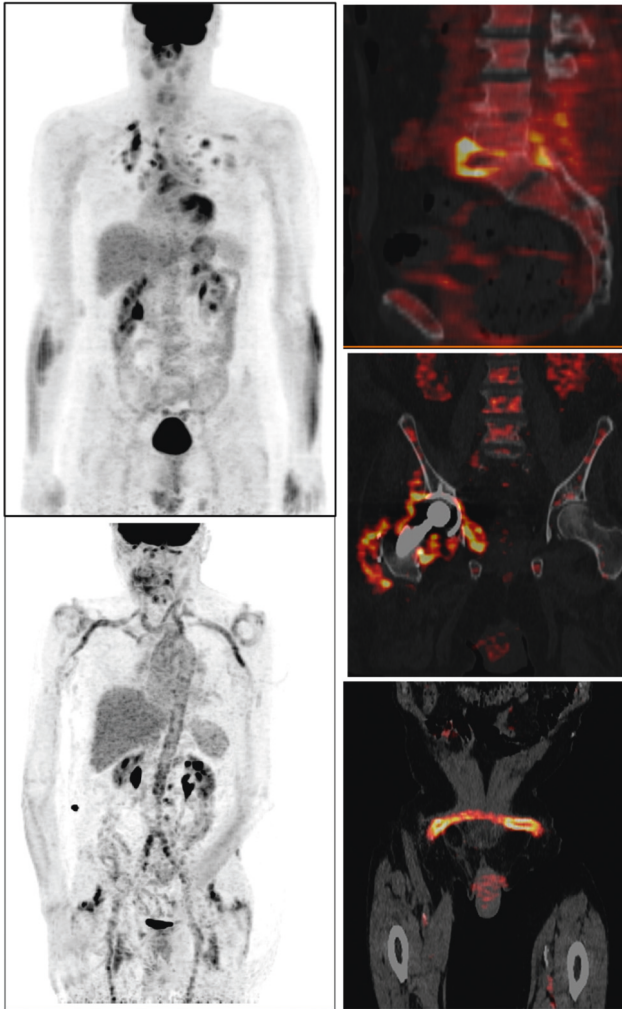


FIGURE 1: Examples of infectious and inflammatory diseases detected by  $^{18}\text{F}$ -FDG PET/CT: systemic sarcoidosis with pulmonary and mediastinal involvement (upper left), large vessel vasculitis associated with inflammatory rheumatic disease (lower left), spondylodiscitis (upper right), periprosthetic joint infection (middle right), and vascular graft infection (lower right).

The aim of this article is to summarize the findings of meta-analyses published in the last ten years about the diagnostic performance of  $^{18}\text{F}$ -FDG PET/CT in this setting.

## 2. Methods

A comprehensive computer literature search of PubMed/MEDLINE and Cochrane library databases was conducted to find recent published meta-analyses on the diagnostic performance of  $^{18}\text{F}$ -FDG PET/CT for the diagnosis of infectious and inflammatory diseases.

A search algorithm based on the combination of the following terms was used: (i) “PET” OR “positron emission tomography” OR “FDG” OR “fluorodeoxyglucose” AND (ii) meta-analysis. The literature search was updated until December 31<sup>st</sup>, 2018. No language restriction was used. Recent meta-analyses published in the last ten years and investigating the diagnostic performance of  $^{18}\text{F}$ -FDG PET/

CT in infectious or inflammatory diseases were eligible for inclusion. Titles and abstracts of the retrieved articles were reviewed, applying the inclusion criteria mentioned above.

For each selected meta-analysis, information was collected about basic study characteristics (disease evaluated, authors, year of publication, number of original articles included, and number of patients included) and pooled diagnostic performance measures including 95% confidence interval values (95% CI).

Main findings of the selected meta-analyses were briefly described.

## 3. Results

From the comprehensive computer literature search from PubMed/MEDLINE and Cochrane databases, 36 meta-analyses were selected and retrieved in full-text version [6–41]. The characteristics of the selected articles are presented in Table 1 and summarized here below.

**3.1. Fever of Unknown Origin (FUO).** Fever of unknown origin (FUO) is a very precise entity, as described in the literature. FUO is commonly defined as temperature  $\geq 38.3^\circ\text{C}$  on at least two occasions, duration of illness  $\geq 3$  weeks or multiple febrile episodes in  $\geq 3$  weeks, not immunocompromised patient, and uncertain diagnosis despite thorough history-taking, physical examination, and obligatory investigations [42]. The diagnosis in patients with FUO is a challenging medical problem; the causes of FUO may be infectious diseases, noninfectious inflammatory diseases, or tumours, and  $^{18}\text{F}$ -FDG PET/CT detecting foci of increased glucose metabolism may be used for revealing the source of fever [42]. Several meta-analyses have estimated the diagnostic performance of  $^{18}\text{F}$ -FDG PET/CT in the assessment of FUO unidentified by conventional workup [6–12].

Dong et al. firstly reported that the pooled sensitivity and specificity of  $^{18}\text{F}$ -FDG PET/CT for the detection of FUO were 98.2% (95% CI: 93.6–99.8) and 85.9% (95% CI: 75–93.4), respectively. Therefore, this method should be considered among the first diagnostic tools for patients with FUO in whom conventional diagnostics have been unsuccessful [6].

Hao et al. confirmed the high sensitivity of  $^{18}\text{F}$ -FDG PET/CT for the diagnosis of patients with FUO (pooled value: 85%; 95% CI: 81–88), but the possibility of false-positive results should be kept in mind [7].

Another meta-analysis demonstrated that abnormal  $^{18}\text{F}$ -FDG PET/CT findings are associated with a substantially increased final diagnostic rate in FUO (pooled odds ratio: 8.94; 95% CI: 4.18–19.12,  $p < 0.00001$ ). Consequently,  $^{18}\text{F}$ -FDG PET/CT could be considered for inclusion in the first-line diagnostic workup of FUO. Further randomized prospective studies with standardized  $^{18}\text{F}$ -FDG PET/CT are warranted to confirm this first-line position [8].

Tateuchi et al. reported that  $^{18}\text{F}$ -FDG PET/CT can be useful in identifying the source of fever in patients with classic FUO (immunocompetent patients). The summary sensitivity, specificity, and diagnostic yield of this method



TABLE 1: Continued.

Topic	Authors	Year	Articles included about $^{18}\text{F}$ -FDG PET/CT	Patients included	Sensitivity (95% CI)	Specificity (95% CI)	LR+ (95% CI)	LR- (95% CI)	DOR (95% CI)
Osteomyelitis	Wang et al.* [30]	2011	7	319	92.3% (86.7–96.1)	92% (87–95.6)	9.8 (6–16)	0.11 (0.07–0.2)	98 (42.8–224)
Osteomyelitis related to diabetic foot	Treglia et al.* [31]	2013	4	178	74% (60–85)	91% (85–96)	5.6 (2–15.3)	0.37 (0.1–1.35)	16.9 (2–139.6)
	Lauri et al.* [32]	2017	6	254	89% (68–97)	92% (85–96)	11 (4.7–25)	0.11 (0.03–0.4)	95 (18–504)
Prosthetic joint infection	Jin et al.* [33]	2014	14	838	86% (82–90)	86% (83–89)	NR	NR	NR
	Verberne et al.* [34]	2016	10	666	86% (80–90)	93% (90–95)	NR	NR	NR
	Verberne et al.* [35]	2017	5	179	70% (56–81)	84% (76–90)	NR	NR	NR
Spondylodiscitis	Prodromou et al.* [36]	2014	12	224	97% (83–100)	88% (74–95)	8.2 (3.5–18.9)	0.03 (0–0.21)	NR
	Yin et al.* [37]	2018	6	191	96% (84–99)	90% (79–96)	9.8 (4.4–22)	0.05 (0.01–0.19)	124 (39–394)
	Kim et al.* [38]	2018	7	212	95% (87–98)	88% (73–95)	7.6 (3.4–17.2)	0.05 (0.02–0.14)	141 (44–444)
Rheumatic diseases	Descamps et al.* [39]	2018	90	2300	NR	NR	NR	NR	NR
Inflammatory bowel diseases	Treglia et al.* [40]	2013	7	219	85% (81–88)	87% (84–90)	6.2 (2.9–13.4)	0.19 (0.1–0.34)	44.3 (11.8–167)
	Zhang et al.* [41]	2014	3	162	84% (78–89)	86% (81–89)	5.3 (1.3–22)	0.2 (0.07–0.6)	25.9 (2.8–238)

LR+ = positive likelihood ratio; LR- = negative likelihood ratio; DOR = diagnostic odds ratio; 95% CI = 95% confidence interval; NR = not reported; CIED = cardiovascular implantable electronic device; GCA = giant cell arteritis; TA = Takayasu arteritis; TA<sup>+</sup> = Takayasu arteritis using National Health Institute scale; \*both PET and PET/CT are included.

were 86% (95% CI: 81–90), 52% (95% CI: 36–67), and 58% (95% CI: 51–64), respectively. The contribution of  $^{18}\text{F}$ -FDG PET/CT may be limited in clinical settings in which infectious and neoplastic causes are less common. Indirect comparisons of test performance suggested that  $^{18}\text{F}$ -FDG PET/CT outperformed standalone  $^{18}\text{F}$ -FDG PET, gallium-67 scintigraphy, and radiolabelled leukocyte scintigraphy in detecting causes of FUO. Studies using standardized diagnostic algorithms are needed to determine the optimal timing for testing and to assess the impact of tests on management decisions and patient-relevant outcomes [9].

Recently, Bharucha et al. reported an overall diagnostic contribution of 56% (95% CI: 50–61) of  $^{18}\text{F}$ -FDG PET/CT in all patients with FUO. In a subgroup analysis taking into account previous investigations, the diagnostic yield/added contribution of  $^{18}\text{F}$ -FDG PET/CT over CT was 32% (95% CI: 22–44). The pooled proportion of abnormal  $^{18}\text{F}$ -FDG PET/CT in patients with FUO was 69% (95% CI: 63–75); the higher proportion of abnormal scans was accounted for by a proportion of false-positive abnormal scans with no contribution to the final diagnosis, with an overall result of 9% (95% CI: 5–14). The authors concluded that there is insufficient evidence to support the value of  $^{18}\text{F}$ -FDG PET/CT in investigative algorithms of FUO [10].

Conversely, in an updated meta-analysis on patients with FUO or inflammation of unknown origin (IUO),  $^{18}\text{F}$ -FDG PET/CT was demonstrated to be very helpful for recognizing

and excluding diseases, directing further diagnostic decisions and avoiding unnecessary invasive examinations. The pooled sensitivity and specificity were 84% (95% CI: 79–89) and 63% (95% CI: 49–75), respectively. Based on these findings, the authors recommended  $^{18}\text{F}$ -FDG PET/CT among the first-line diagnostic tools for patients with FUO and IUO [11].

Lastly, it has been recently demonstrated that patients with negative  $^{18}\text{F}$ -FDG PET/CT results were significantly more likely to present with spontaneous fever regression than those with positive  $^{18}\text{F}$ -FDG PET/CT results (summary relative risk = 5.6; 95% CI: 3.4–9.2;  $p < 0.001$ ) [12].

Overall, there is no agreement among the selected meta-analyses about the added value of  $^{18}\text{F}$ -FDG PET/CT in patients with FUO. The main drawback of the meta-analyses evaluating the diagnostic performance of  $^{18}\text{F}$ -FDG PET/CT for this specific indication is that they include articles without real FUO patients or with highly variable definitions of FUO; therefore, related meta-analyses could be not accurate in this regard [43].

Furthermore, the diagnostic yield of  $^{18}\text{F}$ -FDG PET/CT in patients with FUO should take into account not only the positive cases but also the true negative cases as patients with a negative  $^{18}\text{F}$ -FDG PET/CT are likely to have a favourable course [12]. Considering that 30–50% of patients with FUO will not have a final diagnosis and do well after prolonged follow-up without further treatment, the diagnostic yield of

$^{18}\text{F}$ -FDG PET/CT might be even higher compared to that reported in the selected meta-analyses [43].

**3.2. Large Vessel Vasculitis (LVV).** Large vessel vasculitis (LVV) is defined as an inflammatory disease mainly affecting the large arteries, with two major variants, Takayasu arteritis (TA) and giant cell arteritis (GCA). GCA often coexists with polymyalgia rheumatica (PMR) in the same patient, since both belong to the same disease spectrum [44].  $^{18}\text{F}$ -FDG PET/CT may demonstrate increased radiopharmaceutical uptake in the vascular wall of large vessels in patients with LVV; therefore, this method may be used for diagnosis, monitoring of disease activity, and evaluating disease progression in LVV [44–47], and several meta-analyses have assessed the role of this imaging method in this setting [13–19].

First meta-analyses including both  $^{18}\text{F}$ -FDG PET and PET/CT studies reported a valuable diagnostic performance of these methods in patients with GCA with a pooled sensitivity and specificity of 80% (95% CI: 63–91) and 89% (95% CI: 78–94), respectively [13], and a moderate value of these methods in assessing TA activity, with a pooled sensitivity and specificity of 70.1% (95% CI: 58.6–80) and 77.2% (95% CI: 64.2–87.3), respectively [14].

In a meta-analysis of Soussan et al. including both  $^{18}\text{F}$ -FDG PET and PET/CT studies, these imaging methods showed good performances in the diagnosis of LVV, with higher accuracy in GCA patients than in TA patients. A vascular uptake equal to or higher than the liver uptake appeared to be a good criterion for the diagnosis of vascular inflammation.  $^{18}\text{F}$ -FDG PET or PET/CT showed high sensitivity and specificity for the diagnosis of LVV in GCA patients in comparison to controls, with pooled values of 90% (95% CI: 79–93) and 98% (95% CI: 94–99), respectively.  $^{18}\text{F}$ -FDG PET or PET/CT had a pooled sensitivity of 87% (95% CI: 78–93) and specificity of 73% (95% CI: 63–81) for the assessment of disease activity in TA, with up to 84% of specificity in studies using National Institutes of Health criteria as the disease activity assessment scale [15].

Another meta-analysis by Lee et al. confirmed that  $^{18}\text{F}$ -FDG PET/CT has good diagnostic accuracy for LVV with a pooled sensitivity and specificity of 83.9% (95% CI: 71.7–92.4) and 87.2% (95% CI: 72.6–95.7), respectively [16].

In a recent meta-analysis, the pooled sensitivity and specificity of  $^{18}\text{F}$ -FDG PET or PET/CT for detecting active disease in TA compared to clinical assessment were 81% (95% CI: 69–89) and 74% (95% CI: 55–86), respectively. Active disease by  $^{18}\text{F}$ -FDG PET or PET/CT was also associated with elevations of acute phase reactants, as C-reactive protein (CRP) and erythrocyte sedimentation rate (ESR) [17]. Conversely, in another meta-analysis by Gomez et al. about the association between the CRP value and  $^{18}\text{F}$ -FDG PET or PET/CT vascular positivity in TA, CRP concentration only moderately reflected the  $^{18}\text{F}$ -FDG PET vascular positivity in TA, suggesting dissociated information [18]. More prospective studies are needed to assess the value of  $^{18}\text{F}$ -FDG PET/CT as an independent biomarker for subtle

vascular wall inflammation detection in patients with TA [18].

Lastly, an updated meta-analysis confirmed that  $^{18}\text{F}$ -FDG PET or PET/CT has a good performance for the detection of active disease in patients with LVV with a pooled sensitivity and specificity of 88% (95% CI: 79–93) and 81% (95% CI: 64–91), respectively. Therefore,  $^{18}\text{F}$ -FDG PET/CT could be suggested as a surrogate biomarker for assessment of disease activity of LVV during or after immunosuppressive therapy, but further studies are warranted to determine if PET-based treatment of LVV can improve outcomes [19].

Several factors may significantly influence the arterial wall  $^{18}\text{F}$ -FDG uptake and must be taken into consideration for interpretation of  $^{18}\text{F}$ -FDG PET/CT in LVV [44]. Many PET interpretation criteria have been proposed; nevertheless, evidence supports the use of a visual  $^{18}\text{F}$ -FDG PET grading scale with vascular  $^{18}\text{F}$ -FDG uptake  $\geq$  liver uptake as LVV positivity criterion [44]. Atherosclerotic vascular uptake may be a source of false positivity for LVV evaluation, despite a classical patchy uptake pattern. Taking these considerations into account, vascular inflammation in LVV on  $^{18}\text{F}$ -FDG PET classically appears as a smooth linear pattern [44].

Patients with suspected LVV often immediately receive high-dose glucocorticoids before  $^{18}\text{F}$ -FDG PET/CT, and this may reduce the intensity of arterial  $^{18}\text{F}$ -FDG uptake. The accuracy of  $^{18}\text{F}$ -FDG PET/CT can therefore vary in relation to the delay between the initiation of immunosuppressive therapy and  $^{18}\text{F}$ -FDG PET/CT [44].

For the precise evaluation of diagnostic accuracy of  $^{18}\text{F}$ -FDG PET/CT in patients with LVV, it should be taken into account that in some patients,  $^{18}\text{F}$ -FDG PET/CT may be the only modality allowing for the diagnosis of LVV, and therefore it cannot be compared to a gold standard [44].

Overall, based on the available evidence,  $^{18}\text{F}$ -FDG PET/CT has demonstrated high diagnostic performance for the detection of LVV. Further studies are needed to select the most clinically relevant and reproducible criteria for defining the presence of LVV with  $^{18}\text{F}$ -FDG PET/CT, as well as to test the clinical impact of  $^{18}\text{F}$ -FDG PET/CT on the management of patients with suspected LVV [44].

**3.3. Infective Endocarditis (IE) and Cardiovascular Implantable Electronic Device (CIED) Infections.** Infective endocarditis (IE) is a serious and potentially life-threatening condition. The current diagnosis of IE is based on the modified Duke criteria, which has approximately 80% sensitivity for the diagnosis of native valve endocarditis (NVE), with lower sensitivity for the diagnosis of prosthetic valve endocarditis (PVE) and culture-negative endocarditis [48, 49]. Noninvasive imaging modalities may improve diagnosis of infective endocarditis (IE) [48, 49]. In particular,  $^{18}\text{F}$ -FDG PET/CT is currently included as diagnostic tool in the diagnostic flow chart for IE [48–51], and some meta-analyses have evaluated the diagnostic performance of this method in patients with IE or CIED infections [20–24].

A first meta-analysis published in 2016 demonstrated that the overall diagnostic performance of  $^{18}\text{F}$ -FDG PET/CT for the diagnosis of IE was not high due to the low sensitivity: pooled sensitivity and specificity were 61% (95% CI: 52–88) and 88% (95% CI: 80–93), respectively. However the diagnostic performance of  $^{18}\text{F}$ -FDG PET/CT increased in the subgroup of patients with PVE [20].

Mahmood et al. demonstrated that  $^{18}\text{F}$ -FDG PET/CT may be a useful adjunctive diagnostic tool in the evaluation of diagnostically challenging cases of IE, particularly in PVE. The pooled sensitivity and specificity of  $^{18}\text{F}$ -FDG PET/CT for diagnosis of IE were 76.8% (95% CI: 71.8–81.4) and 77.9% (95% CI: 71.9–83.2), respectively. Diagnostic accuracy was improved for PVE with pooled sensitivity of 80.5% (95% CI: 74.1–86) and pooled specificity of 73.1% (95% CI: 63.8–81.2). More recent studies published from 2015 to 2017 reported a higher pooled sensitivity of 81.3% (95% CI: 74.3–87) and specificity of 79% (95% CI: 71.2–85.5). The majority of the recent studies were prospective and used a specific protocol (i.e., a low-carbohydrate fat-allowed diet for at least 24 hours prior to imaging, a prolonged fasting prior to imaging, and/or an intravenous heparin bolus prior to  $^{18}\text{F}$ -FDG administration).  $^{18}\text{F}$ -FDG PET/CT also has the potential to detect clinically relevant extracardiac foci of infection, malignancy, and other sources of inflammation leading to more appropriate treatment regimens and surgical intervention. Additional extracardiac foci of infection were found on 17% of patients in this meta-analysis [21].

In another meta-analysis, Juneau et al. demonstrated that  $^{18}\text{F}$ -FDG PET/CT has a good diagnostic accuracy for the diagnosis of IE if adequate patient preparation for suppression of physiological myocardial  $^{18}\text{F}$ -FDG uptake was performed, including prolonged fasting at least 12 hours and/or heparin injection before  $^{18}\text{F}$ -FDG administration and/or high-fat carbohydrate-restricted protein-permitted diet. Pooled sensitivity of  $^{18}\text{F}$ -FDG PET/CT performed with adequate cardiac preparation for the diagnosis of IE was 81% (95% CI: 73–86) and pooled specificity was 85% (95% CI: 78–91). In the subgroup of patients with PVE, the pooled sensitivity was 85% (95% CI: 77–91) but specificity was 81% (95% CI: 72–88). Therefore,  $^{18}\text{F}$ -FDG PET/CT may be useful in the investigation of IE and should be considered in cases where the diagnosis is uncertain [22].

$^{18}\text{F}$ -FDG PET/CT may be helpful in the diagnosis of CIED infections, particularly in patients with the absence of localizing signs or definitive echocardiographic findings. In a recent meta-analysis, Mahmood et al. reported a pooled sensitivity and specificity of  $^{18}\text{F}$ -FDG PET/CT in the diagnosis of CIED infections of 85% (95% CI: 80–89) and 90% (95% CI: 84–94), respectively.  $^{18}\text{F}$ -FDG PET/CT demonstrated a higher sensitivity of 96% (95% CI: 86–99) and specificity of 97% (95% CI: 86–99) for diagnosis of pocket infections. Diagnostic accuracy for lead infections or CIED-IE was lower with pooled sensitivity of 76% (95% CI: 65–85) and specificity of 83% (95% CI: 72–90). In the subgroup of studies that described use of any myocardial suppression protocol, the pooled sensitivity was 92% (95% CI: 85–96) and the pooled specificity was 81% (95% CI: 71–89) [23].

Another recent meta-analysis confirmed the high diagnostic performance of  $^{18}\text{F}$ -FDG PET/CT for the diagnosis of CIED infections with a pooled sensitivity of 87% (95% CI: 82–91) and a pooled specificity of 94% (95% CI: 88–98). Pooled sensitivity and specificity for diagnosis of pocket/generator related CIED infections were 93% (95% CI: 84–98) and 98% (95% CI: 88–100), respectively. Pooled sensitivity and specificity for diagnosis of lead or IE-related CIED infection were 65% (95% CI: 53–76) and 88% (95% CI: 77–94), respectively [24].

Overall,  $^{18}\text{F}$ -FDG PET/CT demonstrated a good diagnostic performance in patients with IE and CIED infections with higher diagnostic accuracy if adequate patient preparation for suppression of physiological myocardial  $^{18}\text{F}$ -FDG uptake was performed.

**3.4. Vascular Graft Infection (VGI).** Vascular graft infection (VGI), a serious complication in vascular surgery, has a high morbidity and mortality rate. The diagnosis is complicated by nonspecific symptoms and challenged by the variable accuracy of different imaging techniques [25, 52]. A recent meta-analysis demonstrated a good diagnostic performance of  $^{18}\text{F}$ -FDG PET/CT in patients with VGI with a pooled sensitivity and specificity of 95% (95% CI: 87–99) and 80% (95% CI: 69–89), respectively [25].

Another recent meta-analysis investigating the diagnostic accuracy of  $^{18}\text{F}$ -FDG PET/CT in VGI reported a pooled sensitivity and specificity for focal  $^{18}\text{F}$ -FDG uptake of 97% (95% CI: 89–99) and 89% (95% CI: 70–96), respectively [26].

One of the factors influencing the  $^{18}\text{F}$ -FDG uptake in patients with suspicious VGI is the time at which  $^{18}\text{F}$ -FDG PET/CT is performed after surgery. In fact,  $^{18}\text{F}$ -FDG uptake reaches its peak in the first few weeks after surgery and tends towards normal values around 4 weeks postoperatively, even if long-lasting physiologic activity has also been described. If  $^{18}\text{F}$ -FDG PET/CT is performed in cases of recently implanted grafts, increased  $^{18}\text{F}$ -FDG uptake can occur in uninfected grafts leading to false-positive  $^{18}\text{F}$ -FDG PET/CT findings for VGI [26].

False-negative  $^{18}\text{F}$ -FDG PET/CT findings in VGI may occur mainly because of the use of antibiotics prior to imaging, thus lowering the metabolic activity expected in infections and lowering the  $^{18}\text{F}$ -FDG uptake [26].

Variable interpretation criteria have been used to assess VGI by  $^{18}\text{F}$ -FDG PET/CT. The sensitivity and specificity of  $^{18}\text{F}$ -FDG PET/CT may therefore vary based on the criteria used [26]. A consensus about the parameters used for interpretation of the results would lead to better diagnostic accuracy, and this could be increased by performing the scan prior to antimicrobial treatment. Results from larger prospective studies are warranted [26].

**3.5. Sarcoidosis.** Sarcoidosis is a multisystem chronic inflammatory disease of unknown etiology characterized by widespread growth of noncaseating granulomas. The diagnosis of sarcoidosis is based on clinical and imaging presentation, histological confirmation, and the absence of

alternative diseases. Imaging techniques may play a role in the diagnostic workup of patients with sarcoidosis to assess disease extent and activity and treatment response evaluation [53]. The role of  $^{18}\text{F}$ -FDG PET/CT in patients with sarcoidosis is well established [54, 55]. Based on evidence-based data, the recommendations for use of  $^{18}\text{F}$ -FDG PET/CT in patients with sarcoidosis could be the following: evaluation of inflammatory active disease in patients with persistent symptoms and negative serologic markers; assessment of inflammation in radiologic stage IV sarcoidosis with lung fibrosis; evaluation of inflammatory active extrathoracic sites of sarcoidosis or assessment of cardiac sarcoidosis (especially in patients with implanted pacemakers); identification of active sites for diagnostic biopsy not revealed by other methods; and evaluation of treatment response in refractory sarcoidosis [54].

The role of  $^{18}\text{F}$ -FDG PET/CT in cardiac sarcoidosis is currently under active investigation [56], and some meta-analyses have addressed the diagnostic performance of  $^{18}\text{F}$ -FDG PET/CT in this setting [27–29].

In the meta-analysis of Youssef et al., the pooled sensitivity and specificity of  $^{18}\text{F}$ -FDG PET or PET/CT for diagnosis of cardiac sarcoidosis were 89% (95% CI: 79–96) and 78% (95% CI: 68–86), respectively [27].

Tang et al. demonstrated that the diagnostic accuracy of  $^{18}\text{F}$ -FDG PET/CT for cardiac sarcoidosis depends on adequate suppression of physiological cardiac glucose uptake. Overall,  $^{18}\text{F}$ -FDG PET/CT had a pooled sensitivity of 75% (95% CI: 69–80) and a pooled specificity of 81% (95% CI: 76–85) for the diagnosis of cardiac sarcoidosis. This modest diagnostic accuracy was attributed to the inclusion of studies in which a short fasting duration before scanning likely influenced its sensitivity. Excluding studies without adequate myocardial suppression resulted in a pooled sensitivity of 81% (95% CI: 76–86) and a pooled specificity of 82% (95% CI: 77–86). Fasting for at least 12 hours before scanning or a high-fat low-carbohydrate diet given at 3 to 6 hours before imaging or heparin infusion before imaging has shown to improve the diagnostic accuracy of  $^{18}\text{F}$ -FDG PET/CT in cardiac sarcoidosis [28].

Lastly, an updated meta-analysis on the diagnostic performance of  $^{18}\text{F}$ -FDG PET or PET/CT in cardiac sarcoidosis demonstrated a pooled sensitivity and specificity of 84% (95% CI: 71–91) and 83% (95% CI: 74–89), respectively. The presence of combined myocardial perfusion imaging improved the diagnostic accuracy of  $^{18}\text{F}$ -FDG PET/CT for diagnosis of cardiac sarcoidosis. Nevertheless, further large multicenter studies in this setting are needed [29].

**3.6. Musculoskeletal Infections.** Musculoskeletal infections are a serious problem in healthcare. Establishing the correct diagnosis is often difficult and may have a huge impact on daily life. Treatment of a musculoskeletal infection often requires a long time and/or costly procedures which can be avoided if musculoskeletal infection is excluded [57]. On the other hand, timely identification and precise localization of musculoskeletal infections by imaging techniques are critical for early initiation of treatment and can have a significant

impact on patient outcome. In this setting, nuclear medicine and radiological imaging are complementary techniques [57]. In particular, several meta-analyses have investigated the diagnostic performance of  $^{18}\text{F}$ -FDG PET/CT in patients with suspicious musculoskeletal infections [30–38].

Wang et al. calculated the diagnostic performance of  $^{18}\text{F}$ -FDG PET or PET/CT in patients with suspicious osteomyelitis reporting a high pooled sensitivity and specificity in this setting: pooled values were 92.3% (95% CI: 86.7–96.1) and 92% (95% CI: 87–95.6), respectively [30].

A first meta-analysis focused on the diagnostic performance of  $^{18}\text{F}$ -FDG PET or PET/CT in osteomyelitis related to diabetic foot reported a pooled sensitivity and specificity of 74% (95% CI: 60–85) and 91% (95% CI: 85–96), respectively [31]. An updated meta-analysis on the same topic demonstrated a pooled sensitivity of 89% (95% CI: 68–97) and a pooled specificity of 92% (95% CI: 85–96) [32].

Jin et al. calculated the diagnostic performance of  $^{18}\text{F}$ -FDG PET or PET/CT in detecting prosthetic infection after arthroplasty. They found a pooled sensitivity and specificity of 86% (95% CI: 82–90) and 86% (95% CI: 83–89), respectively. The pooled sensitivity of  $^{18}\text{F}$ -FDG PET or PET/CT in demonstrating hip and knee prosthetic infection was 88% (95% CI: 83–92) and 72% (95% CI: 58–84), respectively. The pooled specificity of  $^{18}\text{F}$ -FDG PET or PET/CT in demonstrating hip and knee prosthetic infection was 88% (95% CI: 84–91) and 80% (95% CI: 71–88), respectively [33].

A meta-analysis focused on periprosthetic hip infection confirmed the good diagnostic accuracy of  $^{18}\text{F}$ -FDG PET or PET/CT in this setting with pooled sensitivity and specificity of 86% (95% CI: 80–90) and 93% (95% CI: 90–95), respectively, using increased  $^{18}\text{F}$ -FDG uptake in the bone-prosthesis interface as the criterion for infection for the index test [34].

A meta-analysis focused on periprosthetic knee infection demonstrated a not optimal diagnostic accuracy of  $^{18}\text{F}$ -FDG PET or PET/CT in this setting with pooled sensitivity and specificity of 70% (95% CI: 56–81) and 84% (95% CI: 76–90) [35].

Some factors influencing the diagnostic performance of  $^{18}\text{F}$ -FDG PET/CT in patients with osteomyelitis should be underlined: first of all, several interpretation criteria of  $^{18}\text{F}$ -FDG PET have been used in the literature, by using visual and/or semiquantitative criteria, leading to different diagnostic accuracy values [30–35]. Furthermore, continuous physiologic  $^{18}\text{F}$ -FDG activity around the prostheses may be the cause of false-positive  $^{18}\text{F}$ -FDG PET/CT findings for periprosthetic infection [33–35].

$^{18}\text{F}$ -FDG PET or PET/CT has an excellent diagnostic performance in detecting infectious spondylodiscitis [58]. A first meta-analysis on  $^{18}\text{F}$ -FDG PET or PET/CT in patients with suspicious spondylodiscitis reported a pooled sensitivity and specificity of 97% (95% CI: 83–100) and 88% (95% CI: 74–95), respectively [36]. In this setting, the diagnostic performance of  $^{18}\text{F}$ -FDG PET or PET/CT was higher compared with magnetic resonance imaging (MRI). Considering studies comparing  $^{18}\text{F}$ -FDG PET or PET/CT and MRI, pooled sensitivity and specificity of  $^{18}\text{F}$ -FDG PET or PET/CT were 96% (95% CI: 84–99) and 90% (95% CI: 79–96), whereas the

pooled sensitivity and specificity of MRI were 76% (95% CI: 65–84) and 62% (95% CI: 45–77) [37]. Another recent meta-analysis confirmed the better diagnostic accuracy of  $^{18}\text{F}$ -FDG PET or PET/CT compared to MRI for the detection of spondylodiscitis: for  $^{18}\text{F}$ -FDG PET or PET/CT, pooled sensitivity and specificity were 95% (95% CI: 87–98) and 88% (95% CI: 73–95), respectively; and for MRI, pooled sensitivity and specificity were 85% (95% CI: 65–95) and 66% (95% CI: 48–80), respectively [38].

Overall, based on the available evidence,  $^{18}\text{F}$ -FDG PET/CT has demonstrated a good diagnostic performance for the detection of musculoskeletal infections.

**3.7. Inflammatory Rheumatic Diseases.** Molecular imaging methods, including  $^{18}\text{F}$ -FDG PET/CT, have been proposed for a better assessment of inflammatory rheumatic diseases [59].  $^{18}\text{F}$ -FDG uptake in the shoulders or hips was often reported in PMR (pooled prevalence: 76%), especially in periarticular sites (pooled prevalence: 84%). Furthermore, interspinous  $^{18}\text{F}$ -FDG uptake, demonstrating interspinous bursitis, is common in PMR (pooled prevalence: 67%). However, these findings are not very specific for PMR [39].

Patients with rheumatoid arthritis (RA) may also have interspinous  $^{18}\text{F}$ -FDG uptake (pooled prevalence: 34%) or articular  $^{18}\text{F}$ -FDG uptake in shoulders or hips (pooled prevalence: 66%) or in other articular regions (pooled prevalence: 78%). Articular  $^{18}\text{F}$ -FDG uptake is not specific for PMR or RA as it is common in other connective tissue diseases (pooled prevalence: 70%). Overall,  $^{18}\text{F}$ -FDG PET/CT is helpful in diagnostic research, but the interpretation of  $^{18}\text{F}$ -FDG uptake at each site is not characteristic of a specific inflammatory rheumatic disease [39].

**3.8. Inflammatory Bowel Diseases.**  $^{18}\text{F}$ -FDG PET/CT may also be used to image areas of active inflammation, such as those occurring in patients with active inflammatory bowel disease (IBD) as Crohn's disease and ulcerative colitis [60]. In this setting,  $^{18}\text{F}$ -FDG PET or PET/CT showed a good accuracy with a pooled sensitivity and specificity of 85% (95% CI: 81–88) and 87% (95% CI 84–90), respectively [40]. These findings were confirmed by another meta-analysis including prospective studies only [41]. Nevertheless, more prospective studies evaluating the role of  $^{18}\text{F}$ -FDG PET/CT for this indication are needed. Specific challenges for the use of  $^{18}\text{F}$ -FDG PET/CT in IBD are the physiological  $^{18}\text{F}$ -FDG uptake in the bowel and the movement of the bowel that may influence a correct coregistration of  $^{18}\text{F}$ -FDG PET and CT images [40].

## 4. Discussion

Overall, this article demonstrates that there is increasing evidence about the diagnostic performance of  $^{18}\text{F}$ -FDG PET/CT in infectious and inflammatory diseases, with good diagnostic accuracy values for some indications (Table 1). Awareness of the results described in this review has the potential to affect patient care by providing supportive evidence for more effective use of  $^{18}\text{F}$ -FDG PET/CT in the

diagnosis of some infectious or inflammatory diseases.  $^{18}\text{F}$ -FDG PET/CT may potentially be useful to direct therapeutic strategies improving patient outcome, but prospective outcome studies are needed in this setting. In fact, diagnostic accuracy of a test is not a measure of clinical effectiveness, and good diagnostic performance does not necessarily result in improved patient outcomes. Other factors beyond the diagnostic performance should influence the choice of an imaging modality in patients with infectious and inflammatory diseases (i.e., availability, radiation dose, safety, examination time, legal, organization and economic aspects, and cost-effectiveness).

Some limitations of the included meta-analyses should be underlined because they could limit definitive conclusions on the diagnostic performance of  $^{18}\text{F}$ -FDG PET/CT in infectious and inflammatory diseases. First of all, in some meta-analyses, a limited number of published articles (some of them with small sample size) were included reducing the statistical power of the analysis (Table 1).

In several meta-analyses, a considerable heterogeneity of diagnostic performance of  $^{18}\text{F}$ -FDG PET/CT among studies was found. Heterogeneity may represent a potential source of bias in a meta-analysis. This heterogeneity is likely to arise through baseline differences among the patients in the included studies, diversity in methodological aspects between different studies, and different study quality [61]. The diversity of the interpretation criteria used for  $^{18}\text{F}$ -FDG PET/CT may also have contributed to the heterogeneity among studies.

About the study design, only some articles included in each meta-analysis were prospective studies, influencing the overall quality of the meta-analysis and causing heterogeneity. Many of the included studies are small, single-centre, retrospective series limiting their applicability to a broader setting. In most of the included studies, the  $^{18}\text{F}$ -FDG PET/CT results were available to the clinicians caring for patients which may have influenced their decision making. Moreover, interpretation of imaging was often not blinded to the clinical scenario, which may have influenced reporting of  $^{18}\text{F}$ -FDG PET/CT results.

The lack of a reliable “gold standard” for the diagnosis of infection and inflammation could be another limitation of the described meta-analyses. The studies included in the meta-analyses used multiple and imperfect reference standards and were deemed likely to have produced biased results because of differential verification and incorporation of the  $^{18}\text{F}$ -FDG PET/CT result in the reference standard. Differential verification and incorporation bias are likely to lead to overestimation of test performance, and thus the summary estimates should be interpreted with caution [61].

Also, publication bias is a major concern in all meta-analyses as studies reporting significant findings are more likely to be published than those reporting nonsignificant results [61].

Some current indications of  $^{18}\text{F}$ -FDG PET/CT in infectious and inflammation were not evaluated by meta-analyses. In particular, septicemia and/or bacteremia of unknown origin is an important current field of use of  $^{18}\text{F}$ -FDG PET/CT [62–67]; furthermore, the diagnostic performance of  $^{18}\text{F}$ -FDG PET/CT

for infections caused by specific pathogens (i.e., fungal infections, mycobacteriosis, etc.) [68, 69] needs also to be evaluated through a meta-analytic approach.

Large multicenter prospective studies and in particular more cost-effective analyses comparing  $^{18}\text{F}$ -FDG PET/CT with other imaging modalities in infectious and inflammatory diseases are warranted. To this regard, cost-effective analyses on  $^{18}\text{F}$ -FDG PET/CT in patients with FUO and bacteremia are already available, demonstrating that  $^{18}\text{F}$ -FDG PET/CT appears to be a cost-effective imaging technique in these settings by avoiding unnecessary investigations and reducing the duration of hospitalization [70–73].

By using  $^{18}\text{F}$ -FDG PET/CT, it is difficult to distinguish sterile inflammation from inflammation caused by infection. Even though radiolabelled leukocytes are routinely used in clinical practice for this purpose, new radiopharmaceuticals including imaging agents targeting bacteria are currently investigated [74, 75]. A recent evidence-based review highlighted the availability of many promising PET radiopharmaceuticals for bacterial imaging despite some bias related to animal selection and index test, but few have been translated to human subjects. Results showed a lack of standardized infection models and experimental settings [75]. PET/CT using autologous leukocytes radiolabelled with  $^{18}\text{F}$ -FDG demonstrated a good diagnostic accuracy for the diagnosis of infectious diseases, but larger studies are needed [76].

Furthermore, radiopharmaceuticals beyond  $^{18}\text{F}$ -FDG have been developed for evaluating inflammatory diseases, in particular to define new strategies for imaging immune cells as well as tissue modifications induced by the inflammatory process [77].

The role of  $^{18}\text{F}$ -FDG PET/CT for assessing treatment response in infectious or inflammatory diseases is also promising [78]. However, there are currently no recommended imaging modalities to objectively evaluate the effectiveness of treatment. Therapeutic effectiveness is currently gauged by the patient's subjective clinical response [78].

Hybrid PET/MRI systems, combining functional information with high soft tissue contrast provided by MRI, are now available for clinical use. Although the role of  $^{18}\text{F}$ -FDG PET/MRI in infectious and inflammatory diseases is promising, these areas of clinical investigation are still in the early phase, and more evidence-based data are needed in this setting [79].

## Conflicts of Interest

The author declares no conflicts of interest.

## References

- [1] A. Signore, K. L. Anzola, S. Auletta et al., "Current status of molecular imaging in inflammatory and autoimmune disorders," *Current Pharmaceutical Design*, vol. 24, no. 7, pp. 743–753, 2018.
- [2] M. Sollini, C. Lauri, R. Boni, E. Lazzeri, P. A. Erba, and A. Signore, "Current status of molecular imaging in infections," *Current Pharmaceutical Design*, vol. 24, no. 7, pp. 754–771, 2018.
- [3] F. Jamar, J. Buscombe, A. Chiti et al., "EANM/SNMMI guideline for  $^{18}\text{F}$ -FDG use in inflammation and infection," *Journal of Nuclear Medicine*, vol. 54, no. 4, pp. 647–658, 2013.
- [4] S. Hess, A. Alavi, and S. Basu, "PET-based personalized management of infectious and inflammatory disorders," *PET Clinics*, vol. 11, no. 3, pp. 351–361, 2016.
- [5] A. W. Glaudemans, E. F. de Vries, F. Galli, R. A. Dierckx, R. H. Slart, and A. Signore, "The use of  $^{18}\text{F}$ -FDG-PET/CT for diagnosis and treatment monitoring of inflammatory and infectious diseases," *Clinical and Developmental Immunology*, vol. 2013, Article ID 623036, 14 pages, 2013.
- [6] M.-j. Dong, K. Zhao, Z.-f. Liu, G.-l. Wang, S.-y. Yang, and G.-j. Zhou, "A meta-analysis of the value of fluorodeoxyglucose-PET/PET-CT in the evaluation of fever of unknown origin," *European Journal of Radiology*, vol. 80, no. 3, pp. 834–844, 2011.
- [7] R. Hao, L. Yuan, Y. Kan, C. Li, and J. Yang, "Diagnostic performance of  $^{18}\text{F}$ -FDG PET/CT in patients with fever of unknown origin," *Nuclear Medicine Communications*, vol. 34, no. 7, pp. 682–688, 2013.
- [8] F. L. Besson, P. Chaumet-Riffaud, M. Playe et al., "Contribution of  $^{18}\text{F}$ -FDG PET in the diagnostic assessment of fever of unknown origin (FUO): a stratification-based meta-analysis," *European Journal of Nuclear Medicine and Molecular Imaging*, vol. 43, no. 10, pp. 1887–1895, 2016.
- [9] M. Takeuchi, I. J. Dahabreh, T. Nishashi, M. Iwata, G. M. Varghese, and T. Terasawa, "Nuclear imaging for classic fever of unknown origin: meta-analysis," *Journal of Nuclear Medicine*, vol. 57, no. 12, pp. 1913–1919, 2016.
- [10] T. Bharucha, A. Rutherford, S. Skeoch et al., "Diagnostic yield of FDG-PET/CT in fever of unknown origin: a systematic review, meta-analysis, and Delphi exercise," *Clinical Radiology*, vol. 72, no. 9, pp. 764–771, 2017.
- [11] Y. Kan, W. Wang, J. Liu, J. Yang, and Z. Wang, "Contribution of  $^{18}\text{F}$ -FDG PET/CT in a case-mix of fever of unknown origin and inflammation of unknown origin: a meta-analysis," *Acta Radiologica*, vol. 60, no. 6, pp. 716–725, 2018.
- [12] M. Takeuchi, T. Nishashi, A. Gafter-Gvili et al., "Association of  $^{18}\text{F}$ -FDG PET or PET/CT results with spontaneous remission in classic fever of unknown origin: a systematic review and meta-analysis," *Medicine*, vol. 97, no. 43, article e12909, 2018.
- [13] F. L. Besson, J.-J. Parienti, B. Bienvenu et al., "Diagnostic performance of  $^{18}\text{F}$ -fluorodeoxyglucose positron emission tomography in giant cell arteritis: a systematic review and meta-analysis," *European Journal of Nuclear Medicine and Molecular Imaging*, vol. 38, no. 9, pp. 1764–1772, 2011.
- [14] Y. Cheng, N. Lv, Z. Wang, B. Chen, and A. Dang, " $^{18}\text{F}$ -FDG-PET in assessing disease activity in Takayasu arteritis: a meta-analysis," *Clinical and Experimental Rheumatology*, vol. 31, no. 75, pp. S22–S27, 2013.
- [15] M. Soussan, P. Nicolas, C. Schramm et al., "Management of large-vessel vasculitis with FDG-PET," *Medicine*, vol. 94, no. 14, article e622, 2015.
- [16] Y. H. Lee, S. J. Choi, J. D. Ji, and G. G. Song, "Diagnostic accuracy of  $^{18}\text{F}$ -FDG PET or PET/CT for large vessel vasculitis," *Zeitschrift für Rheumatologie*, vol. 75, no. 9, pp. 924–931, 2016.
- [17] L. Barra, T. Kanji, J. Malette, and C. Pagnoux, "Imaging modalities for the diagnosis and disease activity assessment of Takayasu's arteritis: a systematic review and meta-analysis," *Autoimmunity Reviews*, vol. 17, no. 2, pp. 175–187, 2018.
- [18] L. Gomez, P. Chaumet-Riffaud, N. Noel et al., "Effect of CRP value on  $^{18}\text{F}$ -FDG PET vascular positivity in Takayasu arteritis: a systematic review and per-patient based meta-analysis,"

- European Journal of Nuclear Medicine and Molecular Imaging*, vol. 45, no. 4, pp. 575–581, 2018.
- [19] S.-W. Lee, S.-J. Kim, Y. Seo, S. Y. Jeong, B.-C. Ahn, and J. Lee, “F-18 FDG PET for assessment of disease activity of large vessel vasculitis: a systematic review and meta-analysis,” *Journal of Nuclear Cardiology*, vol. 26, no. 1, pp. 59–67, 2018.
- [20] J. Yan, C. Zhang, Y. Niu et al., “The role of  $^{18}\text{F}$ -FDG PET/CT in infectious endocarditis: a systematic review and meta-analysis,” *International Journal of Clinical Pharmacology and Therapeutics*, vol. 54, no. 5, pp. 337–342, 2016.
- [21] M. Mahmood, A. T. Kendi, S. Ajmal et al., “Meta-analysis of  $^{18}\text{F}$ -FDG PET/CT in the diagnosis of infective endocarditis,” *Journal of Nuclear Cardiology*, vol. 26, no. 3, pp. 922–935, 2017.
- [22] D. Juneau, M. Golfam, S. Hazra et al., “Molecular Imaging for the diagnosis of infective endocarditis: a systematic literature review and meta-analysis,” *International Journal of Cardiology*, vol. 253, pp. 183–188, 2018.
- [23] M. Mahmood, A. T. Kendi, S. Farid et al., “Role of  $^{18}\text{F}$ -FDG PET/CT in the diagnosis of cardiovascular implantable electronic device infections: a meta-analysis,” *Journal of Nuclear Cardiology*, vol. 26, no. 3, pp. 958–970, 2017.
- [24] D. Juneau, M. Golfam, S. Hazra et al., “Positron emission tomography and single-photon emission computed tomography imaging in the diagnosis of cardiac implantable electronic device infection: a systematic review and meta-analysis,” *Circulation: Cardiovascular Imaging*, vol. 10, no. 4, 2017.
- [25] E. I. Reinders Folmer, G. C. I. Von Meijenfheldt, M. J. Van der Laan et al., “Diagnostic imaging in vascular graft infection: a systematic review and meta-analysis,” *European Journal of Vascular and Endovascular Surgery*, vol. 56, no. 5, pp. 719–729, 2018.
- [26] D. Rojoa, N. Kontopodis, S. A. Antoniou, C. V. Ioannou, and G. A. Antoniou, “ $^{18}\text{F}$ -FDG PET in the diagnosis of vascular prosthetic graft infection: a diagnostic test accuracy meta-analysis,” *European Journal of Vascular and Endovascular Surgery*, vol. 57, no. 2, pp. 292–301, 2019.
- [27] G. Youssef, E. Leung, I. Mylonas et al., “The use of  $^{18}\text{F}$ -FDG PET in the diagnosis of cardiac sarcoidosis: a systematic review and metaanalysis including the Ontario experience,” *Journal of Nuclear Medicine*, vol. 53, no. 2, pp. 241–248, 2012.
- [28] R. Tang, J. T.-Y. Wang, L. Wang et al., “Impact of patient preparation on the diagnostic performance of  $^{18}\text{F}$ -FDG PET in cardiac sarcoidosis,” *Clinical Nuclear Medicine*, vol. 41, no. 7, pp. e327–e339, 2016.
- [29] S.-J. Kim, K. Pak, and K. Kim, “Diagnostic performance of F-18 FDG PET for detection of cardiac sarcoidosis; a systematic review and meta-analysis,” *Journal of Nuclear Cardiology*, 2019.
- [30] G.-l. Wang, K. Zhao, Z.-f. Liu, M.-j. Dong, and S.-y. Yang, “A meta-analysis of fluorodeoxyglucose-positron emission tomography versus scintigraphy in the evaluation of suspected osteomyelitis,” *Nuclear Medicine Communications*, vol. 32, no. 12, pp. 1134–1142, 2011.
- [31] G. Treglia, R. Sadeghi, S. Annunziata et al., “Diagnostic performance of Fluorine-18-Fluorodeoxyglucose positron emission tomography for the diagnosis of osteomyelitis related to diabetic foot: a systematic review and a meta-analysis,” *The Foot*, vol. 23, no. 4, pp. 140–148, 2013.
- [32] C. Lauri, M. Tamminga, A. W. J. M. Glaudemans et al., “Detection of osteomyelitis in the diabetic foot by imaging techniques: a systematic review and meta-analysis comparing MRI, white blood cell scintigraphy, and FDG-PET,” *Diabetes Care*, vol. 40, no. 8, pp. 1111–1120, 2017.
- [33] H. Jin, L. Yuan, C. Li, Y. Kan, R. Hao, and J. Yang, “Diagnostic performance of FDG PET or PET/CT in prosthetic infection after arthroplasty: a meta-analysis,” *Quarterly Journal of Nuclear Medicine and Molecular Imaging*, vol. 58, no. 1, pp. 85–93, 2014.
- [34] S. J. Verberne, P. G. Raijmakers, and O. P. P. Temmerman, “The accuracy of imaging techniques in the assessment of periprosthetic hip infection,” *Journal of Bone and Joint Surgery*, vol. 98, no. 19, pp. 1638–1645, 2016.
- [35] S. J. Verberne, R. J. A. Sonnega, O. P. P. Temmerman, and P. G. Raijmakers, “What is the accuracy of nuclear imaging in the assessment of periprosthetic knee infection? a meta-analysis,” *Clinical Orthopaedics and Related Research*, vol. 475, no. 5, pp. 1395–1410, 2017.
- [36] M. L. Prodromou, P. D. Ziakas, L. S. Poulou, P. Karsaliakos, L. Thanos, and E. Mylonakis, “FDG PET is a robust tool for the diagnosis of spondylodiscitis,” *Clinical Nuclear Medicine*, vol. 39, no. 4, pp. 330–335, 2014.
- [37] Y. Yin, X. Liu, X. Yang, J. Guo, Q. Wang, and L. Chen, “Diagnostic value of FDG-PET versus magnetic resonance imaging for detecting spondylitis: a systematic review and meta-analysis,” *Spine Journal*, vol. 18, no. 12, pp. 2323–2332, 2018.
- [38] S. J. Kim, K. Pak, K. Kim, and J. S. Lee, “Comparing the diagnostic accuracies of F-18 FDG PET and MRI for the detection of spondylodiscitis: a meta-analysis,” *Spine*, 2018.
- [39] L. Descamps, L. Olagne, C. Merlin, F. Cachin, M. Soubrier, and S. Mathieu, “Utility of PET/CT in the diagnosis of inflammatory rheumatic diseases: a systematic review and meta-analysis,” *Annals of the Rheumatic Diseases*, vol. 77, no. 11, p. e81, 2018.
- [40] G. Treglia, N. Quartuccio, R. Sadeghi et al., “Diagnostic performance of fluorine-18-fluorodeoxyglucose positron emission tomography in patients with chronic inflammatory bowel disease: a systematic review and a meta-analysis,” *Journal of Crohn’s and Colitis*, vol. 7, no. 5, pp. 345–354, 2013.
- [41] J. Zhang, L.-F. Li, Y.-J. Zhu et al., “Diagnostic performance of  $^{18}\text{F}$ -FDG-PET versus scintigraphy in patients with inflammatory bowel disease,” *Nuclear Medicine Communications*, vol. 35, no. 12, pp. 1233–1246, 2014.
- [42] I. J. E. Kouijzer, C. M. Mulders-Manders, C. P. Bleeker-Rovers, and W. J. G. Oyen, “Fever of unknown origin: the value of FDG-PET/CT,” *Seminars in Nuclear Medicine*, vol. 48, no. 2, pp. 100–107, 2018.
- [43] I. J. E. Kouijzer, J. W. M. van der Meer, W. J. G. Oyen, and C. P. Bleeker-Rovers, “Diagnostic yield of FDG-PET/CT in fever of unknown origin: a systematic review, meta-analysis, and Delphi exercise,” *Clinical Radiology*, vol. 73, no. 6, pp. 588–589, 2018.
- [44] R. H. J. A. Slart, Writing group, Reviewer group et al., “FDG-PET/CT(A) imaging in large vessel vasculitis and polymyalgia rheumatica: joint procedural recommendation of the EANM, SNMMI, and the PET Interest Group (PIG), and endorsed by the ASNC,” *European Journal of Nuclear Medicine and Molecular Imaging*, vol. 45, no. 7, pp. 1250–1269, 2018.
- [45] G. Treglia, M. V. Mattoli, L. Leccisotti, G. Ferraccioli, and A. Giordano, “Usefulness of whole-body fluorine-18-fluorodeoxyglucose positron emission tomography in patients with large-vessel vasculitis: a systematic review,” *Clinical Rheumatology*, vol. 30, no. 10, pp. 1265–1275, 2011.
- [46] G. Treglia, A. Versari, L. Giovanella, N. Pipitone, and C. Salvarani, “Is  $^{18}\text{F}$ -FDG PET a ‘potentially hazardous’ or an effective tool in evaluating patients with large-vessel vasculitis?,” *Clinical and Experimental Rheumatology*, vol. 31, no. 75, p. S93, 2013.

- [47] C. Dejaco, S. Ramiro, C. Duftner et al., "EULAR recommendations for the use of imaging in large vessel vasculitis in clinical practice," *Annals of the Rheumatic Diseases*, vol. 77, no. 5, pp. 636–643, 2018.
- [48] P. A. Erba, P. Lancellotti, I. Vilacosta et al., "Recommendations on nuclear and multimodality imaging in IE and CIED infections," *European Journal of Nuclear Medicine and Molecular Imaging*, vol. 45, no. 10, pp. 1795–1815, 2018.
- [49] A. Gomes, A. W. J. M. Glaudemans, D. J. Touw et al., "Diagnostic value of imaging in infective endocarditis: a systematic review," *Lancet Infectious Diseases*, vol. 17, no. 1, pp. e1–e14, 2017.
- [50] G. Treglia and F. Bertagna, "Factors influencing the sensitivity of  $^{18}\text{F}$ -FDG PET/CT in the detection of infective endocarditis," *European Journal of Nuclear Medicine and Molecular Imaging*, vol. 40, no. 7, pp. 1112–1113, 2013.
- [51] C. Caldarella, L. Leccisotti, G. Treglia, and A. Giordano, "Which is the optimal acquisition time for FDG PET/CT imaging in patients with infective endocarditis?," *Journal of Nuclear Cardiology*, vol. 20, no. 2, pp. 307–309, 2013.
- [52] G. Treglia, F. Maggi, L. Bonomo, and A. Giordano, "Usefulness of fluorine-18 fluorodeoxyglucose PET/computed tomography in diagnosis of aortitis and treatment response evaluation in a patient with aortic prosthesis," *Journal of Cardiovascular Medicine*, vol. 12, no. 11, pp. 814–816, 2011.
- [53] A. R. Larici, A. W. Glaudemans, A. Del Ciello, R. H. Slart, L. Calandriello, and O. Gheysens, "Radiological and nuclear medicine imaging of sarcoidosis," *Q J Nucl Med Mol Imaging*, vol. 62, no. 1, pp. 14–33, 2018.
- [54] G. Treglia, S. Annunziata, D. Sobic-Saranovic, F. Bertagna, C. Caldarella, and L. Giovannella, "The role of  $^{18}\text{F}$ -FDG-PET and PET/CT in patients with sarcoidosis," *Academic Radiology*, vol. 21, no. 5, pp. 675–684, 2014.
- [55] G. Treglia, S. Taralli, and A. Giordano, "Emerging role of whole-body  $^{18}\text{F}$ -fluorodeoxyglucose positron emission tomography as a marker of disease activity in patients with sarcoidosis: a systematic review," *Sarcoidosis Vasculitis and Diffuse Lung Diseases*, vol. 28, no. 2, pp. 87–94, 2011.
- [56] R. H. J. A. Slart, A. W. J. M. Glaudemans, P. Lancellotti et al., "A joint procedural position statement on imaging in cardiac sarcoidosis: from the cardiovascular and inflammation & infection committees of the European association of nuclear medicine, the European association of cardiovascular imaging, and the American society of nuclear cardiology," *Journal of Nuclear Cardiology*, vol. 25, no. 1, pp. 298–319, 2018.
- [57] A. W. Glaudemans, N. Prandini, M. Di Girolamo et al., "Hybrid imaging of musculoskeletal infections," *Quarterly Journal of Nuclear Medicine and Molecular Imaging*, vol. 62, no. 1, pp. 3–13, 2018.
- [58] G. Treglia, C. Focacci, C. Caldarella et al., "The role of nuclear medicine in the diagnosis of spondylodiscitis," *European Review for Medical and Pharmacological Sciences*, vol. 16, no. 2, pp. 20–25, 2012.
- [59] F. Jamar, A. Versari, F. Galli, F. Lecouvet, and A. Signore, "Molecular imaging of inflammatory arthritis and related disorders," *Seminars in Nuclear Medicine*, vol. 48, no. 3, pp. 277–290, 2018.
- [60] O. Catalano, F. Maccioni, C. Lauri, S. Auletta, R. Dierckx, and A. Signore, "Hybrid imaging in Crohn's disease: from SPECT/CT to PET/MR and new image interpretation criteria," *Quarterly Journal of Nuclear Medicine and Molecular Imaging*, vol. 62, no. 1, pp. 40–55, 2018.
- [61] R. Sadeghi and G. Treglia, "Systematic reviews and meta-analyses of diagnostic studies: a practical guideline," *Clinical and Translational Imaging*, vol. 5, no. 2, pp. 83–87, 2017.
- [62] M. B. Brøndserud, C. Pedersen, F. S. Rosenvinge, P. F. Høilund-Carlsen, and S. Hess, "Clinical value of FDG-PET/CT in bacteremia of unknown origin with catalase-negative gram-positive cocci or *Staphylococcus aureus*," *European Journal of Nuclear Medicine and Molecular Imaging*, vol. 46, no. 6, pp. 1351–1358, 2019.
- [63] J. Colombo, L. Elzi, G. Treglia, and A. Perren, "Light in the dark:  $^{18}\text{F}$ -FDG PET/CT in *Staphylococcus aureus* bacteremia of unknown origin," *Intensive Care Medicine*, vol. 44, no. 4, pp. 488–489, 2018.
- [64] D. Mandry, A. Tatopoulos, E. Chevalier-Mathias et al., " $^{18}\text{F}$ -fluorodeoxyglucose positron emission tomography combined with whole-body computed tomographic angiography in critically ill patients with suspected severe sepsis with no definite diagnosis," *European Journal of Nuclear Medicine and Molecular Imaging*, vol. 41, no. 10, pp. 1924–1930, 2014.
- [65] J.-R. Tseng, K.-Y. Chen, M.-H. Lee, C.-T. Huang, Y.-H. Wen, and T.-C. Yen, "Potential usefulness of FDG PET/CT in patients with sepsis of unknown origin," *PLoS One*, vol. 8, no. 6, Article ID e66132, 2013.
- [66] A. Tewari, S. Padma, and P. Sundaram, "The diagnostic role of  $^{18}\text{F}$ -fluorodeoxyglucose-positron emission tomography/computed tomography in occult bacteremia searching underlying primary disease," *Annals of Indian Academy of Neurology*, vol. 15, no. 4, pp. 336–338, 2012.
- [67] S. Kluge, S. Braune, A. Nierhaus et al., "Diagnostic value of positron emission tomography combined with computed tomography for evaluating patients with septic shock of unknown origin," *Journal of Critical Care*, vol. 27, no. 3, pp. 316.e1–7, 2012.
- [68] B. Leroy-Freschini, G. Treglia, X. Argemi et al., " $^{18}\text{F}$ -FDG PET/CT for invasive fungal infection in immunocompromised patients," *QJM: An International Journal of Medicine*, vol. 111, no. 9, pp. 613–622, 2018.
- [69] G. Treglia, S. Taralli, M. L. Calcagni, F. Maggi, A. Giordano, and L. Bonomo, "Is there a role for fluorine 18 fluorodeoxyglucose-positron emission tomography and positron emission tomography/computed tomography in evaluating patients with mycobacteriosis? a systematic review," *Journal of Computer Assisted Tomography*, vol. 35, no. 3, pp. 387–393, 2011.
- [70] I. J. Kouijzer, F. J. Vos, C. P. Bleeker-Rovers, and W. J. Oyen, "Clinical application of FDG-PET/CT in metastatic infections," *Quarterly Journal of Nuclear Medicine and Molecular Imaging*, vol. 61, no. 2, pp. 232–246, 2017.
- [71] H. Balink, S. S. Tan, N. J. G. M. Veeger et al., " $^{18}\text{F}$ -FDG PET/CT in inflammation of unknown origin: a cost-effectiveness pilot-study," *European Journal of Nuclear Medicine and Molecular Imaging*, vol. 42, no. 9, pp. 1408–1413, 2015.
- [72] E. M. Becerra Nakayo, A. M. Garcia Vicente, A. M. Soriano Castrejón et al., "Análisis de costo-efectividad en el diagnóstico de fiebre de origen desconocido y el papel de la  $^{18}\text{F}$ -FDG PET-TC: propuesta de algoritmo diagnóstico," *Revista Española de Medicina Nuclear e Imagen Molecular*, vol. 31, no. 4, pp. 178–186, 2012.
- [73] F. J. Vos, C. P. Bleeker-Rovers, B. J. Kullberg, E. M. M. Adang, and W. J. G. Oyen, "Cost-effectiveness of routine  $^{18}\text{F}$ -FDG PET/CT in high-risk patients with gram-positive bacteremia," *Journal of Nuclear Medicine*, vol. 52, no. 11, pp. 1673–1678, 2011.
- [74] T. Ebenhan, E. Lazzeri, and O. Gheysens, "Imaging of bacteria: is there any hope for the future based on past experience?," *Current Pharmaceutical Design*, vol. 24, no. 7, pp. 772–786, 2018.

- [75] S. Auletta, M. Varani, R. Horvat, F. Galli, A. Signore, and S. Hess, "PET radiopharmaceuticals for specific bacteria imaging: a systematic review," *Journal of Clinical Medicine*, vol. 8, no. 2, p. 197, 2019.
- [76] M. Meyer, N. Testart, M. Jreige et al., "Diagnostic performance of PET or PET/CT using  $^{18}\text{F}$ -FDG labeled white blood cells in infectious diseases: a systematic review and a bivariate meta-analysis," *Diagnostics*, vol. 9, no. 2, p. 60, 2019.
- [77] M. Pacilio, C. Lauri, D. Prosperi, A. Petitti, and A. Signore, "New SPECT and PET radiopharmaceuticals for imaging inflammatory diseases: a narrative review," *Seminars in Nuclear Medicine*, vol. 48, no. 3, pp. 261–276, 2018.
- [78] M. M. Sathekge, A. O. Ankrah, I. Lawal, and M. Vorster, "Monitoring response to therapy," *Seminars in Nuclear Medicine*, vol. 48, no. 2, pp. 166–181, 2018.
- [79] M. Sollini, R. Berchiolli, M. Kirienko et al., "PET/MRI in infection and inflammation," *Seminars in Nuclear Medicine*, vol. 48, no. 3, pp. 225–241, 2018.

## Review Article

# Neutrophil Elastase Activity Imaging: Recent Approaches in the Design and Applications of Activity-Based Probes and Substrate-Based Probes

Natacha Jugniot,<sup>1</sup> Pierre Voisin,<sup>1</sup> Abderrazzak Bentaher,<sup>3</sup> and Philippe Mellet <sup>1,2</sup>

<sup>1</sup>Centre de Résonance Magnétique des Systèmes Biologiques, UMR5536, CNRS, Université de Bordeaux, 33076 Bordeaux, France

<sup>2</sup>INSERM, 33076 Bordeaux Cedex, France

<sup>3</sup>Equipe "Inflammation et Immunité de l'Épithélium Respiratoire"—EA7426 Faculté de Médecine Lyon Sud, 69495 Pierre Bénite, France

Correspondence should be addressed to Philippe Mellet; [philippe.mellet@rmsb.u-bordeaux.fr](mailto:philippe.mellet@rmsb.u-bordeaux.fr)

Received 28 March 2019; Accepted 19 May 2019; Published 12 June 2019

Guest Editor: Xiang-Guo Li

Copyright © 2019 Natacha Jugniot et al. This is an open access article distributed under the Creative Commons Attribution License, which permits unrestricted use, distribution, and reproduction in any medium, provided the original work is properly cited.

The last few decades of protease research has confirmed that a number of important biological processes are strictly dependent on proteolysis. Neutrophil elastase (NE) is a critical protease in immune response and host defense mechanisms in both physiological and disease-associated conditions. Particularly, NE has been identified as a promising biomarker for early diagnosis of lung inflammation. Recent studies have shown an increasing interest in developing methods for NE activity imaging both in vitro and in vivo. Unlike anatomical imaging modalities, functional molecular imaging, including enzymatic activities, enables disease detection at a very early stage and thus constitutes a much more accurate approach. When combined with advanced imaging technologies, opportunities arise for measuring imbalanced proteolytic activities with unprecedented details. Such technologies consist in building the highest resolved and sensitive instruments as well as the most specific probes based either on peptide substrates or on covalent inhibitors. This review outlines strengths and weaknesses of these technologies and discuss their applications to investigate NE activity as biomarker of pulmonary inflammatory diseases by imaging.

## 1. Introduction

Degradome analysis indicates that protease and protease inhibitor genes represent more than 2% of total genes in human genome [1]. Proteases regulate a variety of physiological processes critical for life [2] including regulation of maturation, localization, activity and recycling of many proteins, modulation of protein-protein interactions, processing in signalization, transduction, and amplification of molecular signals. Proteases influence DNA replication and transcription, cell proliferation, migration, and differentiation, tissue remodeling, angiogenesis, wound repair, blood coagulation, digestion, ovulation, inflammation, necrosis, and apoptosis and immune response as well as pathogen clearance [3]. Accordingly, proteases are a major focus of attention for the pharmaceutical industry as potential drug

targets or as diagnostic and prognostic biomarkers [4]. Since the function of proteases is to cleave proteins and peptides in response to biological, chemical, or physical stimuli, their action must be carefully orchestrated and strictly controlled for homeostasis purpose. Therefore, their actions are regulated at multiple levels [5]. Proteases are traditionally synthesized as inactive enzymes called zymogens that require activation process. They consist in subunit multimerization. For instance, dimerization of the Human Immunodeficiency Virus type 1 (HIV-1) protease subunits is an essential process for the acquisition of proteolytic activity, which plays a critical role in the maturation and replication of the virus [6]. Another way of regulation consists in proteolytic cleavage of precursors, as pancreatic serine proteases, activated for food digestion only when they reach the duodenum [7]. Others mechanisms consist either in

blocking active proteases by endogenous inhibitors or in trapping them in a dedicated compartment such as mitochondria, specific apical membranes, and lysosomes, in which acidic pH participates also to enzyme activity containment. Particularly, mature protease neutrophil elastase (NE) is stored in specific neutrophilic granules in an active form that should be inactivated by inhibitors upon its extracellular release in the setting of inflammation or infection [8]. Therefore, if not correctly regulated, NE activity has the ability to damage host tissues leading to the development of pathologies as pointed below. Accordingly, noninvasive methods allowing direct and reliable monitoring of protease activity in the context of complex biological samples or in vivo especially in diseased situations are greatly needed for a diagnostic purpose. In this context, this review will focus on recent advances in NE activity detection, quantification, and applications both in vitro and in vivo.

*1.1. Neutrophil Elastase: A Double-Edged Sword.* NE (EC 3.4.21.37) is a 29 kDa serine protease of chymotrypsin family stored in azurophilic granules of polymorphonuclear neutrophils [9, 10] and released during neutrophil degranulation [11]. NE plays a relatively important role in neutrophil-mediated bacterial killing, and a cidal mechanism of the enzyme against Gram-negative bacteria has been elucidated [12, 13]. Furthermore, not only NE kills directly invading pathogens, but the enzyme fine tunes host inflammatory response for better pathogen eradication and its associated inflammation [14]. Normal inflammatory response triggers recruitment and activation of neutrophils toward the inflammation site. Neutrophil extracellular degranulation occurs and an overwhelming concentration of NE molecules over their endogenous inhibitors takes place. Protease activity is yet restricted in space and time by inhibitors in the tissue. Paradoxically, persistent or excessive inflammation as a result of prolonged exposure to stimulus has been found to be detrimental. NE with exacerbated elastolytic activity was shown to be one of the main lung destructive actors. Indeed, its large repertoire of substrates, particularly, elastin favors potent proteolysis [15]. NE activity can result in extensive lung tissue damages potentially leading to organ failure and death making inflammatory diseases a major health concern worldwide as well as an important economic burden [16]. Clinical studies have evidenced how an elevated concentration of NE correlates to acute lung injury [17], development of cystic fibrosis (CF) symptoms [18] as well as Chronic obstructive pulmonary disorders (stable and/or exacerbated COPD) [19], and bronchiectasis [20]. Moreover, it has been postulated that NE can contribute to the progress of lung cancer [21]. This correlation between NE activity level and disease progress has prompted researchers to investigate the use of NE as biomarker to diagnose and monitor pathological inflammations.

*1.2. Pivotal Role of NE/Anti-NE Balance Status Imaging.* A standard approach for looking at proteases in inflamed situations is the analysis of their transcript levels. Because

of the posttranslational modifications, monitoring protease activity directly is more reliable to translate its roles in biological events. Another commonly used method for the quantification of NE is the immunodiagnostic from biological fluid samples. Antibody-related techniques yield information on total protease amount but lack the ability to differentiate between active and inactive enzyme forms. Methods to overcome such limitations tried to combine classical ELISA with the application of active-site inhibitors. A colorimetric active site-specific immunoassay (CASSIA) was described [22] for several serine proteases with arginyl specificity. Preferred protocols consist in using avidin capture of a biotinylated peptidyl arginyl chloromethyl ketone (CMK) and a specific antiprotease antibody recognition revealed by an enzymatic amplification step. In the case of a chymotrypsin-like specificity, a peptidyl inhibitor with a hydrophobic P1 amino acid side-chain can be used. Based on the CASSIA technique, cathepsin G activity was successfully detected [23]. It is thus largely conceivable that analog probes can be developed for a neutrophil-like activity detection. Nevertheless, a difficulty lies in the inescapable capture competition between protease-coupled probes and the uncoupled probes. Thus, to make sure that the enzyme activity measurement is not underestimated, a more complex assay is needed. It can consist in a preliminary assay in which uncoupled probe would be removed or in an increase of coated avidin concentration. Another method, termed ABRA-ELISA (Activity-Based probe Ratiometric-Enzyme Linked ImmunoSorbent Assay), was found particularly relevant on serine protease kallikreins for ovarian cancer diagnosis and could be applied to NE [24]. This strategy consists in combining the high throughput and high sensitivity of an ELISA-based detection with the advantage of an active-site inhibitor labeling. The proportion of the active form relative to the total concentration of the enzymatic biomarker (regular ELISA) would then be easily monitored in samples and may therefore serve as a novel diagnostic tool to quantify the active form in pathophysiological settings. However, these assays have limitations as the requirement for enzyme immobilization on a solid surface can result in its improper structural orientation or decreased reactivity with the target. It also needs collection of biological samples, requiring therefore an invasive intervention. Thus, methods for in vivo monitoring and imaging of NE activity in real time are studied.

Clinical symptoms are often undetectable at early stage of a disease, making diagnosis approach even more challenging. Nowadays, no reliable clinical methods exist to image deleterious NE proteolytic activity, which is again convincingly documented as a culprit in tissue destructive diseases. To address this concern, the field of functional molecular imaging represents an attractive and relevant tool [25]. The information quality provided is highly dependent on (a) the choice of the biomarker, (b) the physical, biochemical and pharmacological characteristics of the probe, and (c) the imaging modality [26] to characterize NE imbalance activity, especially during disease initiation phase.

This review will discuss the design of novel probes and how their application in NE proteolytic activity imaging could become a reliable clinical diagnostic tool. On one hand, imaging agents binding their biological target with high specificity and affinity are worked out, including the design of substrate-based probes and activity-based probes. On the other hand, imaging instruments including optical imaging and Magnetic Resonance Imaging (MRI) methods should be able to detect disorders with high sensitivity and high resolution (Figure 1).

## 2. Molecular Technologies of NE Activity Imaging

The development of functional imaging technologies has led to the production of a myriad of molecular imaging agents for a variety of proteases [27–32]. Table 1 lists a series of probes specifically targeting NE activity and discussed in this review. Enzymatic constants, types of probe, and detection modality are indicated for each.

**2.1. Activity-Based Probes.** Activity-based probes (ABPs) are low-molecular-weight molecule reporters designed to covalently bind a target enzyme as an active site reacting inhibitor and allow to visualize and localize active protease using fluorescence-based imaging modalities. All ABPs share a similar basic design, which incorporates elements required for targeting, modification, and detection of target proteins (Figure 2). Features that characterize ABP structures include (i) a reactive functional group termed as « warhead » that binds the catalytic residue of the enzyme active site, thus leading to the formation of covalent complex; (ii) a linker chain that has the basic function to separate the reactive functional group from the tag (for NE targeting, the linker corresponds to specific peptides matching its substrate binding pocket); and (iii) a reporter tag, often a biotin or fluorophore for the optical detection of the enzyme-probe complex. It should be noted that some isotope-based techniques were studied. For example, a radiolabeled aptamer-based inhibitor of NE coupled to  $^{99m}\text{Tc}$  has been used to image inflammation in a rat reverse passive Arthus reaction model [33]. In the same way, a human NE inhibitor (EPI-HNE-2) radiolabeled with  $^{99m}\text{Tc}$  has been used to visualize inflammation and infection in monkeys [34]. However, while nuclear imaging can be very sensitive, ionizing radiations limit its use in routine disease follow-up. Then, optical detection constitutes a judicious alternative.

ABPs appear very interesting for living organisms imaging applications. Indeed, one of the advantages of ABPs relies in the fact that the selectivity can be controlled both by the warhead and linker sequence. In this aim, focus on warhead and linker is more suitable over reporter tag.

**2.1.1. Warhead.** Numerous peptide-based as well as non-peptidyl inhibitors have been studied for NE specific studies [48]. Peptide CMK, like the most effective one MeO-Suc-AAPV-CMK, has proved to be very effective inhibitors of NE

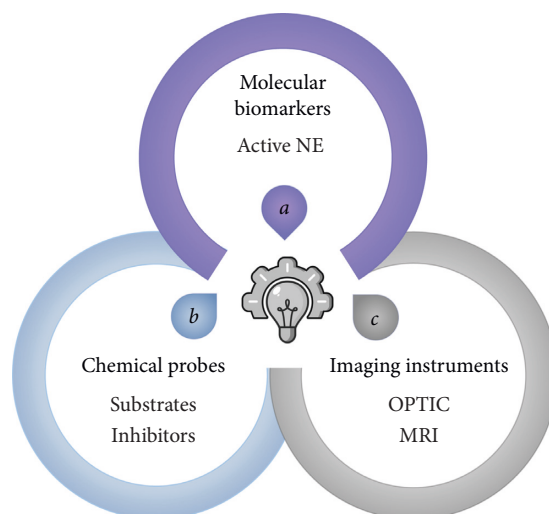


FIGURE 1: Key elements necessary for neutrophil elastase (NE) proteolytic imaging. The concept is to integrate molecular biomarker, chemical probes with imaging instruments to visualize, localize, and quantify NE activity for diagnosis (disease initiation and/or progression) and therapy follow-up of inflammatory processes. OPTIC: optical imaging; MRI: magnetic resonance imaging.

and particularly useful for structural studies [49, 50]. However, oligopeptides CMK are highly reactive and potentially toxic molecules, thus will never find a use in clinics [51]. They rather serve as a standard of comparison for developed inhibitors. ABPs have been proposed with a large repertoire of warhead designed to covalently link amino acid residue Ser195 of NE. Several groups reported interesting data about the influence of well-known classes of inhibitors used as warhead to study the biological functions of neutrophil serine proteases [52, 53]. Recently, Schulz-Fincke and colleagues highlighted the strong labeling capability of a sulfonyloxypthalimide moiety as a new type of warhead that is linker-connected to a coumarin fluorophore [54]. The probe showed adequate fluorescence properties and suitable detection of NE in the presence of a large excess of cell lysate proteins with no detectable nonspecific interaction. The use of this probe against endogenous elastase from healthy donors-derived blood show promising results for further in vivo experiments.

**2.1.2. Linker.** In addition to warhead development, recognition sequence of the linker adds to the probe specificity. This link controls the specificity of the inhibitor toward its target by a recognition element such as a peptidic sequence. The exploration of protease substrate specificity is generally restricted to naturally occurring amino acids, obviously limiting the degree of conformational space that can be surveyed. In their studies, Kasperkiewicz and coworkers reported the design of a hybrid natural and nonnatural peptidic substrate of NE, PK101, using a hybrid combinatorial substrate library profiling [35, 36]. That optimal substrate sequence exhibits astounding  $k_{\text{cat}}/K_M$  surpassing the commonly used peptide sequence AAPV by more than

TABLE 1: Recapitulative set of probes for NE proteolytic activity imaging.

Probe sequence	$k_{\text{cat}}/K_M$ ( $\text{M}^{-1}\text{s}^{-1}$ )	$K_M$ ( $\mu\text{M}$ )	$k_{\text{cat}}$ ( $\text{s}^{-1}$ )	Nature of probe	Detection modality	Probe name	References
$^{99\text{m}}\text{Tc-NX21909}$		$2 \times 10^5$ ( $k_{\text{inact}}$ )		Activity-based probe	Positron emission tomography	NX21909	[33]
$^{99\text{m}}\text{Tc-MAG}_3\text{-EPI-HNE-2}$		$2 \times 10^{-6}$ ( $K_i$ )		Activity-based probe	Positron emission tomography	EPI-HNE-2	[34]
Biotin-PEG(4)-Nle(O-bzl)-Met( $\text{O}_2$ )-Oic- AbuPO(Oph) <sub>2</sub>	$1.4 \times 10^7$ ( $k_{\text{obs}}/I$ )	n.d	n.d	Activity-based probe	Optic (fluorogenic)	Elastase-PK101	[35, 36]
Ac-AAPV-AMC	$5.8 \times 10^3$	n.d	n.d	Substrate-based probe	Optic (fluorogenic)	—	[37]
MeO-Suc-AAPV-AMC	$11 \times 10^3$	290	3.3	Substrate-based probe	Optic (fluorogenic)	—	[37]
CFP-TSGGSGGTRQFIRWGGGGGGTIG- YFP-HHHHHH	$390 \times 10^5$ ( $k_{\text{obs}}/K_M$ )	$0.7 \pm 0.2$	$27 \pm 5.4$ ( $k_{\text{obs}}$ )	Substrate-based probe	Optic (fluorogenic)	Protein Biosensor IV	[38]
Abz-QPMAVVQYPQ-EDDnp	$10.9 \times 10^5$	n.d	n.d	Substrate-based probe	Optic (fluorogenic)	NEmo-1 & NEmo-2	[39, 40]
CNC-(O-C(O)G-NHC(O)-Suc-APA-AMC	$33.5 \times 10^5$	n.d	n.d	Substrate-based probe	Optic (fluorogenic)	Neutrophil Elastase 680 FAST <sup>sm</sup>	[41–45]
MeO-Suc-AAPV-(R/S) $\text{C}_{12}\text{H}_{23}\text{NO}_3\text{P}^{\bullet}$				Substrate-based probe	Optic (fluorogenic) MRI (dynamic nuclear polarization)	PepNA	[46]
R-isomer	$9.3 \times 10^5$	$15 \pm 2.9$	$14 \pm 0.9$			—	[47]
S-isomer	$6.4 \times 10^5$	$25 \pm 5.4$	$16 \pm 1.1$			—	

n.d., no data.

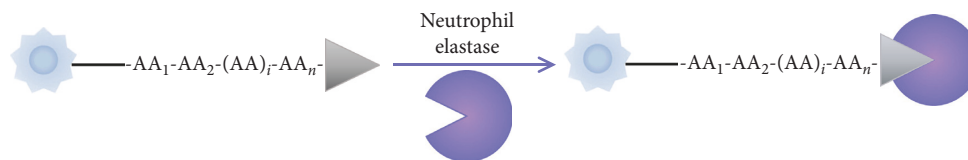


FIGURE 2: Overall principle of activity-based probe (ABP). Warhead (grey triangle) structurally matches with the target protease (purple). Active ABP can be detected by the tag (blue star).  $AA_1-AA_n$  indicates amino acid position in the specific peptide.

7000-fold and showed high selectivity (900-fold) to NE over the closely related protease Proteinase 3 (PR3). The substrate was converted in an extremely sensitive ABP and was applied to reveal NE activity in vitro during the process of neutrophil extracellular trap (NET) formation [35].

Although the development of selective ABP probes remains a challenge, we believe that incorporation of novel warheads mixed with original substrate design will enable a very specific targeting of biomarkers as NE. Nevertheless, by nature, ABPs bind only a single protease and generate only one detectable molecule per binding event. The detected signal is then directly proportional to the overall concentration of active protease, and detection of low-abundance proteins may be challenging.

**2.2. Substrate-Based Probes.** Signal amplification by multiple processing events can be successfully achieved by substrate-based probes. Indeed, one of the major benefits of using the turnover of substrate as a reporter is that a single active protease can process many substrates continuously leading thereby to signal amplification [55]. Below, we emphasize on the use of attractive substrate-based probes to NE activity monitoring.

**2.2.1. Substrate-Based Probes for Optical Imaging.** Molecular imaging requires high-resolution and highly sensitive instruments to detect imaging agents that connect the imaging signal with the molecular event. Molecular imaging is easily performed using fluorescent probes enabling 3D images on small animals. A variety of organic fluorophores with emission wavelengths ranging from visible to near infrared region have been synthesized. These molecules can be modified with additional groups to optimize their inherent properties such as photophysical characteristics, solubility, cell permeability, toxicity, or enzyme specificity. Currently, three major types of activated fluorescent probes are used to monitor NE activity (Figure 3). The general approach is to design a substrate so that the prequench signal of the fluorophore can be turned « on » by protease activity.

**(1) FL/UV Enzyme-Sensitive Probe.** The fluorogenic/chromogenic probe design consists of a peptide attached at the C-terminus to a revelator, such as Amino-Methyl Coumarin (AMC, in vitro and in vivo fluorophore) or p-Nitro-Anilide (pNA, in vitro chromophore) (Figure 3(a)). Those probes are limited to a strong P1 interaction with two or three additional sites according to Schechter & Berger nomenclature [56]. Bieth and coworkers thoroughly studied the action

of NE on substrates coupled to those two molecules varying in their peptidic chain length [57, 58]. Few years later, the group of powers developed a sensitive assay for NE activity inhibition involving the exploitation of the peptide sequence MeO-Suc-Ala-Ala-Pro-Val-CH<sub>2</sub>Cl, which has been reported as the most effective CMK inhibitor of NE [49]. Taking advantage of this sequence, they attached an AMC molecule to the C-terminal carboxyl group of the peptide sequence [59] (MeO-Suc-Ala-Ala-Pro-Val-AMC). The same year, MeOSuc-Ala-Ala-Pro-Val-pNA substrates were synthesized and analytically used as chromogenic substrate [37]. Currently, several synthetic NE substrates are commercially available. However, for routine assays, NE activity is measured using either fluorogenic peptide substrates such as *N*-methoxy-succinyl-Ala-Ala-Pro-Val-AMC or chromogenic peptide substrates such as *N*-methoxy-succinyl-Ala-Ala-Pro-Val-pNA. These are widely used to quantify NE and as a marker in inflammatory lung diseases, such as CF [60, 61].

**(2) Fluorophore-Quencher Type Probe.** Initially developed for caspase activity detection, many strategies use quenched fluorogenic substrates in accordance with the principle of Förster resonance energy transfer (FRET) [62]. FRET-based probe requires a pair of fluorophores, individually flanked at one each side of a peptide taking advantage of both the *P* and *P'* specificity. In order for energy transfer to occur, the emission spectrum of the donor has to overlap with the excitation spectrum of the acceptor and both have to be located within a short distance from each other ( $<R_0$ , i.e., Förster distance at which the energy transfer efficiency is 50%). Cleavage of the linker drives away the two fluorochromes suppressing the energy transfer and resulting in an increase in the emission intensity of the donor and reducing or eliminating the acceptor emission (Figure 3(b)).

Potential utilization of FRET-based probes to monitor protease activity has been investigated in 2004 by Felber and colleagues [63]. They exposed an FRET system consisting of Cyan and Yellow fluorescent proteins (CFP and YFP, respectively) linked by a peptide. CFP-linker-YFP system was used for a variety of proteases. Based on Felber biosensor, Schulenburg et al. published a powerful FRET-based probe in 2016 [64]. They applied the CFP-linker-YFP system for NE with a linker containing a NE-recognition sequence. This probe exhibits about 200-fold more affinity than the chromogenic substrate reference (MeO-Succinyl-AAPV-pNA).

Other strategy consists in quenched FRET probes with improved specificity toward human and mouse neutrophil elastase, with the substrate sequence PMAVVQSV [38].

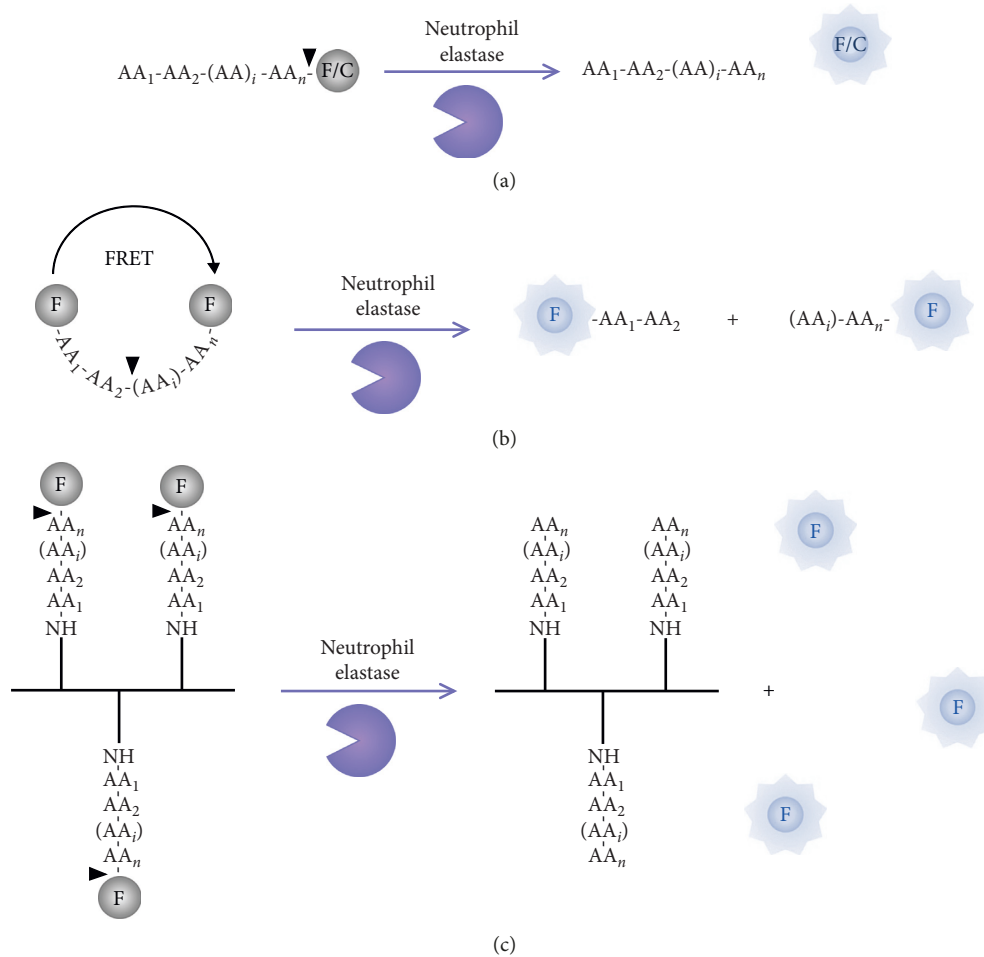


FIGURE 3: Protease-sensitive probes for optical imaging. (a) Fluorogenic (F)/chromogenic (C) enzyme-sensitive probe. One fluorescent or chromogenic molecule is bound to a peptide. Spectroscopic properties will be altered upon proteolysis. (b) Fluorophore-quencher type probe. Förster resonance energy transfer- (FRET-) based probes require a donor and an acceptor fluorophore pair each saturated on one side of the enzyme cleavage site. (c) Polymeric-peptide conjugate probe. Overabundance of fluorophores coupled to a polymer backbone via a peptide substrate. Black arrowheads depict cleavage site within the amino acid sequence.

The linker sequence in the construct is designed to be preferentially cleaved by NE while remaining resistant to other proteases including mouse PR3 [39]. The company PerkinElmer took advantage of this sequence to provide Neutrophil Elastase 680 FAST™ as a preclinical fluorescent activated sensor. It consists of the dedicated peptide sequence with two VivoTag-S680 fluorochromes, which are self-quenched and become highly fluorescent after cleavage by elastase. In 2011, Kossodo et al. used this substrate to image and quantify for the first time NE activity in mouse models with acute lung injury and response to treatments [65]. Neutrophil Elastase 680 FAST™ is now used widely as NE substrate and largely reported in the literature not only in lung inflammation but also in cancers [41, 66], arthritis [42, 43], and atherosclerosis [44].

So far, studies of NE activity have focused on free NE form. Interestingly, several reports demonstrated [9, 45, 67–69] and measured [67] the presence of a significant proportion of NE binding the anionic external plasma membrane of cells in an active form. Membrane-associated

NE appears to be important in lung pathogenesis [70] and measuring its activity *in vivo* may be of great help in testing the activity of exogenous inhibitors since it was shown to be largely resistant to inhibition by endogenous inhibitors including  $\alpha 1$ -antitrypsin and SLPI [45]. Particularly, the activity of membrane-associated NE pool may be relevant in early CF in young children for which no free NE activity is detectable in Bronchoalveolar Lavages (BALs) fluid despite structural evidence of lung disease by chest CT [71, 72]. Using the substrate sequence previously described, PMAVVSVP [38], Schultz and coworkers generated FRET reporters for free NE (NEmo-1) as well as the lapidated form for plasma membrane insertion (NEmo-2) where two negative charges were introduced to prevent internalization into the cell [73]. For the first time, the role of membrane-associated NE activity was shown to correlate, *ex vivo*, with severity of lung disease in patients with CF and potentially other chronic neutrophilic lung diseases [18]. Interestingly, their results suggest that, in the microenvironment of CF airways, neutrophils acquire this activated configuration with increased membrane-

associated NE activity even at low levels of inflammation, when free NE activity is still contained by endogenous antiproteases. Longitudinal studies in larger patient cohorts will be required to determine the predictive value of membrane-associated NE activity as a biomarker of disease severity and progression.

(3) *Polymeric-Peptide Conjugate Probe*. Alternatively, several studies used polymers modified with small organic fluorophores for proteolytic activity. Probes are developed utilizing a synthetic (i.e., dendrimer or polylysine) or protein (collagen, gelatin) [40] backbone to which a large number of reporters are attached via peptide linkers in close proximity to each other. Overabundance of fluorochromes anchored onto a polymer template through cleavable peptide substrate sequences in close proximity causes self-quenching. Upon peptide hydrolysis by proteases, fluorescence is restored and can be measured (Figure 1(c)).

A widely used series of probes is based on poly-L-lysine as a scaffold for conjugation of near-infrared fluorophores. Originally, Weissleder and colleagues first developed in 1999, a copolymer of poly-L-lysine and methoxypolyethylene glycol succinate (mPEGs) conjugated with cyanine dye (Cy5.5) for in vivo imaging [74]. Once internalized into cancer cells, 95% of the quenched fluorescence was recovered, resulting in a 12-fold increase in the fluorescent signal. Introduction of a selective peptide substrates between the polylysine backbone and the fluorophore allowed imaging of specific protease activities. By simply by replacing the peptides, imaging probes were then developed for detecting other disease-associated proteases such as cathepsins [75], MMPs [76, 77], caspases [78, 79], thrombin [80], or urokinase-type plasminogen activator [81, 82].

In 2005, Edwards and coworkers outlined an approach involving the use of cotton cellulose nanocrystal (CNC) fluorescent peptide conjugates as a support for a sensitive biosensor for NE and porcine pancreatic elastase (CNC-(O-C(O)Gly-NHC(O))succinyl-Ala-Pro-Ala-AMC) [83]. Relative to that shown by the tripeptide, peptide-CNC displayed 5-fold higher efficiency for NE as judged by a  $k_{cat}/K_M$  value of  $33\,500\text{ M}^{-1}\cdot\text{s}^{-1}$ .

There are however several drawbacks of using optical imaging: (a) substrate fluorescence quenching is not complete hence requiring long waiting times to eliminate nonspecific “blinding” light, (b) light tissue penetration is limited and prevents imaging of deeply seated tissues or skull, and (c) three-dimensional images are obtained by reconstruction.

**2.2.2. Substrate-Based Probes for Magnetic Resonance Imaging (MRI).** MRI appears particularly well suited to deliver exquisite anatomical details. It has a superior true 3D coding along with exceptionally good soft tissue contrast compared to optical imaging. MRI offers high spatial resolution and an unlimited depth penetration. Completely noninvasive, it allows simultaneous acquisition of anatomical structure and physiological function, particularly relevant for longitudinal follow-up involving multiple acquisitions. Nevertheless, the use of MRI is hampered by the limited sensitivity so far prevented clinical molecular imaging such as enzyme activity

imaging. Thus, it requires the design of smart contrast agents and development of powerful signal amplification strategies.

(1) *Overhauser-Enhanced Magnetic Resonance Imaging (OMRI)*. To overcome this limitation, a particular imaging method based on Overhauser effect was developed to enhance NMR sensitivity by increasing the signal/noise ratio [46]. Briefly, OMRI is a double-resonance experiment transferring a part of the higher spin polarization of an unpaired electron to the enviroing water protons (through electron-proton Overhauser effect) which enhances the MRI signal that appears brighter on the final image. This method, called Overhauser-Enhanced Magnetic Resonance Imaging (OMRI), was improved to localize and image molecular processes. NMR signal enhancement was observed in mouse glioma thanks to intravenous injection of an original nonspecific spin probe design [84]. Probes with unpaired electron such as nitroxide molecules are stable enough in physiological conditions to be detected by OMRI, and they can be turned into enzyme activity probes. In 2014, for the first time, 3D visualization of proteolytic activities happened in vivo in mice using an on/off nitroxide-labeled with a 30 kDa elastin substrate probe [85]. High Overhauser enhancements of 10-fold were observed in the intestinal tract of mice after elastolytic activity on the probe.

After such proof-of-concept, a  $\beta$ -phosphorylated nitroxide-based probe was developed and turned into NE specific probe by adding a peptide moiety, MeO-Suc-AAPV, recognized by the target enzyme. The probe presented a  $K_M$  of  $15\text{ }\mu\text{M}$  and a  $k_{cat}/K_M$  value of  $930\,000\text{ M}^{-1}\cdot\text{s}^{-1}$  [86]. It was designed such that its spectroscopic properties change upon removal of the peptide moiety by NE. This particular 6-peaks nitroxide has its resonant frequency shifted upon NE action (i.e, a change in its hyperfine coupling constants). It was tested in vitro by Electronic Paramagnetic Resonance (EPR). An unambiguous shift of about 5 G in the phosphorus hyperfine coupling constant was reached, allowing a specific detection of the substrate and the product at two distinct frequencies. Being a frequency-specific imaging method, the advantage of having a shifting resonance is that both the substrate and the product are detectable and distinguishable through OMRI. This shift can be used to measure an enzyme activity by EPR in vitro or to create contrast in vivo by Overhauser-enhanced magnetic resonance imaging (Figure 4). A concentration as low as 1 nM of NE was detected in mouse BALs from a lung acute inflammation model. In humans with cystic fibrosis, concentrations of NE in the epithelial lining fluid are around 2000, the lower limit of the method even for patients with mild lung disease [47, 87]. Thus, it ensures a fast and strong signal in a few seconds in vivo.

### 3. Summary and Outlook

The rapid expansion of molecular imaging technologies highlights promising prospects for early diagnosis of proteolysis. Substrate-based imaging agents have been recently shown to have strong values for NE imaging as biomarker of

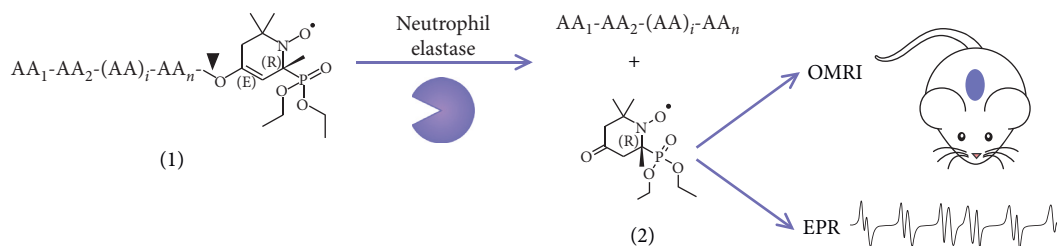


FIGURE 4: Proteolysis imaging by MRI. Proteolysis of peptide-locked nitroxide (1) into a free nitroxide (2) by neutrophil elastase creating high contrast in vivo by OMRI and EPR shift in vitro. Black arrowhead designates cleavage site in the amino acid specific sequence.

inflammation. Significantly, strategies using substrate coupled to an original nitroxide in OMRI exhibit multiple advantages. Totally noninvasive, OMRI values are highly resolved and highly sensitive. Recently, another type of nitroxide was used as theranostic approach for the treatment of solid tumors. This smart agent named “Alkoxynamine” can, in vitro, spontaneously undergo hemolysis producing a highly reactive alkyl agent which in turn would induce cancer cell death and a stable nitroxide which would serve as imaging contrast agent by OMRI [88]. NE activity imaging could potentially take advantage of the enhancement of other MRI methods. Chemical exchange saturation transfer (CEST) agent as well as fluorine magnetic resonance spectrometry have been designed to detect the catalytic activity of several proteases, respectively [89–94].

Application to human diagnosis will require further development in terms of specificity and localization. Unnatural amino acid-recognition sequences could overcome such concerns by enhancing the specificity of proteolysis. On the other hand, ABPs, as covalently linked to the target protease (NE), lead to a prolonged retention at the inflamed site. This property contrasts with the irremediable diffusion of substrate-based probe.

Hence, the use of NE probes may ultimately lead to an easy methodology consisting in new diagnostic tools functioning through noninvasive protocols [95] for NE activity quantification in lung disorders especially those where this protease is regarded as the primary suspect [8]. The selectivity for other overexpressed proteases during pathologies, such as the matrix metalloproteinase MMP-2 and MMP-9, the cysteine protease cathepsin B in solid tumors, or cathepsin G, and PR3 in inflammation, opens the door for a sensitive imaging method of any protease/inhibitor imbalance.

In addition to clinical diagnosis, evaluation of disease severity and follow-up, NE molecular imaging would also certainly have a huge potential in drug development improvement [96]. Molecular imaging techniques can be used to assess drug efficacy in a more objective way than clinical outcomes. A better control of NE activity using safe and efficient inhibitors might help to downregulate proteolytic destruction and slow disease progression. AZD9668 has already shown an attractive potential in phase II study as reversible inhibitor of human NE [97]. Very recently, BAY 85-8501 was revealed as another reversible human NE inhibitor in phase II study [98].

Although overall the molecular imaging is still at stage of development, it is expected that more advancements will be achieved in the area of molecular imaging agent, and in near future, molecular imaging techniques should drive clinical transformations. By building a complete inventory of endangered areas, proteolysis imaging would allow to respond actively in a way that leads to the optimum outcome for the patient when organs can still be preserved [99]. Molecular imaging will open a novel avenue for clinicians and simultaneously support the goal of advancing personalized medicine: “*the right prevention and treatment for the right patient at the right time*” [100].

## Abbreviations

ABP:	Activity-based probe
AMC:	7-Amino-4-methylcoumarin
BAL:	Bronchoalveolar lavage
CEST:	Chemical exchange saturation transfer
CF:	Cystic fibrosis
CFP:	Cyan fluorescent protein
CMK:	Chloromethyl ketone
CNC:	Cellulose nanocrystal
COPD:	Chronic obstructive pulmonary disorder
EC:	Enzyme commission
EPR:	Electronic paramagnetic resonance
FRET:	Förster resonance energy transfer
MRI:	Magnetic resonance imaging
NE:	Neutrophil elastase
NET:	Neutrophil extracellular trap
OMRI:	Overhauser-enhanced magnetic resonance imaging
PepNA:	Peptide-nanocellulose aerogel
pNA:	<i>para</i> -Nitro-anilide
PR3:	Proteinase 3
Ser195:	Serine 195
YFP:	Yellow fluorescent protein.

## Additional Points

**Highlights.** (1) No robust method exists in clinic to image active Neutrophil elastase, well known to be a biomarker of inflammation. (2) Neutrophil elastase activity imaging can be reached in vitro and in vivo using probes based either on

peptide substrates or on covalent inhibitors. (3) The various probes and instrumentations for Neutrophil elastase activity imaging have distinct advantages and could be best used complementarily. (4) Improvements of probe structures and imaging instrumentation should be applied to further improve probes biodistribution and specificity. (5) Recent advances in molecular imaging open the door for a new clinical tool to image any protease/inhibitor imbalance.

## Conflicts of Interest

The authors declare that they have no conflicts of interest.

## Acknowledgments

This work was supported by the French ANR PULMO-ZYMAGE (ANR-15-CE18-0012-01).

## References

- [1] X. S. Puente, L. M. Sánchez, A. Gutiérrez-Fernández, G. Velasco, and C. López-Otín, "A genomic view of the complexity of mammalian proteolytic systems," *Biochemical Society Transactions*, vol. 33, no. 2, pp. 331–334, 2005.
- [2] N. Rawlings and G. Salvesen, *Handbook of Proteolytic Enzymes*, Academic Press, Waltham, MA, USA, 3rd edition, 2012.
- [3] A. W. Segal, "How neutrophils kill microbes," *Annual Review of Immunology*, vol. 23, no. 1, pp. 197–223, 2005.
- [4] B. Turk, "Targeting proteases: successes, failures and future prospects," *Nature Reviews Drug Discovery*, vol. 5, no. 9, pp. 785–799, 2006.
- [5] L. Hedstrom, "Serine protease mechanism and specificity," *Chemical Reviews*, vol. 102, no. 12, pp. 4501–4524, 2002.
- [6] A. Wlodawer, M. Miller, M. Jaskolski et al., "Conserved folding in retroviral proteases: crystal structure of a synthetic HIV-1 protease," *Science*, vol. 245, no. 4918, pp. 616–621, 1989.
- [7] H. Neurath and K. A. Walsh, "Role of proteolytic enzymes in biological regulation (a review)," *Proceedings of the National Academy of Sciences*, vol. 73, no. 11, pp. 3825–3832, 1976.
- [8] B. Korkmaz, M. S. Horwitz, D. E. Jenne, and F. Gauthier, "Neutrophil elastase, proteinase 3, and cathepsin G as therapeutic targets in human diseases," *Pharmacological Reviews*, vol. 62, no. 4, pp. 726–759, 2010.
- [9] C. T. N. Pham, "Neutrophil serine proteases: specific regulators of inflammation," *Nature Reviews Immunology*, vol. 6, no. 7, pp. 541–550, 2006.
- [10] B. Korkmaz, T. Moreau, and F. Gauthier, "Neutrophil elastase, proteinase 3 and cathepsin G: physicochemical properties, activity and physiopathological functions," *Biochimie*, vol. 90, no. 2, pp. 227–242, 2008.
- [11] M. Faurischou and N. Borregaard, "Neutrophil granules and secretory vesicles in inflammation," *Microbes and Infection*, vol. 5, no. 14, pp. 1317–1327, 2003.
- [12] A. Belaouaj, R. McCarthy, M. Baumann et al., "Mice lacking neutrophil elastase reveal impaired host defense against gram negative bacterial sepsis," *Nature Medicine*, vol. 4, no. 5, pp. 615–618, 1998.
- [13] A. A. Belaouaj, "Degradation of outer membrane protein a in *Escherichia coli* killing by neutrophil elastase," *Science*, vol. 289, no. 5482, pp. 1185–1187, 2000.
- [14] Y. S. Lopez-Boado, M. Espinola, S. Bahr, and A. Belaouaj, "Neutrophil serine proteinases cleave bacterial flagellin, abrogating its host response-inducing activity," *Journal of Immunology*, vol. 172, no. 1, pp. 509–515, 2004.
- [15] N. Guyot, J. Wartelle, L. Malleret et al., "Unopposed cathepsin G, neutrophil elastase, and proteinase 3 cause severe lung damage and emphysema," *American Journal of Pathology*, vol. 184, no. 8, pp. 2197–2210, 2014.
- [16] J. B. Soriano, A. A. Abajobir, K. H. Abate et al., "Global, regional, and national deaths, prevalence, disability-adjusted life years, and years lived with disability for chronic obstructive pulmonary disease and asthma, 1990–2015: a systematic analysis for the Global Burden of Disease Study 2015," *The Lancet Respiratory Medicine*, vol. 5, no. 9, pp. 691–706, 2017.
- [17] K. Kawabata, T. Hagio, and S. Matsuoka, "The role of neutrophil elastase in acute lung injury," *European Journal of Pharmacology*, vol. 451, no. 1, pp. 1–10, 2002.
- [18] A. S. Dittrich, I. Kühbandner, S. Gehrig et al., "Elastase activity on sputum neutrophils correlates with severity of lung disease in cystic fibrosis," *European Respiratory Journal*, vol. 51, no. 3, article 1701910, 2018.
- [19] R. Pawar and S. Abhang, "Evaluation of serum level of neutrophil elastase, superoxide dismutase and nitric oxide in COPD patients and its correlation with lung function test," *International Journal of Biochemistry Research & Review*, vol. 5, no. 2, pp. 153–161, 2015.
- [20] J. D. Chalmers, K. L. Moffitt, G. Suarez-Cuartin et al., "Neutrophil elastase activity is associated with exacerbations and lung function decline in bronchiectasis," *American Journal of Respiratory and Critical Care Medicine*, vol. 195, no. 10, pp. 1384–1393, 2017.
- [21] G. Moroy, A. J. P. Alix, J. Sapi, W. Hornebeck, and E. Bourguet, "Neutrophil elastase as a target in lung cancer," *Anti-Cancer Agents in Medicinal Chemistry*, vol. 12, no. 6, pp. 565–579, 2012.
- [22] K. G. Mann, E. B. Williams, S. Krishnaswamy, W. Church, A. Giles, and R. P. Tracy, "Active site-specific immunoassays," *Blood*, vol. 76, no. 4, pp. 755–766, 1990.
- [23] F. Zou, M. Schmon, M. Sienczyk et al., "Application of a novel highly sensitive activity-based probe for detection of cathepsin G," *Analytical Biochemistry*, vol. 421, no. 2, pp. 667–672, 2012.
- [24] K. Oikonomopoulou, K. K. Hansen, A. Baruch, M. D. Hollenberg, and E. P. Diamandis, "Immuno-fluorometric activity-based probe analysis of active KLK6 in biological fluids," *Biological Chemistry*, vol. 389, 2008.
- [25] R. Yan and D. Ye, "Molecular imaging of enzyme activity in vivo using activatable probes," *Science Bulletin*, vol. 61, no. 21, pp. 1672–1679, 2016.
- [26] M. L. James and S. S. Gambhir, "A molecular imaging primer: modalities, imaging agents, and applications," *Physiological Reviews*, vol. 92, no. 2, pp. 897–965, 2012.
- [27] W. Rut, M. Poręba, P. Kasperkiewicz, S. J. Snipas, and M. Drąg, "Selective substrates and activity-based probes for imaging of the human constitutive 20S proteasome in cells and blood samples," *Journal of Medicinal Chemistry*, vol. 61, no. 12, pp. 5222–5234, 2018.
- [28] M. Poreba, W. Rut, M. Vizovisek et al., "Selective imaging of cathepsin L in breast cancer by fluorescent activity-based probes," *Chemical Science*, vol. 9, no. 8, pp. 2113–2129, 2018.

- [29] Y. Shaulov-Rotem, E. Merquiol, T. Weiss-Sadan et al., "A novel quenched fluorescent activity-based probe reveals caspase-3 activity in the endoplasmic reticulum during apoptosis," *Chemical Science*, vol. 7, no. 2, pp. 1322–1337, 2016.
- [30] I. Abd-Elrahman, H. Kosuge, T. W. Sada et al., "Cathepsin activity-based probes and inhibitor for preclinical atherosclerosis imaging and macrophage depletion," *PLoS One*, vol. 11, Article ID e0160522, 2016.
- [31] B. F. Gilmore, D. J. Quinn, T. Duff, G. R. Cathcart, C. J. Scott, and B. Walker, "Expedited solid-phase synthesis of fluorescently labeled and biotinylated aminoalkane diphenyl phosphonate affinity probes for chymotrypsin- and elastase-like serine proteases," *Bioconjugate Chemistry*, vol. 20, no. 11, pp. 2098–2105, 2009.
- [32] M. J. Page, A. L. Lourenço, T. David et al., "Non-invasive imaging and cellular tracking of pulmonary emboli by near-infrared fluorescence and positron-emission tomography," *Nature Communications*, vol. 11, no. 6, 2015.
- [33] J. Charlton, J. Sennello, and D. Smith, "In vivo imaging of inflammation using an aptamer inhibitor of human neutrophil elastase," *Chemistry & Biology*, vol. 4, no. 11, pp. 809–816, 1997.
- [34] M. Rusckowski, T. Qu, J. Pullman et al., "Inflammation and infection imaging with a 99m TC-neutrophil elastase inhibitor in monkeys," *Journal of Nuclear Medicine*, vol. 41, no. 2, pp. 363–374, 2000.
- [35] P. Kasperkiewicz, M. Poreba, S. J. Snipas et al., "Design of ultrasensitive probes for human neutrophil elastase through hybrid combinatorial substrate library profiling," *Proceedings of the National Academy of Sciences*, vol. 111, no. 7, pp. 2518–2523, 2014.
- [36] B. C. Lechtenberg, P. Kasperkiewicz, H. Robinson, M. Drag, and S. J. Riedl, "The elastase-PK101 structure: mechanism of an ultrasensitive activity-based probe revealed," *ACS Chemical Biology*, vol. 10, no. 4, pp. 945–951, 2015.
- [37] K. Nakajima, J. C. Powers, B. M. Ashe, and M. Zimmerman, "Sensitive mapping the extended substrate binding site of cathepsin G and human leukocyte elastase," *Journal of Biological Chemistry*, vol. 254, no. 10, pp. 4027–4032, 1979.
- [38] T. Kalupov, M. Brillard-Bourdet, S. Dadé et al., "Structural characterization of mouse neutrophil serine proteases and identification of their substrate specificities," *Journal of Biological Chemistry*, vol. 284, no. 49, pp. 34084–34091, 2009.
- [39] H. Crisford, E. Sapey, and R. A. Stockley, "Proteinase 3; a potential target in chronic obstructive pulmonary disease and other chronic inflammatory diseases," *Respiratory Research*, vol. 19, no. 1, 2018.
- [40] O. R. F. Mook, C. V. Overbeek, E. G. Ackema, F. V. Maldegem, and W. M. Frederiks, "In situ localization of gelatinolytic activity in the extracellular matrix of metastases of colon cancer in rat liver using quenched fluorogenic DQ-gelatin," *Journal of Histochemistry & Cytochemistry*, vol. 51, no. 6, pp. 821–829, 2003.
- [41] I. Lerman, M. D. L. L. Hernandez, J. Rangel-Moreno et al., "Infiltrating myeloid cells exert protumorigenic actions via neutrophil elastase," *Molecular Cancer Research*, vol. 15, no. 9, pp. 1138–1152, 2017.
- [42] H. E. Scales, M. Ierna, K. M. Smith et al., "Assessment of murine collagen-induced arthritis by longitudinal non-invasive duplexed molecular optical imaging," *Rheumatology*, vol. 55, no. 3, pp. 564–572, 2015.
- [43] M. M. Muley, A. R. Reid, B. Botz, K. Bölskei, Z. Helyes, and J. J. McDougall, "Neutrophil elastase induces inflammation and pain in mouse knee joints via activation of proteinase-activated receptor-2," *British Journal of Pharmacology*, vol. 173, no. 4, pp. 766–777, 2016.
- [44] A. Glinzer, X. Ma, J. Prakash et al., "Targeting elastase for molecular imaging of early atherosclerotic lesions," *Arteriosclerosis, Thrombosis, and Vascular Biology*, vol. 37, no. 3, pp. 525–533, 2016.
- [45] C. A. Owen, "Cell surface-bound elastase and cathepsin G on human neutrophils: a novel, non-oxidative mechanism by which neutrophils focus and preserve catalytic activity of serine proteinases," *Journal of Cell Biology*, vol. 131, no. 3, pp. 775–789, 1995.
- [46] P. Mellet, P. Massot, G. Madelin et al., "New concepts in molecular imaging: non-invasive MRI spotting of proteolysis using an overhauser effect switch," *PLoS One*, vol. 4, no. 4, Article ID e5244, 2009.
- [47] S. I. Rennard, G. Basset, D. Lecossier et al., "Estimation of volume of epithelial lining fluid recovered by lavage using urea as marker of dilution," *Journal of Applied Physiology*, vol. 60, no. 2, pp. 532–538, 1986.
- [48] P. D. Edwards, D. W. Andisik, A. M. Strimpler, B. Gomes, and P. A. Tuthill, "Nonpeptidic inhibitors of human neutrophil elastase. 7. Design, synthesis, and in vitro activity of a series of pyridopyrimidine trifluoromethyl ketones," *Journal of Medicinal Chemistry*, vol. 39, no. 5, pp. 1112–1124, 1996.
- [49] J. C. Powers, B. F. Gupton, A. D. Harley, N. Nishino, and R. J. Whitley, "Specificity of porcine pancreatic elastase, human leukocyte elastase and cathepsin G inhibition with peptide chloromethyl ketones," *Biochimica et Biophysica Acta (BBA)—Enzymology*, vol. 485, no. 1, pp. 156–166, 1977.
- [50] P. Tuhy and J. C. Powers, "Inhibition of human leukocyte elastase by peptide chloromethyl ketones," *FEBS Letters*, vol. 50, no. 3, pp. 359–361, 1975.
- [51] V. Ranga, J. Kleinerman, M. P. C. Ip, J. Sorensen, and J. C. Powers, "Effects of oligopeptide chloromethyl ketone administered after elastase: renal toxicity and lack of experimental emphysema," *American Review of Respiratory Disease Returns*, vol. 124, pp. 613–618, 1981.
- [52] R. Grzywa, E. Burchacka, M. Łęcka et al., "Synthesis of novel phosphonic-type activity-based probes for neutrophil serine proteases and their application in spleen lysates of different organisms," *ChemBioChem*, vol. 15, no. 17, pp. 2605–2612, 2014.
- [53] E. F. P. Ruivo, L. M. Gonçalves, L. A. R. Carvalho et al., "Clickable 4-oxo- $\beta$ -lactam-based selective probing for human neutrophil elastase related proteomes," *Chem-MedChem*, vol. 11, no. 18, pp. 2037–2042, 2016.
- [54] A.-C. Schulz-Fincke, A. S. Tikhomirov, A. Braune et al., "Design of an activity-based probe for human neutrophil elastase: implementation of the lossen rearrangement to induce Förster resonance energy transfers," *Biochemistry*, vol. 57, no. 5, pp. 742–752, 2018.
- [55] L. E. Edgington, M. Verdoes, and M. Bogyo, "Functional imaging of proteases: recent advances in the design and application of substrate-based and activity-based probes," *Current Opinion in Chemical Biology*, vol. 15, no. 6, pp. 798–805, 2011.
- [56] I. Schechter and A. Berger, "On the size of the active site in proteases. I. Papain," *Biochemical and Biophysical Research Communications*, vol. 27, no. 2, pp. 157–162, 1967.
- [57] J. Bieth and C. G. Wermuth, "The action of elastase on p-nitroanilide substrates," *Biochemical and Biophysical Research Communications*, vol. 53, no. 2, pp. 383–390, 1973.
- [58] J. Bieth, B. Spiess, and C. G. Wermuth, "The synthesis and analytical use of a highly sensitive and convenient substrate

- of elastase," *Biochemical Medicine*, vol. 11, no. 4, pp. 350–357, 1974.
- [59] M. J. Castillo, K. Nakajima, M. Zimmerman, and J. C. Powers, "Sensitive substrates for human leukocyte and porcine pancreatic elastase: a study of the merits of various chromophoric and fluorogenic leaving groups in assays for serine proteases," *Analytical Biochemistry*, vol. 99, no. 1, pp. 53–64, 1979.
- [60] L. P. A. McGarvey, K. Dunbar, S. L. Martin et al., "Cytokine concentrations and neutrophil elastase activity in bronchoalveolar lavage and induced sputum from patients with cystic fibrosis, mild asthma and healthy volunteers," *Journal of Cystic Fibrosis*, vol. 1, no. 4, pp. 269–275, 2002.
- [61] D. S. Armstrong, S. M. Hook, K. M. Jansen et al., "Lower airway inflammation in infants with cystic fibrosis detected by newborn screening," *Pediatric Pulmonology*, vol. 40, no. 6, pp. 500–510, 2005.
- [62] S. Mizukami, K. Kazuya, T. Higuchi et al., "Imaging of caspase-3 activation in HeLa cells stimulated with etoposide using a novel fluorescent probe," *FEBS Letters*, vol. 453, no. 3, pp. 356–360, 1999.
- [63] L. M. Felber, S. M. Cloutier, C. Kündig et al., "Evaluation of the CFP-substrate-YFP system for protease studies: advantages and limitations," *Biotechniques*, vol. 36, no. 5, pp. 878–885, 2004.
- [64] C. Schulenburg, G. Faccio, D. Jankowska, K. Maniura-Weber, and M. Richter, "A FRET-based biosensor for the detection of neutrophil elastase," *The Analyst*, vol. 141, no. 5, pp. 1645–1648, 2016.
- [65] S. Kossodo, J. Zhang, K. Groves et al., "Noninvasive in vivo quantification of neutrophil elastase activity in acute experimental mouse lung injury," *International Journal of Molecular Imaging*, vol. 2011, Article ID 581406, 11 pages, 2011.
- [66] A.-S. Ho, C.-H. Chen, C.-C. Cheng et al., "Neutrophil elastase as a diagnostic marker and therapeutic target in colorectal cancers," *Oncotarget*, vol. 5, no. 2, 2014.
- [67] B. Korkmaz, S. Attucci, M. A. Juliano et al., "Measuring elastase, proteinase 3 and cathepsin G activities at the surface of human neutrophils with fluorescence resonance energy transfer substrates," *Nature Protocols*, vol. 3, no. 6, pp. 991–1000, 2008.
- [68] E. J. Campbell and C. A. Owen, "The sulfate groups of chondroitin sulfate and heparan sulfate-containing proteoglycans in neutrophil plasma membranes are novel binding sites for human leukocyte elastase and cathepsin G," *Journal of Biological Chemistry*, vol. 282, no. 19, article 14645, 2007.
- [69] A. J. O'Donoghue, Y. Jin, G. M. Knudsen et al., "Global substrate profiling of proteases in human neutrophil extracellular traps reveals consensus motif predominantly contributed by elastase," *PLoS One*, vol. 8, no. 9, Article ID e75141, 2013.
- [70] E. Kelly, C. M. Greene, and N. G. McElvaney, "Targeting neutrophil elastase in cystic fibrosis," *Expert Opinion on Therapeutic Targets*, vol. 12, no. 2, pp. 145–157, 2008.
- [71] P. D. Sly, C. L. Gangell, L. Chen et al., "Risk factors for bronchiectasis in children with cystic fibrosis," *New England Journal of Medicine*, vol. 368, no. 21, pp. 1963–1970, 2013.
- [72] P. D. Sly, S. Brennan, C. Gangell et al., "Lung disease at diagnosis in infants with cystic fibrosis detected by newborn screening," *American Journal of Respiratory and Critical Care Medicine*, vol. 180, no. 2, pp. 146–152, 2009.
- [73] S. Gehrig, M. A. Mall, and C. Schultz, "Spatially resolved monitoring of neutrophil elastase activity with ratiometric fluorescent reporters," *Angewandte Chemie International Edition*, vol. 51, no. 25, pp. 6258–6261, 2012.
- [74] R. Weissleder, C.-H. Tung, U. Mahmood, and A. Bogdanov Jr., "In vivo imaging of tumors with protease-activated near-infrared fluorescent probes," *Nature biotechnology*, vol. 17, no. 4, pp. 375–378, 1999.
- [75] F. A. Jaffer, D.-E. Kim, L. Quinti et al., "Optical visualization of cathepsin K activity in atherosclerosis with a novel, protease-activatable fluorescence sensor," *Circulation*, vol. 115, no. 17, pp. 2292–2298, 2007.
- [76] R. A. Sheth, A. Kunin, L. Stangenberg et al., "In Vivo optical molecular imaging of matrix metalloproteinase activity following celecoxib therapy for colorectal cancer," *Molecular imaging*, vol. 11, no. 5, article 7290.2012.00003, 2012.
- [77] C. Bremer, C.-H. Tung, and R. Weissleder, "In vivo molecular target assessment of matrix metalloproteinase inhibition," *Nature medicine*, vol. 7, no. 6, pp. 743–748, 2001.
- [78] M. Sameni, J. Doseescu, and F. Sloane, "Imaging proteolysis by living human glioma cells," *Biological Chemistry*, vol. 382, no. 5, pp. 785–788, 2001.
- [79] S. M. Messerli, S. Prabhakar, Y. Tang et al., "A novel method for imaging apoptosis using a caspase-1 near-infrared fluorescent probe," *Neoplasia*, vol. 6, no. 2, pp. 95–105, 2004.
- [80] F. A. Jaffer, C.-H. Tung, R. E. Gerszten, and R. Weissleder, "In vivo imaging of thrombin activity in experimental thrombi with thrombin-sensitive near-infrared molecular probe," *Arteriosclerosis, Thrombosis, and Vascular Biology*, vol. 22, no. 11, pp. 1929–1935, 2002.
- [81] B. Law, A. Curino, T. H. Bugge, R. Weissleder, and C.-H. Tung, "Design, synthesis, and characterization of urokinase plasminogen-activator-sensitive near-infrared reporter," *Chemistry & Biology*, vol. 11, no. 1, pp. 99–106, 2004.
- [82] V. Fritz, D. Noël, C. Bouquet et al., "Antitumoral activity and osteogenic potential of mesenchymal stem cells expressing the urokinase-type plasminogen antagonist amino-terminal fragment in a murine model of osteolytic tumor," *Stem Cells*, vol. 26, no. 11, pp. 2981–2990, 2008.
- [83] J. V. Edwards, N. T. Prevost, A. D. French, M. Concha, and B. D. Condon, "Kinetic and structural analysis of fluorescent peptides on cotton cellulose nanocrystals as elastase sensors," *Carbohydrate Polymers*, vol. 116, pp. 278–285, 2015.
- [84] P. Massot, E. Parzy, L. Pourtau et al., "In vivo high-resolution 3D overhauser-enhanced MRI in mice at 0.2 T," *Contrast Media & Molecular Imaging*, vol. 7, no. 1, pp. 45–50, 2012.
- [85] N. Koonjoo, E. Parzy, P. Massot et al., "In vivo overhauser-enhanced MRI of proteolytic activity," *Contrast Media & Molecular Imaging*, vol. 9, no. 5, pp. 363–371, 2014.
- [86] N. Jugniot, I. Duttagupta, A. Rivot et al., "An elastase activity reporter for electronic paramagnetic resonance (EPR) and overhauser-enhanced magnetic resonance imaging (OMRI) as a line-shifting nitroxide," *Free Radical Biology and Medicine*, vol. 126, pp. 101–112, 2018.
- [87] M. W. Crystal, K. A. Hilliard, T. M. Norvell, and M. Berger, "Bronchoalveolar lavage findings in cystic fibrosis patients with stable, clinically mild lung disease suggest ongoing infection and inflammation," *American Journal of Respiratory and Critical Care Medicine*, vol. 150, no. 2, pp. 448–454, 1994.
- [88] D. Moncelet, P. Voisin, N. Koonjoo et al., "Alkoxyamines: toward a new family of theranostic agents against cancer," *Molecular Pharmaceutics*, vol. 11, no. 7, pp. 2412–2419, 2014.
- [89] K. Akazawa, F. Sugihara, M. Minoshima, S. Mizukami, and K. Kikuchi, "Sensing caspase-1 activity using activatable 19F MRI nanoprobe with improved turn-on kinetics," *Chemical Communications*, vol. 54, no. 83, pp. 11785–11788, 2018.

- [90] X. Yue, Z. Wang, L. Zhu et al., “Novel  $^{19}\text{F}$  activatable probe for the detection of matrix metalloprotease-2 activity by MRI/MRS,” *Molecular Pharmaceutics*, vol. 11, no. 11, pp. 4208–4217, 2014.
- [91] M. Suchý, R. Ta, A. X. Li et al., “A paramagnetic chemical exchange-based MRI probe metabolized by cathepsin D: design, synthesis and cellular uptake studies,” *Organic & Biomolecular Chemistry*, vol. 8, no. 11, p. 2560, 2010.
- [92] D. V. Hingorani, L. A. Montano, E. A. Randtke, Y. S. Lee, J. Cárdenas-Rodríguez, and M. D. Pagel, “A single diamagnetic catalyCEST MRI contrast agent that detects cathepsin B enzyme activity by using a ratio of two CEST signals,” *Contrast Media & Molecular Imaging*, vol. 11, no. 2, pp. 130–138, 2016.
- [93] M. D. Pagel, B. Yoo, G. Liu, and R. Rosenblum, “CMR 2005: 13.06: activatable MRI CEST agents that detect enzyme activities,” *Contrast Media & Molecular Imaging*, vol. 1, no. 2, pp. 88–89, 2006.
- [94] B. Yoo, V. R. Sheth, C. M. Howison et al., “Detection of in vivo enzyme activity with catalyCEST MRI,” *Magnetic Resonance in Medicine*, vol. 71, no. 3, pp. 1221–1230, 2014.
- [95] S. Chakraborti, T. Chakraborti, and N. S. Dhalla, *Proteases in Human Diseases*, Springer, Berlin, Germany, 2017.
- [96] Y. Wang and M. Deng, “Medical imaging in new drug clinical development,” *Journal of Thoracic Disease*, vol. 2, pp. 245–252, 2010.
- [97] R. Stockley, A. De Soyza, K. Gunawardena et al., “Phase II study of a neutrophil elastase inhibitor (AZD9668) in patients with bronchiectasis,” *Respiratory Medicine*, vol. 107, no. 4, pp. 524–533, 2013.
- [98] H. Watz, J. Nagelschmitz, A. Kirsten et al., “Safety and efficacy of the human neutrophil elastase inhibitor BAY 85-8501 for the treatment of non-cystic fibrosis bronchiectasis: a randomized controlled trial,” *Pulmonary Pharmacology & Therapeutics*, vol. 56, pp. 86–93, 2019.
- [99] J. Holland, “The role of molecular imaging in personalised healthcare,” *CHIMIA International Journal for Chemistry*, vol. 70, no. 11, pp. 787–795, 2016.
- [100] European Alliance for Personalised Medicine—Innovation and patient Access to personalised medicine, [http://euapm.eu/pdf/EAPM\\_REPORT\\_on\\_Innovation\\_and\\_Patient\\_Access\\_to\\_Personalised\\_Medicine.pdf](http://euapm.eu/pdf/EAPM_REPORT_on_Innovation_and_Patient_Access_to_Personalised_Medicine.pdf).

## Review Article

# Renal Allograft Rejection: Noninvasive Ultrasound- and MRI-Based Diagnostics

Ulrich Jehn <sup>1</sup>, Katharina Schuette-Nuetgen,<sup>1</sup> Dominik Kentrup,<sup>1,2</sup> Verena Hoerr,<sup>3,4</sup> and Stefan Reuter <sup>1</sup>

<sup>1</sup>Department of Medicine, Division of General Internal Medicine, Nephrology and Rheumatology, University Hospital of Muenster, 48149 Muenster, Germany

<sup>2</sup>Department of Medicine, Division of Nephrology, The University of Alabama at Birmingham (UAB), 35294 Birmingham, Alabama, USA

<sup>3</sup>Department of Clinical Radiology, University Hospital of Muenster, 48149 Muenster, Germany

<sup>4</sup>Institute of Medical Microbiology, Jena University Hospital, Am Klinikum 1, 07747 Jena, Germany

Correspondence should be addressed to Stefan Reuter; [stefan.reuter@ukmuenster.de](mailto:stefan.reuter@ukmuenster.de)

Received 24 January 2019; Accepted 26 March 2019; Published 10 April 2019

Guest Editor: Sarah Ohrndorf

Copyright © 2019 Ulrich Jehn et al. This is an open access article distributed under the Creative Commons Attribution License, which permits unrestricted use, distribution, and reproduction in any medium, provided the original work is properly cited.

To date, allogeneic kidney transplantation remains the best available therapeutic option for patients with end-stage renal disease regarding overall survival and quality of life. Despite the advancements in immunosuppressive drugs and protocols, episodes of acute allograft rejection, a sterile inflammatory process, continue to endanger allograft survival. Since effective treatment for acute rejection episodes is available, instant diagnosis of this potentially reversible graft injury is imperative. Although histological examination by invasive core needle biopsy of the graft remains the gold standard for the diagnosis of ongoing rejection, it is always associated with the risk of causing substantial graft injury as a result of the biopsy procedure itself. At the same time, biopsies are not immediately feasible for a considerable number of patients taking anticoagulants due to the high risk of complications such as bleeding and uneven distribution of pathological changes within the graft. This can result in the wrong diagnosis due to the small size of the tissue sample taken. Therefore, there is a need for a tool that overcomes these problems by being noninvasive and capable of assessing the whole organ at the same time for specific and fast detection of acute allograft rejection. In this article, we review current state-of-the-art approaches for noninvasive diagnostics of acute renal transplant inflammation, i.e., rejection. We especially focus on nonradiation-based methods using magnetic resonance imaging (MRI) and ultrasound.

## 1. Introduction

Kidney transplantation (KTx) is the most preferred treatment for patients suffering from end-stage renal disease (ESRD) [1], as it offers enormously better survival rates compared to other renal replacement therapies [2]. Ongoing progress in transplantation medicine results in better success rates of organ transplantation and a prolongation of renal allografts' half-life. [3, 4] Despite the considerable progress of immunosuppressive regimens, acute rejection (AR) still remains a serious issue after KTx, which decreases patient and graft survival rates after its occurrence [5, 6].

AR depicts a condition of sterile inflammation, either antibody or/and T cell mediated.

While the T cell or cellular-mediated rejection (TCMR) usually occurs early after transplantation and is more prevalent, humoral or antibody-mediated AR (AMR) occurs later in fewer patients [7, 8]. Overall, 13–53% of kidney recipients develop an episode of AR within one year after transplantation [9]. The risk of progression to chronic allograft damage with consecutive reduced long-term survival increases with every episode of AR [10, 11]. Chronic allograft failure constitutes still the main cause for death-censored graft loss after KTx [12, 13]. This underlines the importance of early detection and specific treatment for AR.

Transplantation from genetically different tissues involuntarily induces a recipient's immune response against the alloantigens. The formation of antibodies against donor-specific HLA-antigens is a key feature of AMR. Moreover, numerous non-HLA antibodies directed against both alloantigens and autoantigens have been identified to potentially initiate allograft rejection [14]. A critical immunological event inevitably caused by transplantation is related to the ischemia-reperfusion injury of the graft, leading, for example, to an upregulation of expressed HLA antigens in the graft on one side and initiating an inflammatory state on the other side [8]. Moreover, the donor organ transfers immune competent cells to the recipient which may trigger rejection [15].

TCMR is induced by recipient's antigen-presenting cells, which present donor antigens to T-lymphocytes with following activation and differentiation of these cytotoxic T-lymphocytes (CTLs) [16]. Besides CTLs and other leukocyte subtypes, the complement system contributes to the inflammation as well. Once activated, CTLs expand and differentiate into effector cells, extravasate, and subsequently infiltrate the transplant [7, 17]. Different chemokines, cytokines, and the upregulation of vascular adhesion molecules guide this process [18], finally leading to necrotic parenchymal destruction or initiation of apoptosis [19, 20].

Owing to modern efficacious immunosuppressants, the clinical presentation of renal allograft rejection episodes has changed from fever and graft tenderness to an often subclinical manifestation characterized by increasing proteinuria, elevation of serum creatinine, or solely histological changes, which hinders early recognition [21].

Gold standard for diagnosis of allograft rejection is the histopathologic evaluation of core needle biopsies by applying international consensus criteria, the Banff classification [21]. The biopsy procedure potentially causes serious complications for the allograft recipient, and it also underlies distinct contraindications. Therefore, noninvasive techniques to detect AR would be a key advancement for this field.

Apart from structural details, ultrasound- and MRI-based techniques nowadays are also capable to visualize functional and biological processes to some extent in the context of the abovementioned inflammatory processes that accompany AR.

As transplant recipients require active surveillance and frequent assessments of the graft's condition, we provide a review of the current nonradiation-based, noninvasive imaging techniques to detect AR that might help reduce the need for biopsies in the future. All technical approaches bare the potential to be used (in a modification) for the diagnoses of AR in other transplant organs than the kidney as well.

## 2. Ultrasound

Over the last four years, significant progress has been made particularly in the field of ultrasound- and MRI-based techniques. Sonographic examination is one of the most valuable clinical tools for patients' assessment. It is widely available and routinely utilized to monitor specific

properties such as perfusion, resistance indices etc., of the graft after organ transplantation. The parameters assessed include unspecific features of AR such as enlargement of the transplant caused by swelling, abatement of corticomedullary differentiation, change in echogenicity, and distinctive structures such as medullary pyramids. Analysis of the perfusion of the grafts can be performed with Doppler ultrasound and contrast-enhanced ultrasound (CEUS) examination. Sonography is advantageous due to its innocuousness, cost-effectiveness, and wide availability. However, on the downside, it has limitations with regard to sensitivity and specificity for AR until now.

Recent approaches have addressed these limitations and offered potential solutions to overcome them. One of those approaches is the assessment of the resistive index (RI) [22], which increases when grafts undergo antibody-mediated rejection. While using the RI, one has to keep in mind that it is increased in cases of acute tubular necrosis (ATN) as well, and the systemic resistance of the vasculature, pulse pressure, and heart rate and rhythm also contribute to it. Thus, RI cannot be precisely assessed in patients with atrial fibrillation for instance, and it is significantly influenced by the recipient's age or dialysis time before the transplantation. While it is associated with overall survival, its usefulness for the prediction of graft survival is questionable [22–24].

A further ultrasound-based approach uses CEUS, which involves the use of either intravenously applied microbubble-based contrast agents to increase the echogenicity of blood or targeted microbubble-based contrast agents addressing specific tissues. CEUS parameters of interest are rising time, time to peak, and delta-time among other regions of interest [25]. Conventional CEUS cannot be used for the definitive detection of AR, since the increase in the echogenicity of blood is the only indicator. It is capable to visualize and quantify renal perfusion abnormalities suspicious of acute vascular rejection, but not sufficient to distinguish these abnormalities from other causes of abnormal perfusion [26]. A more specific detection of AR becomes a possibility when microbubble-based contrast agents targeted against T cells are used. By labeling the contrast agent with specific antibodies (for instance, against T cell surface antigen CD3 or other T cell surface antigens like CD8 or CD4), the echogenicity of the graft can be sufficiently increased to enable the reliable diagnosis of AR (Figure 1) [27].

The acquired ultrasound signal intensities also increase with the severity of inflammation, indicating a possible measure of the degree of AR with this method. Furthermore, through targeted CEUS, it was possible to differentiate AR from ATN and acute calcineurin inhibitor toxicity. CEUS demonstrated the capability of therapeutic monitoring of the immunosuppressive treatment of manifest AR, as signal intensity distinctly decreased 24 hours after beginning of rejection therapy.

Therefore, since the pathological mechanism of acute T cell mediated rejection can be observed in cases of AR in other transplanted solid organs, CEUS can potentially detect AR in other organs as well [27].

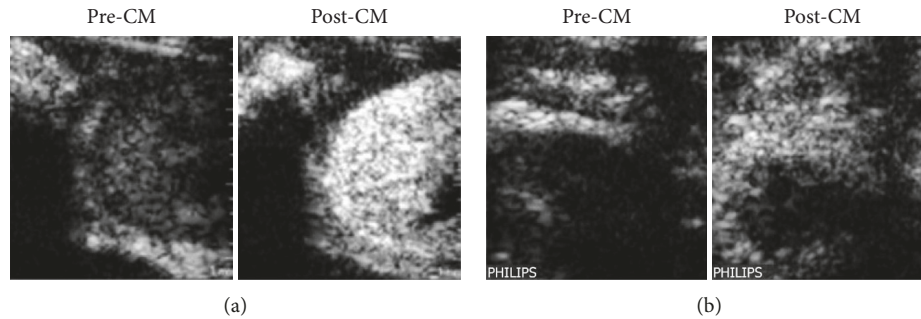


FIGURE 1: Representative ultrasound images of an allogeneic kidney transplantation in a rat (atx, allograft) (a): its native control kidney (native)(b) 4 days after transplantation before (pre-CM), 15 minutes after tail vein injection of microbubbles labeled with an antibody targeted against CD3 positive T cells (post-CM). CM: contrast media/microbubbles conjugated with anti-CD3 antibody [28].

Liao et al. demonstrated in a rat study that C4d can also serve as a target for labeled microbubbles to detect and visualize C4d deposition by means of CEUS in glomeruli and peritubular capillaries as a characteristic of antibody-mediated rejection (AMR) [29], which represents the leading cause of kidney allograft loss [30]. This method also allows quantitative analysis of C4d deposition via normalized intensity differences (NID) [29].

However, for the translation of these approaches to the human body, the immunogenic streptavidin-based conjugation between the microbubble-based contrast agent and the appropriate antibody requires modification.

In another recent study, Meier et al. investigated if a newly developed serial duplex index (SDI) can be used to differentiate between AR and acute vascular rejection more effectively in comparison with the established Doppler parameters RI and pulsatility index (PI) in the first days after the transplantation [31]. The PI represents a Doppler derived index that depends on downstream renal artery resistance and stiffness [32]. Based on the parameters RI, PI, and cortex-pelvis proportion (CPP) calculated on the day of the biopsy ( $t_0$ ) and 3 to 7 days before the biopsy, the SDI was calculated as  $RI \text{ ratio} \times PI \text{ ratio} / CPP \text{ ratio}$ . A retrospective analysis of 121 patients revealed that the SDI was significantly different between patients with normal graft function, acute cellular rejection, and acute vascular rejection. The RI and PI ratios were significantly different only between patients with normal graft function and acute vascular rejection. The developed SDI was able to detect acute renal transplant rejection with greater sensitivity and specificity than the RI and PI ratios, thus it might be helpful to indicate renal biopsy in the future [31]. Nevertheless, this method lacks prospective evaluation.

A different ultrasound-based technique, evaluated to detect AR, was described by Jiménez et al. in 2016. They performed real-time contrast-enhanced sonography (RT-CES) to investigate cortical capillary blood flow (CCBF) after kidney transplantation. RT-CES provides an analysis and quantification of vascular refilling in any region of interest (for instance, the renal cortex) by depicting the destruction of injected microbubbles through an ultrasound pulse. The refilling of a certain area is an indicator of tissue perfusion. A secondary aim was to explore the influences of

AR, acute tubular necrosis, and calcineurin inhibitor toxicity on CCBF, even though this study was not designed to specifically determine these differences [33].

Although AR is associated with lower CCBF in general, CCBF did not demonstrate sufficient sensitivity to distinguish rejection due to tissue edema and cellular infiltration [34]. Unfortunately, RI and CCBF did not correlate with any of the analyzed timepoints (48 h, 5–7 days, and 1, 3, and 12 months after transplantation), possibly because CCBF reflects both donor and graft characteristics, as it can be deduced by the CCBF correlation with donor's age, AR episodes, and living vs. brain-death donor. The authors hypothesized that CCBF would reflect the basal vasculature state from the donor early after transplantation, and later this state would be changed by inflammatory events after transplantation [33].

Yang et al. utilized point shear wave elastography (p-SWE) based on acoustic radiation force (ARF) impulse to quantify tissue stiffness by measuring shear wave speed (SWS) in a prospective study with 115 KTx recipients [35]. The technical principle was already established for detection and quantification of liver fibrosis [36]. The shear wave speed was found to be significantly higher in patients with AR than in the non-AR patients. The authors invented a model called the SEV index that comprised of the parameters SWS, estimated glomerular filtration rate, and kidney volume change for noninvasive detection of AR. In kidneys undergoing AR, SWS was significantly increased (reflecting an increase in parenchymal stiffness) as compared to non-AR kidneys, including stable functioning grafts and ATN kidneys. Thus, SWS analysis for the detection of AR might hold potential. Since kidney volume significantly increases in patients with AR, the authors hypothesized that the edema formed during AR could increase intrarenal pressure due to the strong fibrous capsule surrounding the kidney. This mechanism might be responsible for the observed increased stiffness. In contrast to AR, ATN, which is another common cause for delayed graft function, was additionally associated with a significantly decreased graft volume [35].

A more recent prospective study to evaluate the value of SWS for the differentiation of stable allograft function from acute and chronic allograft dysfunction was performed by Ghonge et al. The study revealed that SWS can help to

differentiate stable allograft function from acute and chronic dysfunction in addition to laboratory and Doppler-based parameters [37].

Kim et al. investigated the worthwhile issue of diagnosing subclinical kidney allograft rejection (SCR) in stable functioning grafts by quantifying tissue elasticity with SWE to identify rejection episodes at a stage with better treatment options. They examined 95 patients who underwent protocol biopsies either 10 days or 1 year after Tx and exhibited a stable allograft function. 34 of them showed histological characteristics of acute rejection. The authors could demonstrate that tissue elasticity was significantly increased in patients with SCR compared to those without in univariate analysis, without being an independent predictor of SCR in multivariate analysis. No differences in tissue elasticity could be found between the histological subtypes of rejection [38]. Important but difficult to control confounding factors of quantitative SWE measurement are amongst others different depths of the allograft and its movement, different pressures of the transducer, and the exact incident angle of the acoustic beam [38, 39].

Viscoelastic response (VisR) ultrasound is an alternative ARF-based tool using two co-localized ARF impulses to delineate tissue properties by measuring viscosity and elasticity (for details, see [40]). Hossain et al. performed a prospective study with 44 patients to examine the ability of VisR to evaluate renal transplant status. This study revealed the feasibility of VisR to significantly differentiate between control allografts and those harboring pathological features. Nevertheless, it was not sufficient to discriminate specifically between various graft pathologies. Hence, VisR could help to preserve patients without a structural graft pathology against unnecessary biopsies but is not able to replace biopsies in patients showing a suspicious VisR finding [41].

### 3. MRI

The natural magnetic properties of hydrogen nuclei can be detected in a magnetic field with the use of magnetic resonance imaging (MRI). The strength of MRI lies in its excellent intrinsic soft tissue contrast, unlimited penetration depth, and high anatomical resolution in addition to the functional assessment of the graft. The technique is capable of differentiating tissue characteristics based on intrinsic MR properties such as  $T_1$  and  $T_2$  relaxation times, water content, and diffusivity [42]. Thus, MRI facilitates the detection of distinctive features of vascular and interstitial structures.

Different MRI techniques have already been successfully applied to discriminate between different causes of renal allograft injury such as AR and ATN, and they allow (to some extent) the visualization of the pathophysiological processes underlying the respective type of injury [42, 43].

**3.1. Renal Function.** A common MRI method to assess renal function is dynamic contrast enhanced MRI (DCE MRI). It depends on gadolinium-based contrast agent protocols, and it is also termed MR renography (MRR). The contrast agents used in this technique are freely filtered across the glomeruli

yet not secreted or reabsorbed in the tubules ideally. Due to these specific characteristics, it optimally assesses renal perfusion, glomerular filtration rate (GFR), and tubular function that has been proved useful for discrimination between AR and ATN [43]. One pathological feature of renal grafts undergoing AR is a significantly reduced cortical and medullary blood flow compared to nonrejected grafts [44–47]. The reduced medullary blood flow in grafts with AR seems to be characteristic to distinguish between AR and ATN in particular [48].

Yamamoto et al. proved the feasibility of discrimination between several types of allograft impairment using a new quantitative analysis method of MRR. They implemented a multicompartamental kinetic kidney model to determine the mean transit time (MTT) of a contrast agent through the different compartments of the kidney. Even though some significant differences in the fractional MTT values between normal grafts or grafts undergoing AR or ATN were obtained, substantial overlaps were observed when these groups were compared with themselves and with healthy control kidneys [47].

Notably, the application of gadolinium-based MRI to patients with severely impaired renal function potentially accompanies the rare but deleterious side effect of contrast-induced nephrogenic systemic fibrosis [49]. Moreover, recent findings revealed the association of intravenous exposure to especially linear gadolinium-containing complexes with neuronal tissue deposition in patients with normal renal function as well. The clinical significance of that finding is undiscovered so far [50].

In contrast, arterial spin labeling (ASL) is an MRI tool that utilizes arterial blood flow as an endogenous contrast agent, and it allows the study of allograft function, particularly by longitudinal perfusion evaluation. It comprises of two acquisitions, one labeled by modifying the longitudinal magnetization of arterial blood water and a control acquisition obtained without arterial labeling. The labeled protons find their way via the arterial bloodstream to the targeted tissue, where they pass from the intra- to the extravascular compartment and reduce the equilibrium magnetization slightly by a few percent. Imaging is performed at time  $T_1$  (inversion time) after the pulsed labeling with the use of a rapid imaging technique, owing to the time required for the labeled protons to perfuse the tissue. In the control acquisition, arterial protons at the target structure are relaxed and in equilibrium. Methods for ASL and labeling pulses can be categorized into continuous (CASL), pulsed (PASL), and velocity-selective (VSASL) techniques [51]. The subtraction of the labeled and control acquisitions suppresses the signal from the static tissue and provides a perfusion-weighted image. Quantitative perfusion maps can be calculated with the use of various TIs (Figure 2(a)). ASL studies using a flow-sensitive alternating inversion recovery (FAIR-ASL) scheme (for details about FAIR-ASL, see [52]) reveal a significant lower perfusion in allografts vs. native kidneys [53]. In conjunction with this, renal allografts with acute decrease in renal function showed a significant lower cortical perfusion when compared to those with steady function in the long-term and the postoperative period [54]. However, the

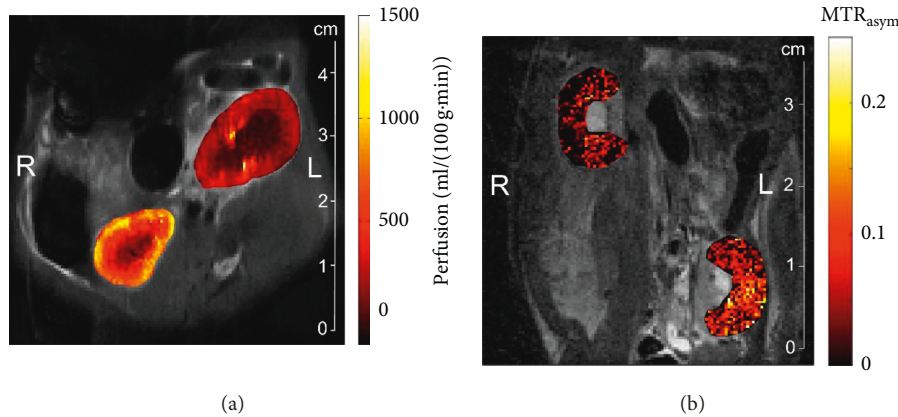


FIGURE 2: Representative in vivo ASL perfusion (a) and glucoCEST  $MTR_{\text{asym}}$  (b) maps of the renal cortex and medulla of an allogeneic transplantation in a rat on day 4 posttransplantation, showing the renal allograft undergoing an acute cellular rejection on the right side (L) and the healthy right contralateral kidney on the left side (R).

underlying disease leading to the decrease in perfusion has not been identified.

Another approach for the functional examination of transplanted kidneys to distinguish between AR and ATN is exploitation of the paramagnetic properties of deoxyhemoglobin via blood-oxygen level dependent (BOLD) MR [55–58]. Deoxyhemoglobin accumulates in tissues with lower oxygen concentration. It is strongly paramagnetic due to its unpaired electrons at the iron centre and thus leads to a shortened transverse relaxation time constant  $T_2^*$ . Inversely, the apparent relaxation rate  $R_2^* (= 1/T_2^*)$  is elevated. In this context, BOLD MR is feasible in providing information about renal parenchymal oxygen concentration [55]. In AR kidney allografts, medullary  $R_2^*$  values decrease significantly, corresponding to a higher oxygenation in comparison with kidneys with ATN. Interestingly, this observation was accompanied by a reduced medullary blood flow assessed by perfusion MR which appears contradictory [55]. The increase in oxygen consumption by active tubular reabsorption whenever filtration and blood flow rise together may be a causal factor for this. As a consequence, regional oxygen tension is not as strongly associated with regional blood flow as in other organs [59].

**3.2. Renal Structure and Morphology.** Diffusion-weighted MRI (DWI MRI) is a contrast agent-independent MRI technique that depends on the signal decay induced by relative diffusion-based displacement of water molecules. It can be quantified by calculating the apparent diffusion coefficient (ADC). The ADC is influenced by the tissue microstructure and separated from the directionality of molecular motion, thus ADC values represent a measure for tissue diffusivity [60, 61].

Hueper et al. recently performed a study wherein they investigated mice after isogenic and allogeneic KTx at day 1 and day 6 after the transplantation. They used a combination of both functional MRI techniques—DWI and mapping of  $T_2$ -relaxation time ( $T_2$ -mapping)—to investigate the severity and course of inflammation and edema formation following KTx during the development of AR and IRI.

The authors observed a progressive ADC reduction in allogeneic grafts when compared to isogenic grafts and normal kidneys, which correlated to histologic findings of tissue inflammation corresponding to AR.

$T_2$  relaxation times increased as a correlate for tissue edema, and this was observed in both transplantation groups. The authors assumed that the acute kidney injury of the graft following prolonged cold ischemia time was responsible for this finding. Interestingly, only the allogeneic group showed an abrogated  $T_2$ -difference between the renal compartments, which indicates a disturbance of physiological differences of tissue water content.

Therefore, Hueper et al., who used a 7 T MRI scanner for their study, concluded that morphological MRI clearly allowed differentiation between allogeneic kidney grafts with AR and isogenic kidney grafts with IRI and provided detailed tissue information with regard to the graft using DWI and  $T_2$ -mapping. In this case, one limitation might be that edema formation interferes with diffusion and T cell invasion which is able to alter  $T_2$ -relaxation.

In order to translate this into clinical practice, two issues have to be considered: first, renal anatomy and physiology of mice differ from humans, and second, clinical MRI scanners usually remain in the range of 1.5–3 T in contrast to 3–9.4 T frequently used in rodent studies. Thus, MRI parameters may differ [62].

For imaging of renal structures, diffusion tensor imaging (DTI) is a more sensitive MRI-based approach that has been applied by Lanzman et al. By sampling several different diffusion directions, DTI addresses the issue of anisotropic diffusion properties due to the radial orientation of main anatomic structures like vessels and tubules. DTI is an effective tool for the assessment of the fractional anisotropy, which is a measure for directionality of diffusion in tissues [63, 64].

**3.3. Molecular Imaging.** Several studies have utilized nanoparticles to specifically detect immune cells or immune proteins in the kidney by using MRI to image the pathophysiological processes that occur when undergoing rejection (for a review, see [65]).

Hauger et al. and Chae et al. proposed application of superparamagnetic iron oxide (SPIO) particle-loaded macrophages to investigate native and transplanted kidney grafts. The first study mentioned was performed in human patients, and the latter in a rat model. Imaging of macrophage infiltration was performed three and five days after the application of the contrast agent. SPIOs cause local field distortion and result in a strong reduction of the relaxation time constant  $T_2^*$ . Hauger et al. found a specific MR pattern for ATN that may be helpful in distinguishing ATN from AR. Furthermore, they were able to successfully discriminate between inflammatory and noninflammatory causes of kidney failure. However, the significant delay between contrast agent application and data acquisition is a strong limitation of this procedure. Moreover, imaging of phagocyte activity is unspecific, as these cells participate in different inflammatory events in the kidney. Chae et al. demonstrated macrophage homing using MRI in their allograft rejection model. However, other causes of graft failure besides AR were not investigated in their study. Unfortunately, nonphagocytic cells, such as T cells, which are more specific to AR, generally present a low SPIO-labeling efficiency and poor contrast agent uptake. Currently, this is a significant limitation to cellular MR imaging *in vivo* [66, 67].

Polyethylene glycol-coated superparamagnetic nano-sized iron-oxide particles constitute a new synthesized class of MRI contrast agent. These particles were tested for the labeling of T cells in a rat model of AR after heart-lung transplantation with a T cell purity of about 90% [68]. This technique offers an approach to track nonphagocytic cells, such as T- and B-lymphocytes, and it may also potentially be translated into clinical application for detection of AR after KTx. It must be mentioned critically that the authors of this study did not regard the 10% non-T cells and their impact. In addition, the labeling is not permanent, and most of the labeling signal shown remains extracellular due to the sticky particles adhering to the plasma membrane of these cells.

Recently, we published a new MRI-based approach called glucoCEST for noninvasive and differential *in vivo* studies of renal allograft injuries. This technique aims to assess regional tissue glucose content. GlucoCEST uses D-glucose as a naturally occurring biodegradable MRI contrast agent, which can be monitored by chemical exchange saturation transfer (CEST) [69].

The measurement of AR-related regional glucose accumulation helped to differentiate AR from syngeneic grafts without AR, kidneys with IRI, and kidneys with cyclosporine A- (CsA-) induced toxicity. The technique involved the calculation of a  $MTR_{asym}$  contrast ratio of cortex to medulla, which was found to be significantly increased in AR compared to the other subgroups (Figure 2(b)). The differentiation of AR from major clinical differential diagnoses of delayed graft function like IRI and CsA toxicity is an important advancement of this new method. Additionally, this approach successfully monitored a response of AR to immunosuppressive treatment at an early point of time [70].

The feasibility of clinical translation for the glucoCEST technique has already been demonstrated in patients with

glioma [71]. Therefore, we are convinced this could be a promising approach for noninvasive detection of AR in humans.

#### 4. Conclusion

New innocuous and sensitive diagnostic tools for the detection of AR assessing the whole organ, particularly in differential diagnostics of delayed graft function, are highly desired. Two particularly suited applications to address this issue are ultrasound and MRI. Advances in technology and contrast agent development have opened new possibilities in this regard. At present, all of these promising new technologies are still at an experimental stage and have yet either to be transferred from animal models to clinics or to be refined to prove an advantage over standardly applied core needle biopsy. For the moment, they are partly capable to better identify patients in need of a kidney allograft biopsy and they offer the potential to advance the clinical routine for noninvasive and specific diagnosis of AR as well as the longitudinal surveillance monitoring of the allograft. The biggest advantage of ultrasound-based diagnostics over MRI-based ones is their broad availability, their potential for bedside and real-time diagnostics, and the relatively low costs. However, in contrast to MRI, ultrasound-based diagnostics has a substantial interobserver variability and needs experienced investigators. Furthermore, most MRI sequences are already available for clinical scanners.

However, detection approaches for structural, morphological, or functional features by ultrasound (perfusion, arterial blood flow, stiffness, elasticity, and viscosity) as well as MRI (perfusion, arterial blood flow, tubular function, tissue diffusivity, and oxygen concentration) lack specificity for the detection of AR; imaging of characteristic molecular biological processes with both ultrasound (T cell migration and C4d deposition) and MRI (macrophage infiltration, T cell migration, and glucose accumulation) bares the potential to overcome this hurdle.

Of course, rejections can occur in every allogenic transplant. Accordingly, the reviewed techniques for noninvasive detection of renal allograft rejection are principally adaptable to other allogenic transplanted solid organs.

#### Abbreviations

ADC:	Apparent diffusion coefficient
ARF:	Acoustic radiation force
ARFI:	Acoustic radiation force impulse imaging
AMR:	Acute antibody-mediated rejection
AR:	Acute rejection
ASL:	Arterial spin labeling
ATN:	Acute tubular necrosis
BOLD:	Blood-oxygen level dependent
CCBF:	Cortical capillary blood flow
CD:	Cluster of differentiation
CEST:	Chemical exchange saturation transfer
CEUS:	Contrast-enhanced ultrasound
CPP:	Cortex-pelvis proportion
CSA:	Cyclosporine A

CT:	Computed tomography
CTL:	Cytotoxic T-lymphocytes
DCE:	Dynamic contrast enhanced
DTI:	Diffusion tensor imaging
DWI:	Diffusion-weighted
ESRD:	End-stage renal disease
FAIR-ASL:	Flow-sensitivity alternating inversion recovery
GFR:	Glomerular filtration rate
HLA:	Human leukocyte antigen
IRI:	Ischemia-reperfusion injury
KTx:	Kidney transplantation
MR:	Magnetic resonance
MRI:	Magnetic resonance imaging
MRR:	Magnetic resonance renography
MTT:	Mean transit time
NID:	Normalized intensity differences
PI:	Pulsatility index
p-SWE:	Point-shear wave elastography
RI:	Resistive index
RT-CES:	Real-time contrast-enhanced sonography
SCR:	Subclinical kidney allograft rejection
SDI:	Serial duplex index
SPIO:	Ultrasmall supermagnetic iron oxide
SWEI:	Shear wave sonoelastography
SWS:	Shear wave speed
T:	Tesla
TCMR:	T cell mediated rejection
TI:	Inversion time
VISR:	Viscoelastic response ultrasound.

## Disclosure

The funders had no role in study design, data collection and analysis, decision to publish, or preparation of the manuscript.

## Conflicts of Interest

The authors declare that there are no conflicts of interest.

## Authors' Contributions

Jehn U wrote the paper; Schuette-Nuetgen K, Kentrup D, and Hoerr V performed research and wrote the paper; and Reuter S designed research and wrote the paper.

## Acknowledgments

The authors acknowledge the support by Open Access Publication Fund of University of Münster and the Collaborative Research Centre 656 (Deutsche Forschungsgemeinschaft, SFB656, Projects C7, and PM12 and 21).

## References

- [1] R. A. Wolfe, V. B. Ashby, E. L. Milford et al., "Comparison of mortality in all patients on dialysis, patients on dialysis awaiting transplantation, and recipients of a first cadaveric transplant," *New England Journal of Medicine*, vol. 341, no. 23, pp. 1725–1730, 1999.
- [2] G. G. Garcia, P. Harden, J. Chapman, and World Kidney Day Steering Committee 2012, "The global role of kidney transplantation," *Nephrology Dialysis Transplantation*, vol. 28, no. 8, pp. e1–e5, 2013.
- [3] A. Lemy, M. Andrien, A. Lionet et al., "Posttransplant major histocompatibility complex class I chain-related gene A antibodies and long-term graft outcomes in a multicenter cohort of 779 kidney transplant recipients," *Transplantation Journal*, vol. 93, no. 12, pp. 1258–1264, 2012.
- [4] K. P. McCullough, D. S. Keith, K. H. Meyer, P. G. Stock, K. L. Brayman, and A. B. Leichtman, "Kidney and pancreas transplantation in the United States, 1998–2007: access for patients with diabetes and end-stage renal disease," *American Journal of Transplantation*, vol. 9, no. 4p2, pp. 894–906, 2009.
- [5] A. Elbadri, C. Traynor, J. T. Veitch et al., "Factors affecting eGFR 5-year post-deceased donor renal transplant: analysis and predictive model," *Renal Failure*, vol. 37, no. 3, pp. 417–423, 2015.
- [6] M. Jalalzadeh, N. Mousavinasab, S. Peyrovi, and M. H. Ghadiani, "The impact of acute rejection in kidney transplantation on long-term allograft and patient outcome," *Nephro-Urology Monthly*, vol. 7, no. 1, article e24439, 2015.
- [7] L. D. Cornell, R. N. Smith, and R. B. Colvin, "Kidney transplantation: mechanisms of rejection and acceptance," *Annual Review of Pathology: Mechanisms of Disease*, vol. 3, no. 1, pp. 189–220, 2008.
- [8] B. J. Nankivell and S. I. Alexander, "Rejection of the kidney allograft," *New England Journal of Medicine*, vol. 363, no. 15, pp. 1451–1462, 2010.
- [9] D. J. Cohen, L. St. Martin, L. L. Christensen, R. D. Bloom, and R. S. Sung, "Kidney and pancreas transplantation in the United States, 1995–2004," *American Journal of Transplantation*, vol. 6, no. 5p2, pp. 1153–1169, 2006.
- [10] A. J. Matas, K. J. Gillingham, W. D. Payne, and J. S. Najarian, "The impact of an acute rejection episode on long-term renal allograft survival (t1/2)1,2," *Transplantation*, vol. 57, no. 6, pp. 857–859, 1994.
- [11] O. Wu, A. R. Levy, A. Briggs, G. Lewis, and A. Jardine, "Acute rejection and chronic nephropathy: a systematic review of the literature," *Transplantation*, vol. 87, no. 9, pp. 1330–1339, 2009.
- [12] J. R. Chapman, P. J. O'Connell, and B. J. Nankivell, "Chronic renal allograft dysfunction," *Journal of the American Society of Nephrology*, vol. 16, no. 10, pp. 3015–3026, 2005.
- [13] A. A. Awan, J. Niu, J. S. Pan et al., "Trends in the causes of death among kidney transplant recipients in the United States (1996–2014)," *American Journal of Nephrology*, vol. 48, no. 6, pp. 472–481, 2018.
- [14] A. Loupy and C. Lefaucheur, "Antibody-mediated rejection of solid-organ allografts," *New England Journal of Medicine*, vol. 379, no. 12, pp. 1150–1160, 2018.
- [15] J. P. Stone, M. Mohamad, K. Amin et al., "Characterizing the early inflammatory contribution of the donor kidney following reperfusion," *Nephrology Dialysis Transplantation*, vol. 32, no. 9, pp. 1487–1492, 2017.
- [16] C. P. Larsen, P. J. Morris, and J. M. Austyn, "Migration of dendritic leukocytes from cardiac allografts into host spleens. A novel pathway for initiation of rejection," *Journal of Experimental Medicine*, vol. 171, no. 1, pp. 307–314, 1990.
- [17] V. Nicleleit and K. Andreoni, "Inflammatory cells in renal allografts," *Frontiers in Bioscience*, vol. 13, pp. 6202–13, 2008.
- [18] R. L. Dedrick, S. Bodary, and M. R. Garovoy, "Adhesion molecules as therapeutic targets for autoimmune diseases and transplant rejection," *Expert Opinion on Biological Therapy*, vol. 3, no. 1, pp. 85–95, 2003.

- [19] M. Barry and R. C. Bleackley, "Cytotoxic T lymphocytes: all roads lead to death," *Nature Reviews Immunology*, vol. 2, no. 6, pp. 401–409, 2002.
- [20] E. Inquilli, "Mechanism of cellular rejection in transplantation," *Pediatric Nephrology*, vol. 25, no. 1, pp. 61–74, 2010.
- [21] M. Mengel, B. Sis, and P. F. Halloran, "SWOT analysis of Banff: strengths, weaknesses, opportunities and threats of the international Banff consensus process and classification system for renal allograft pathology," *American Journal of Transplantation*, vol. 7, no. 10, pp. 2221–2226, 2007.
- [22] M. Naesens, L. Heylen, E. Lerut et al., "Intrarenal resistive index after renal transplantation," *New England Journal of Medicine*, vol. 369, no. 19, pp. 1797–1806, 2013.
- [23] J. Radermacher, M. Mengel, S. Ellis et al., "The renal arterial resistance index and renal allograft survival," *New England Journal of Medicine*, vol. 349, no. 2, pp. 115–124, 2003.
- [24] R. Kramann, D. Frank, V. M. Brandenburg et al., "Prognostic impact of renal arterial resistance index upon renal allograft survival: the time point matters," *Nephrology Dialysis Transplantation*, vol. 27, no. 10, pp. 3958–3963, 2012.
- [25] Y. Jin, C. Yang, S. Wu et al., "A novel simple noninvasive index to predict renal transplant acute rejection by contrast-enhanced ultrasonography," *Transplantation*, vol. 99, no. 3, pp. 636–641, 2015.
- [26] K. Mueller-Peltzer, G. Negrão de Figueiredo, M. Fischereder, A. Habicht, J. Rübenthaler, and D. A. Clevert, "Vascular rejection in renal transplant: diagnostic value of contrast-enhanced ultrasound (CEUS) compared to biopsy," *Clinical Hemorheology and Microcirculation*, vol. 69, no. 1–2, pp. 77–82, 2018.
- [27] A. Grabner, D. Kentrup, M. Muhlmeister et al., "Noninvasive imaging of acute renal allograft rejection by ultrasound detection of microbubbles targeted to T-lymphocytes in rats," *Ultraschall in der Medizin—European Journal of Ultrasound*, vol. 37, no. 1, pp. 82–91, 2016.
- [28] G. Thölking, K. Schuette-Nuetgen, D. Kentrup, H. Pawelski, and S. Reuter, "Imaging-based diagnosis of acute renal allograft rejection," *World Journal of Transplantation*, vol. 6, no. 1, pp. 174–82, 2016.
- [29] T. Liao, Y. Zhang, J. Ren et al., "Noninvasive quantification of intrarenal allograft C4d deposition with targeted ultrasound imaging," *American Journal of Transplantation*, vol. 19, no. 1, pp. 259–268, 2019.
- [30] J. Sellarés, D. G. de Freitas, M. Mengel et al., "Understanding the causes of kidney transplant failure: the dominant role of antibody-mediated rejection and nonadherence," *American Journal of Transplantation*, vol. 12, no. 2, pp. 388–399, 2012.
- [31] M. Meier, L. Fricke, K. Eikenbusch et al., "The serial duplex index improves differential diagnosis of acute renal transplant dysfunction," *Journal of Ultrasound in Medicine*, vol. 36, no. 8, pp. 1607–1615, 2017.
- [32] M. Cicoira, L. Conte, A. Rossi et al., "Renal arterial pulsatility predicts progression of chronic kidney disease in chronic heart failure patients," *International Journal of Cardiology*, vol. 167, no. 6, pp. 3050–3051, 2013.
- [33] C. Jiménez, M. O. López, A. Ros et al., "The natural history of kidney graft cortical microcirculation determined by real-time contrast-enhanced microcirculation (RT-CES)," *PLoS One*, vol. 11, no. 3, Article ID e0150384, 2016.
- [34] C. McArthur and G. M. Baxter, "Current and potential renal applications of contrast-enhanced ultrasound," *Clinical Radiology*, vol. 67, no. 9, pp. 909–922, 2012.
- [35] C. Yang, Y. Jin, S. Wu et al., "Prediction of renal allograft acute rejection using a novel non-invasive model based on acoustic radiation force impulse," *Ultrasound in Medicine & Biology*, vol. 42, no. 9, pp. 2167–2179, 2016.
- [36] G. Ferraioli, P. Parekh, A. B. Levitov, and C. Filice, "Shear wave elastography for evaluation of liver fibrosis," *Journal of Ultrasound in Medicine*, vol. 33, no. 2, pp. 197–203, 2014.
- [37] N. P. Ghonge, M. Mohan, V. Kashyap, and S. Jasuja, "Renal allograft dysfunction: evaluation with shear-wave sonoelastography," *Radiology*, vol. 288, no. 1, pp. 146–152, 2018.
- [38] B. J. Kim, C. K. Kim, and J. J. Park, "Non-invasive evaluation of stable renal allograft function using point shear-wave elastography," *British Journal of Radiology*, vol. 91, no. 1081, article 20170372, 2018.
- [39] H. Early, J. Aguilera, E. Cheang, and J. McGahan, "Challenges and considerations when using shear wave elastography to evaluate the transplanted kidney, with pictorial review," *Journal of Ultrasound in Medicine*, vol. 36, no. 9, pp. 1771–1782, 2017.
- [40] M. R. Selzo, C. J. Moore, M. M. Hossain, M. L. Palmeri, and C. M. Gallippi, "On the quantitative potential of viscoelastic response (VisR) ultrasound using the one-dimensional mass-spring-damper model," *IEEE Transactions on Ultrasonics, Ferroelectrics, and Frequency Control*, vol. 63, no. 9, pp. 1276–1287, 2016.
- [41] M. M. Hossain, M. R. Selzo, R. M. Hinson et al., "Evaluating renal transplant status using viscoelastic response (VisR) ultrasound," *Ultrasound in Medicine & Biology*, vol. 44, no. 8, pp. 1573–1584, 2018.
- [42] J. L. Zhang, G. Morrell, H. Rusinek et al., "New magnetic resonance imaging methods in nephrology," *Kidney International*, vol. 85, no. 4, pp. 768–778, 2014.
- [43] B. Kalb, D. R. Martin, K. Salman, P. Sharma, J. Votaw, and C. Larsen, "Kidney transplantation: structural and functional evaluation using MR nephro-urography," *Journal of Magnetic Resonance Imaging*, vol. 28, no. 4, pp. 805–822, 2008.
- [44] F. Khalifa, M. Abou El-Ghar, B. Abdollahi, H. B. Frieboes, T. El-Diasty, and A. El-Baz, "A comprehensive non-invasive framework for automated evaluation of acute renal transplant rejection using DCE-MRI," *NMR in Biomedicine*, vol. 26, no. 11, pp. 1460–1470, 2013.
- [45] F. Khalifa, A. El-Baz, G. Gimel'farb, and M. A. El-Ghar, "Non-invasive image-based approach for early detection of acute renal rejection," in *Medical Image Computing and Computer-Assisted Intervention—MICCAI 2010*, vol. 6361, no. 1, pp. 10–18, Springer, Berlin, Germany, 2010.
- [46] M. Onniboni, M. De Filippo, R. Averna et al., "Magnetic resonance imaging in the complications of kidney transplantation," *La Radiologia Medica*, vol. 118, no. 5, pp. 837–850, 2013.
- [47] A. Yamamoto, J. L. Zhang, H. Rusinek et al., "Quantitative evaluation of acute renal transplant dysfunction with low-dose three-dimensional MR renography," *Radiology*, vol. 260, no. 3, pp. 781–789, 2011.
- [48] A. L. Wentland, E. A. Sadowski, A. Djamali, T. M. Grist, B. N. Becker, and S. B. Fain, "Quantitative MR measures of intrarenal perfusion in the assessment of transplanted kidneys: initial experience," *Academic Radiology*, vol. 16, no. 9, pp. 1077–1085, 2009.
- [49] L. Daftari Besheli, S. Aran, K. Shaqdan, J. Kay, and H. Abujudeh, "Current status of nephrogenic systemic fibrosis," *Clinical Radiology*, vol. 69, no. 7, pp. 661–668, 2014.
- [50] R. J. McDonald, J. S. McDonald, D. F. Kallmes et al., "Intracranial gadolinium deposition after contrast-enhanced MR imaging," *Radiology*, vol. 275, no. 3, pp. 772–782, 2015.

- [51] E. C. Wong, "An introduction to ASL labeling techniques," *Journal of Magnetic Resonance Imaging*, vol. 40, no. 1, pp. 1–10, 2014.
- [52] E. T. Petersen, I. Zimine, Y.-C. L. Ho, and X. Golay, "Non-invasive measurement of perfusion: a critical review of arterial spin labelling techniques," *British Journal of Radiology*, vol. 79, no. 944, pp. 688–701, 2006.
- [53] N. S. Artz, E. A. Sadowski, A. L. Wentland et al., "Arterial spin labeling MRI for assessment of perfusion in native and transplanted kidneys," *Magnetic Resonance Imaging*, vol. 29, no. 1, pp. 74–82, 2011.
- [54] R. S. Lanzman, H.-J. Wittsack, P. Martirosian et al., "Quantification of renal allograft perfusion using arterial spin labeling MRI: initial results," *European Radiology*, vol. 20, no. 6, pp. 1485–1491, 2010.
- [55] E. A. Sadowski, A. Djamali, A. L. Wentland et al., "Blood oxygen level-dependent and perfusion magnetic resonance imaging: detecting differences in oxygen bioavailability and blood flow in transplanted kidneys," *Magnetic Resonance Imaging*, vol. 28, no. 1, pp. 56–64, 2010.
- [56] S. Y. Park, C. K. Kim, B. K. Park, W. Huh, S. J. Kim, and B. Kim, "Evaluation of transplanted kidneys using blood oxygenation level-dependent MRI at 3 T: a preliminary study," *American Journal of Roentgenology*, vol. 198, no. 5, pp. 1108–1114, 2012.
- [57] G. Liu, F. Han, W. Xiao, Q. Wang, Y. Xu, and J. Chen, "Detection of renal allograft rejection using blood oxygen level-dependent and diffusion weighted magnetic resonance imaging: a retrospective study," *BMC Nephrology*, vol. 15, no. 1, p. 158, 2014.
- [58] W. Xiao, J. Xu, Q. Wang, Y. Xu, and M. Zhang, "Functional evaluation of transplanted kidneys in normal function and acute rejection using BOLD MR imaging," *European Journal of Radiology*, vol. 81, no. 5, pp. 838–845, 2012.
- [59] F. H. Epstein, Y. Agmon, and M. Brezis, "Physiology of renal hypoxia," *Annals of the New York Academy of Sciences*, vol. 718, pp. 72–81, 1994.
- [60] V. Baliyan, C. J. Das, R. Sharma, and A. K. Gupta, "Diffusion weighted imaging: technique and applications," *World Journal of Radiology*, vol. 8, no. 9, pp. 785–98, 2016.
- [61] E. Hollis, M. Shehata, M. Abou El-Ghar et al., "Statistical analysis of ADCs and clinical biomarkers in detecting acute renal transplant rejection," *British Journal of Radiology*, vol. 90, no. 1080, article 20170125, 2017.
- [62] K. Hueper, M. Gutberlet, J. H. Bräsen et al., "Multiparametric Functional MRI: non-Invasive imaging of inflammation and edema formation after kidney transplantation in mice," *PLoS One*, vol. 11, no. 9, Article ID e0162705, 2016.
- [63] R. S. Lanzman, A. Ljimani, G. Pentang et al., "Kidney transplant: functional assessment with diffusion-tensor MR imaging at 3T," *Radiology*, vol. 266, no. 1, pp. 218–225, 2013.
- [64] E. Deger, A. Celik, H. Dheir et al., "Rejection evaluation after renal transplantation using MR diffusion tensor imaging," *Acta Radiologica*, vol. 59, no. 7, pp. 876–883, 2018.
- [65] J. M. Thurman and N. J. Serkova, "Nanosized contrast agents to noninvasively detect kidney inflammation by magnetic resonance imaging," *Advances in Chronic Kidney Disease*, vol. 20, no. 6, pp. 488–499, 2013.
- [66] O. Hauger, N. Grenier, C. Deminère et al., "USPIO-enhanced MR imaging of macrophage infiltration in native and transplanted kidneys: initial results in humans," *European Radiology*, vol. 17, no. 11, pp. 2898–2907, 2007.
- [67] E. Y. Chae, E. J. Song, J. Y. Sohn et al., "Allogeneic renal graft rejection in a rat model: in vivo MR imaging of the homing trait of macrophages," *Radiology*, vol. 256, no. 3, pp. 847–854, 2010.
- [68] L. Liu, Q. Ye, Y. Wu et al., "Tracking T-cells in vivo with a new nano-sized MRI contrast agent," *Nanomedicine: Nanotechnology, Biology and Medicine*, vol. 8, no. 8, pp. 1345–1354, 2012.
- [69] N. N. Yada, J. Xu, A. Bar-Shir et al., "Natural D-glucose as a biodegradable MRI relaxation agent," *Magnetic Resonance in Medicine*, vol. 72, no. 3, pp. 823–828, 2014.
- [70] D. Kentrup, P. Bovenkamp, A. Busch et al., "GlucoCEST magnetic resonance imaging in vivo may be diagnostic of acute renal allograft rejection," *Kidney International*, vol. 92, no. 3, pp. 757–764, 2017.
- [71] X. Xu, N. N. Yadav, L. Knutsson et al., "Dynamic glucose-enhanced (DGE) MRI: translation to human scanning and first results in glioma patients," *Tomography*, vol. 1, no. 2, pp. 105–114, 2015.

## Research Article

# Comparative Evaluation of $^{68}\text{Ga}$ -Citrate PET/CT and $^{18}\text{F}$ -FDG PET/CT in the Diagnosis of Type II Collagen-Induced Arthritis in Rats

Zi Wang <sup>1</sup>, Liang Cai,<sup>1,2</sup> Tingting Xu,<sup>1</sup> Dan Tang,<sup>3</sup> Lin Liu,<sup>1</sup> and Yue Chen <sup>1</sup>

<sup>1</sup>Department of Nuclear Medicine, Affiliated Hospital of Southwest Medical University,

Nuclear Medicine and Molecular Imaging Key Laboratory of Sichuan Province, Luzhou, Sichuan, China

<sup>2</sup>State Key Laboratory for Quality Research of Chinese Medicines, Macau University of Science and Technology, Taipa, Macau

<sup>3</sup>Department of Pathology, Affiliated Hospital of Southwest Medical University, Luzhou, Sichuan, China

Correspondence should be addressed to Yue Chen; [chenyue5523@126.com](mailto:chenyue5523@126.com)

Received 29 January 2019; Accepted 27 February 2019; Published 19 March 2019

Academic Editor: Anne Roivainen

Copyright © 2019 Zi Wang et al. This is an open access article distributed under the Creative Commons Attribution License, which permits unrestricted use, distribution, and reproduction in any medium, provided the original work is properly cited.

Rheumatoid arthritis (RA) is a chronic autoimmune disease characterized by systemic, symmetrical, and erosive synovitis. RA is one of the most common disabling diseases in the clinic. The main clinical intervention strategies are early diagnosis and early treatment. This study aims to predict the diagnostic value of  $^{68}\text{Ga}$ -citrate and  $^{18}\text{F}$ -FDG PET/CT in RA by comparing and analyzing the value of  $^{68}\text{Ga}$ -citrate and  $^{18}\text{F}$ -FDG PET/CT for diagnosing type II collagen-induced arthritis (CIA) in rats. Some CIA models were established. Normal rats were selected as the control group, and 23 days and 40 days were selected as the early and late time points of arthritis, respectively. The semiquantitative analysis of CIA rats was carried out with  $^{68}\text{Ga}$ -citrate PET/CT and  $^{18}\text{F}$ -FDG PET/CT, and the ratio of the maximum standardized uptake ( $\text{SUV}_{\text{max}}$ ) values in the regions of interest (ROIs) of the hind foot ankle joint and thigh muscle was calculated and statistically analyzed. The distribution of CIA rats in vivo at the  $^{68}\text{Ga}$ -citrate 90 min time point was studied, and the ankle tissues were evaluated with hematoxylin and eosin (HE) staining.  $^{68}\text{Ga}$ -citrate PET/CT is obviously superior to  $^{18}\text{F}$ -FDG PET/CT for CIA imaging, and the statistical results show that the difference between the two examination methods is statistically significant ( $P < 0.001$ ). The uptake of these two radiopharmaceuticals showed the same trend in arthritis rats with different scores. The distribution of  $^{68}\text{Ga}$ -citrate at 90 min is consistent with the trend shown by  $^{68}\text{Ga}$ -citrate PET/CT.  $^{68}\text{Ga}$ -citrate PET/CT can reflect the inflammatory activity of affected joints in CIA rats earlier and more sensitively than  $^{18}\text{F}$ -FDG PET/CT, and this imaging advantage continues until the later stage of inflammation. Therefore,  $^{68}\text{Ga}$ -citrate PET/CT is worthy of further promotion and application in the clinical diagnosis of RA.

## 1. Introduction

Rheumatoid arthritis (RA) is a chronic autoimmune disease characterized by systemic, symmetrical, and aggressive synovitis [1]. RA has an insidious onset and is recurrent and persistent. In patients with RA, the affected joints show redness, heat, and pain in the early stages of the disease. In the late stages of the disease, there are different degrees of joint deformity and associated atrophy of bones and muscles. Irreversible joint damage eventually leads to disability. RA is one of the most common disabling diseases in the clinic. The etiology and pathogenesis of RA are not fully

understood and may be related to genetic, environmental, and immune abnormalities. The clinical intervention strategy for RA is early diagnosis and treatment. The timely and accurate diagnosis of RA is of great clinical significance for relieving the clinical symptoms of the disease and reducing the disability rate.

Laboratory evaluation of RA patients involves several biological parameters, including rheumatoid factor, C-reactive protein (CRP), matrix metalloproteinase-3 (MMP-3), and erythrocyte sedimentation rate (ESR) [2]. However, these biological parameters do not accurately reflect the activity of the disease. Magnetic resonance imaging (MRI)

and ultrasound have been used to detect synovitis early in RA [3, 4]. Unfortunately, MRI is often limited to a single joint, and the use of MRI for total body joint imaging is impractical; furthermore, ultrasound is largely dependent on the physician's experience.

Bone scintigraphy is also a routine imaging method used to evaluate RA, but this modality is not sensitive enough to detect synovitis [5]. Positron emission tomography/computed tomography (PET/CT) has higher resolution and can better distinguish bone and soft tissue structures than other imaging modalities.  $^{18}\text{F}$ -FDG PET/CT can accurately reflect glucose metabolism levels in organs and tissues. This imaging modality has become a powerful imaging technology recognized in oncology. This imaging technology can also be used to evaluate inflammatory diseases, such as RA [6, 7].

$^{67}\text{Ga}$ -citrate is a classic radiopharmaceutical for inflammatory imaging and has been widely used in the clinic [8].  $^{68}\text{Ga}$  is an isotope of  $^{67}\text{Ga}$  and has similar physical and chemical properties to  $^{67}\text{Ga}$ . As a positron nuclide,  $^{68}\text{Ga}$  can be combined with PET/CT technology to obtain high-resolution images. The half-life of  $^{68}\text{Ga}$  (68 min) is significantly lower than that of  $^{67}\text{Ga}$  (78.3 h), so  $^{68}\text{Ga}$ -labeled compounds can significantly reduce the radiation dose to patients and staff. In addition,  $^{68}\text{Ga}$  is obtained by a  $^{68}\text{Ge}/^{68}\text{Ga}$  generator [9], which is convenient and quick to obtain, and the cost is obviously lower than that of  $^{67}\text{Ga}$  and  $^{18}\text{F}$  produced by an accelerator. Therefore, PET/CT imaging with  $^{68}\text{Ga}$ -labeled citrate has considerable social and economic benefits. This paper aims to compare the value of  $^{68}\text{Ga}$ -citrate and  $^{18}\text{F}$ -FDG PET/CT for evaluating collagen-induced arthritis (CIA) in rats.

## 2. Materials and Methods

**2.1. Materials.** An  $\text{itG } ^{68}\text{Ge}/^{68}\text{Ga}$  generator was purchased from China Isotope and Radiation Corporation.  $^{18}\text{F}$ -FDG was produced and synthesized by the Department of Nuclear Medicine, Affiliated Hospital of Southwest Medical University; its radiochemical purity (RCP) was over 99%. High-purity chick type II collagen was purchased from Chondrex, USA, and incomplete Freund's adjuvant was purchased from Sigma, USA. Isoflurane was purchased from Hebei Yipin Pharmaceutical Co., Ltd., China, and its chemical formula is  $\text{C}_3\text{H}_2\text{ClF}_5\text{O}$ . All other chemicals involved are reagent-grade materials purchased from Aladdin Bio-Chem Technology, Shanghai, China. Xinhua No. 1 chromatography paper used for paper chromatography (PC) was purchased from Hangzhou Xinhua Paper Co., Ltd. Rat ankle joint data acquisition was performed with a micro-PET/CT scanner (SIEMENS Inveon<sup>TM</sup>, Munich, Germany). The radioactivity of the samples was measured using a  $\gamma$  counter (SN-695B; Hesuo Rihuan Photoelectric Instrument Co., Shanghai, China) and a calibrator (CRC-15R; Capintec Inc., Florham Park, NJ, USA). Seven-week-old healthy and clean female Sprague-Dawley (SD) rats were provided by the Animal Experimental Center of Southwestern Medical University (Animal License SCXK 2013-17) and weighed  $147 \text{ g} \pm 12 \text{ g}$ .

**2.2. Animal Models.** The CIA model has been widely used as a model for human RA because of its common pathological and immunological characteristics. The specific operation for establishing CIA rat models is as follows: 10 mg of chick type II collagen fiber was dissolved in 5 ml of 0.1 mol/L acetic acid and mixed evenly so that the concentration of the mixed solution is 2 mg/ml. This mixture was then stored at 4°C for one night. The next day, 0.7 ml of collagen fiber was aspirated with a 2 ml syringe, and 0.7 ml of incomplete Freund's adjuvant was aspirated with another 2 ml syringe. The needles were removed from both syringes taken, at the same time, the three-way stopcock was connected to an ice bag, and the knob of the three-way stopcock was adjusted to allow the two syringes to communicate at a right angle; thus, the remaining interface was closed. The syringes were pushed back and forth on the ice bag for 30 min so that the solutions in the two syringes were fully mixed into a milky white substance. If the resultant emulsion cannot be dispersed when immersed into clear water, the preparation of 1 mg/ml collagen emulsion can be considered complete. The prepared female SD rats were anesthetized with isoflurane gas (3% concentration, oxygen flow rate 0.6 L/min), and the anesthesia was considered successful when the muscular tension of the rats disappeared. The collagen emulsion (0.1 ml) was injected subcutaneously at a distance of 2-3 cm from the tail root of the rats, and a total of 12 rats were immunized. One week after the initial immunization, the same dose of collagen emulsion was injected into the same area in these rats again.

Beginning on the day of the second immunization, rats were examined clinically every other day to assess the severity of paw arthritis. The arthritis index (AI) score of the paw of model rats is as follows: score 0 = no macroscopic evidence of erythema and swelling; score 1 = erythema and mild soft tissue swelling limited to the tarsus/ankle joint; score 2 = erythema and mild soft tissue swelling extending from the ankle joint to the tarsus; score 3 = erythema and moderate soft tissue swelling extending from the ankle joint to the tarsus; score 4 = obvious erythema and severe swelling (including ankle joint, plantar surface, and toe) or ankylosis of the limbs.

**2.3. Preparation and Quality Control of  $^{68}\text{Ga}$ -Citrate.** Preparation of  $^{68}\text{Ga}$ -citrate: A  $^{68}\text{Ge}/^{68}\text{Ga}$  generator with a specification of 20 mCi was rinsed with 0.05 M HCl to yield 5 ml of  $^{68}\text{Ga}^{3+}$  solution for radioactive labeling. During rinsing, the  $^{68}\text{Ga}^{3+}$  solution was split into 5 EP (2 ml) tubes in sequence so that each EP tube contained 1 ml of solution. The third tube with the highest activity (about 7 mCi  $^{68}\text{Ga}^{3+}$ ) was obtained and 43 mg of citrate solid was added, followed by agitation and reaction in a 60°C water bath for 10-15 min. The pH was adjusted to 4-5, and the solution was filtered through a 0.22  $\mu\text{m}$  filter membrane to obtain the final solution. The quality of  $^{68}\text{Ga}$ -citrate and  $^{68}\text{Ga}^{3+}$  solutions was determined with a PC bar. The origin was marked 2 cm from one end of Xinhua No. 1 paper with a pencil, and 2-4  $\mu\text{l}$  of the final solution was applied at the origin. Finally, a mixture of  $\text{NH}_4\text{OH}$  (25.28%)/ $\text{CH}_3\text{OH}$  (100%)/ $\text{H}_2\text{O}$  (1 : 5 : 9.5 V/V/V)

was used as the elution solvent, and TLC technology was used to analyze the radiochemical purity of  $^{68}\text{Ga}$ -citrate.

**2.4. Stability Assessment of  $^{68}\text{Ga}$ -Citrate.** To evaluate the in vitro stability of  $^{68}\text{Ga}$ -citrate, TLC was used to analyze its quality at room temperature ( $22 \pm 3^\circ\text{C}$ ) at 30 min, 60 min, 90 min, 120 min, and 180 min after the final preparation was synthesized. To study the stability of the labeled preparation in human plasma, 0.1 ml of fresh healthy adult plasma was taken, approximately 300  $\mu\text{Ci}$  (approximately 0.08 ml)  $^{68}\text{Ga}$ -citrate was added, and the radiochemical purity of the labeled compound was determined by TLC after incubation at  $37.4^\circ\text{C}$  for 30 min, 60 min, 90 min, 120 min, and 180 min.

**2.5. Micro-PET/CT Imaging of CIA Rats and Normal Rats.** To evaluate the optimal imaging point for CIA rats injected with  $^{68}\text{Ga}$ -citrate, we selected two affected rats (scoring 1–3), anesthetized them with isoflurane gas (3% concentration, oxygen flow rate 0.6 L/min), weighed them rapidly, and then injected 0.1 ml of 150–300  $\mu\text{Ci}$   $^{68}\text{Ga}$ -citrate in isotonic saline through the tail vein. Under continuous gas anesthesia (1.5% concentration, oxygen flow rate 0.5 L/min), the animals were placed in the supine position for fixation. Micro-PET/CT was performed on the posterior bilateral ankle joints 10 min, 30 min, 60 min, 90 min, 120 min, 150 min, 180 min, and 210 min after injection, and the acquisition matrix size was  $128 \times 128$ . Each scan lasted for 10 min, and the acquired data were reconstructed as two-dimensional filtered back-projections (2D-FBPs). After the data collection was completed, the region of interest (ROI,  $\text{mm}^3$ ) of the lateral muscles of the ankle joint and ipsilateral hind leg was delineated with Inveon Research Workplace 4.2 software, and the maximum standardized uptake value ( $\text{SUV}_{\text{max}}$ ) was calculated to determine the ratio of the arthritis area (target ( $T$ ) area) to background (nontarget ( $\text{NT}$ ) area) ( $T/\text{NT}$ ).

Before performing imaging studies on all the arthritis rats, we selected 3 healthy female rats for  $^{68}\text{Ga}$ -citrate/ $^{18}\text{F}$ -FDG PET/CT imaging of the posterior ankle joint as a control group. These rats were weighed after anesthesia with isoflurane gas, and then 200  $\mu\text{Ci}$   $^{68}\text{Ga}$ -citrate/ $^{18}\text{F}$ -FDG in approximately 0.1 ml of isotonic saline was injected via the tail vein. The imaging time point in rats injected with  $^{68}\text{Ga}$ -citrate was the best time as determined above, while in rats injected with  $^{18}\text{F}$ -FDG, micro-PET/CT image acquisition was initiated at 60 min [10]. We usually performed  $^{68}\text{Ga}$ -citrate PET/CT examinations on rats in the morning on one day. After at least 5  $^{68}\text{Ga}$  half-lives, these rats were injected with  $^{18}\text{F}$ -FDG in the same way for imaging.

On the 23rd and 40th days after the first immunization, we collected micro-PET/CT data from the hind ankle joints of CIA model rats. Like the control rats,  $^{68}\text{Ga}$ -citrate PET/CT examinations were performed on these rats in the morning on one day. After at least 5 half-lives of  $^{68}\text{Ga}$ ,  $^{18}\text{F}$ -FDG was injected into these rats in the same way for imaging. Before all imaging experiments, rats were fasted, and access to water was restricted. After injecting radiopharmaceuticals, the rats were placed separately in small cages to avoid fighting and excessive exercise.

**2.6. Biodistribution in the CIA Rats.** The biodistribution of  $^{68}\text{Ga}$ -citrate in vivo at 90 min was evaluated in CIA model rats (weight range 153–176 g). Each rat was injected with 280–300  $\mu\text{Ci}$  of  $^{68}\text{Ga}$ -citrate in an equal volume of saline via the tail vein in a total volume of 0.1 ml. After 90 minutes, isoflurane (2% concentration, oxygen flow rate of 0.6 L/min) was administered for anesthesia, and 0.1 ml of blood was obtained through the tail vein. Then, 1 ml of air was injected through the tail vein to embolize the rat, and then the rat was quickly dissected. The heart, liver, spleen, lungs, kidneys, stomach, small intestines, muscles, skin, brain, and bilateral hind foot ankle joints of the rats were removed, washed with physiological saline and dried, placed in a test tube of known quality, and a  $\gamma$  counter and microbalance were used to measure the radiological counts and quality of these tissues and calculate the percentage of injected dose per gram of tissue (%ID/g).

**2.7. Histology.** After the biological distribution study was completed, the collected ankle tissues were routinely fixed in 10% neutral formalin. Then, these tissues were sent to the Pathology Department of the Affiliated Hospital of Southwest Medical University, where professional researchers completed decalcification, fixation, sectioning, hematoxylin-eosin (HE) staining, and microscopic observation of the pathological tissues of the ankle joints of the arthritis model rats.

**2.8. Statistical Analysis.** The  $T/\text{NT}$  ratio and biological distribution data were reported as  $\bar{X} \pm \text{SD}$ . The statistical significance of the 95% confidence level was determined by paired  $t$ -tests using SPSS statistics 17.0 software package, and the significance level was set to 0.001.

### 3. Results

**3.1. CIA Models.** On the 3rd day after the second immunization, one rat was found dead, and the other 11 rats showed no signs of deterioration in diet, defecation, or vitality. On the 15th day after the first immunization, one rat developed slight redness and swelling in the left hind foot ankle joint. As time progressed, the left and right ankle joints of several rats showed redness, swelling, and lameness, and the ankle joints of some rats showed explosive deterioration in 1–2 days. On day 23, 8 rats developed arthritis (AI score  $\geq 1$ ). On day 40, 10 rats developed arthritis. A total of 10 of the 11 surviving rats used to establish the CIA model successfully developed arthritis (90.9%).

**3.2. Synthesis and Stability of  $^{68}\text{Ga}$ -Citrate.** It is simple and convenient to synthesize  $^{68}\text{Ga}$ -citrate using readily available reagent-grade citrate and  $^{68}\text{Ga}^{3+}$  solution directly rinsed with our generator. The radiochemical purity and labeling rate were determined by PC and TLC.  $^{68}\text{Ga}^{3+}$  remains at the origin ( $R_f = 0$ ), while the labeling compound  $^{68}\text{Ga}$ -citrate moves to the front ( $R_f = 1$ ) under the same solvent conditions ( $\text{NH}_4\text{OH}/\text{CH}_3\text{OH}/\text{H}_2\text{O}$ ). The radiochemical purity of

$^{68}\text{Ga}$ -citrate has been proven to be over 99%, so it can meet the requirements for subsequent experiments and practical applications. The stability of the labeled compound measured at room temperature and in human plasma at  $37.4^\circ\text{C}$  shows that the *in vitro* labeling rate of  $^{68}\text{Ga}$ -citrate at 180 min is higher than 97%.

**3.3. Micro-PET/CT Image Analysis.** CIA rats were used to acquire  $^{68}\text{Ga}$ -citrate images at different time points. The  $\text{SUV}_{\text{max}}$  value of the ankle joint was measured by placing a 3D volume of interest around each paw. The middle lateral muscle of the tibia of rats was selected as the background; the volume of the 3D ROI of approximately  $2.5 \times 2.5 \times 2.5$  mm was drawn with analysis software to obtain the  $\text{SUV}_{\text{max}}$ . The  $\text{SUV}_{\text{max}}$  was measured at least 5 times, the highest and lowest  $\text{SUV}_{\text{max}}$  were removed, and the remaining values were used to calculate the average value to obtain the final  $\text{SUV}_{\text{max}}$  of the muscle background. Next, the  $\text{SUV}_{\text{max}}$  of the ankle joint was divided by the  $\text{SUV}_{\text{max}}$  of the muscle background for standardization, and finally, the ratio of the *T* area (ankle joint) and *NT* area (muscle) (*T/NT*) was obtained by calculation. Ten minutes after injection of  $^{68}\text{Ga}$ -citrate, CIA model rats had light uptake in the bilateral ankle joints. At 30 min, the uptake of the imaging agent increased gradually. At 90–120 min, the ratio of *T/NT* was basically stable, and the ratio did not change significantly with the acquisition time. However, the image quality gradually deteriorated after 150 min.

CIA onset in rats is similar to that in RA, and the disease process is gradual. The degree of redness and swelling of the bilateral paws of these rats was often inconsistent. Figure 1 shows that on the 23rd day, the AI score in the left paw of one rat was 2 points, while that in the right paw was 0 points. On PET/CT images,  $^{68}\text{Ga}$ -citrate showed high uptake in the left ankle joint ( $\text{SUV}_{\text{max}}$ , 2.2) but low uptake in the right ankle joint ( $\text{SUV}_{\text{max}}$ , 1). In  $^{18}\text{F}$ -FDG images, the left paw had low uptake of the imaging agent ( $\text{SUV}_{\text{max}}$ , 1.4), and the right ankle joint had low uptake ( $\text{SUV}_{\text{max}}$ , 0.96).

The ratio of *T/NT* calculated after the two imaging agents were administered to CIA rats and normal rats were compared (Figure 2). The ratio of ankle joint uptake in rats with successfully induced arthritis (score 1–4) was significantly higher than that in normal rats. At 23 and 40 days, the uptake of the two imaging agents in the ankle joints of arthritic rats followed a general trend: score 4 > score 2 > score 3 > score 1. The *T/NT* ratio of  $^{68}\text{Ga}$ -citrate was always higher than that of  $^{18}\text{F}$ -FDG for rats with the same scores on 23 or 40 days. For rats with the same scores, the *T/NT* ratio of the two imaging agents at 23 days was always higher than that at 40 days.

The *T/NT* ratios of these 11 arthritic rats were statistically analyzed (Table 1). On the 23rd day, the *T/NT* ratio for  $^{68}\text{Ga}$ -citrate imaging ( $6.34 \pm 2.70$ ) in arthritic rats was 1.626 (95% CI: 1.128–2.124), which was higher than that for  $^{18}\text{F}$ -FDG imaging ( $4.71 \pm 1.77$ ); the difference was statistically significant ( $t(21) = 6.795$ ,  $P < 0.001$ ). On the 40th day, the *T/NT* ratio for  $^{68}\text{Ga}$ -citrate imaging ( $5.14 \pm 2.10$ ) was 1.992 (95% CI: 1.462–2.522), which was higher than that for  $^{18}\text{F}$ -FDG

imaging ( $3.15 \pm 1.26$ ); the difference was statistically significant ( $t(21) = 7.819$ ,  $P < 0.001$ ). We believe that  $^{68}\text{Ga}$ -citrate is better than  $^{18}\text{F}$ -FDG for imaging of CIA rats with micro-PET/CT.

**3.4. Biodistribution.** The biological distribution of  $^{68}\text{Ga}$ -citrate in arthritic rats was studied. Figure 3 summarizes the data of %ID/g at 90 min. The evaluation of arthritic ankles followed a general trend: score 4 ( $5.88 \pm 0.90\%$ ID/g) > score 2 ( $4.88 \pm 0.77\%$ ID/g) > score 3 ( $3.92 \pm 0.86\%$ ID/g) > score 1 ( $3.61 \pm 0.59\%$ ID/g) > score 0 ( $2.84 \pm 0.53\%$ ID/g). These data are consistent with the PET/CT images obtained above: the highest uptake was scored 4, and the lowest uptake was scored 0. Blood uptake was the highest ( $23.03 \pm 1.04\%$ ID/g) 90 min after  $^{68}\text{Ga}$ -citrate injection. The next highest uptake occurred in the lungs ( $10.27 \pm 1.44\%$ ID/g) and liver ( $7.89 \pm 0.82\%$ ID/g). As the main aggregation site of transferrin, the liver also showed significant uptake. The stomach ( $3.30 \pm 1.40\%$ ID/g), small intestine ( $3.70 \pm 1.73\%$ ID/g), and kidneys ( $5.62 \pm 1.10\%$ ID/g) all also showed uptake, indicating that the tracer could be excreted both through the digestive and urinary tracts.

**3.5. Histology.** For HE staining of tissues, the ankle tissues of CIA rats fixed in 10% neutral formalin solution were removed, decalcified in 10% formic acid-formaldehyde solution, and dehydrated in 50–100% gradient ethanol. Then, these tissues were immersed in a mixed solution of 100% ethanol and xylene (1 : 1 V/V) and embedded in paraffin after becoming transparent. After embedding,  $4\ \mu\text{m}$  paraffin sections were prepared. These slices were dried in a dryer for 30–60 min, dewaxed with xylene for 5–10 min, and hydrated with gradient ethanol (100–75%). Next, HE was used in sequence. Finally, the tissues were dehydrated with gradient ethanol (75–100%), became transparent with the application of xylene, and were sealed with neutral gum. All sections were photographed at  $10 \times 10$  and  $10 \times 40$  magnification. Figure 4 shows a magnification of  $10 \times 10$  (Figure 4(a)) visible partial exudation of the joint cavity with a large number of neutrophils infiltrating the area, which is an indicative of suppurative inflammation; a magnification of  $10 \times 40$  (Figure 4(b)) shows visible neutrophils in the full field of view, with almost no visible lymphocytes and plasma cells.

## 4. Discussion

The CIA model was Trentham's first experimental arthritis model that was established in 1977 [11]. After a large number of experimental studies, the model has been recognized as a classic model for studying human RA. There are many similarities between pathological changes and symptoms of CIA rats and RA [12]. First, the clinical symptoms are symmetrical joint involvement and invasion of the distal joints of limbs. Second, the main pathological change is proliferative synovitis, which gradually develops from synovitis to pannus formation and begins with edge destruction, eventually leading to articular cartilage destruction and even bone destruction. Finally, CIA causes

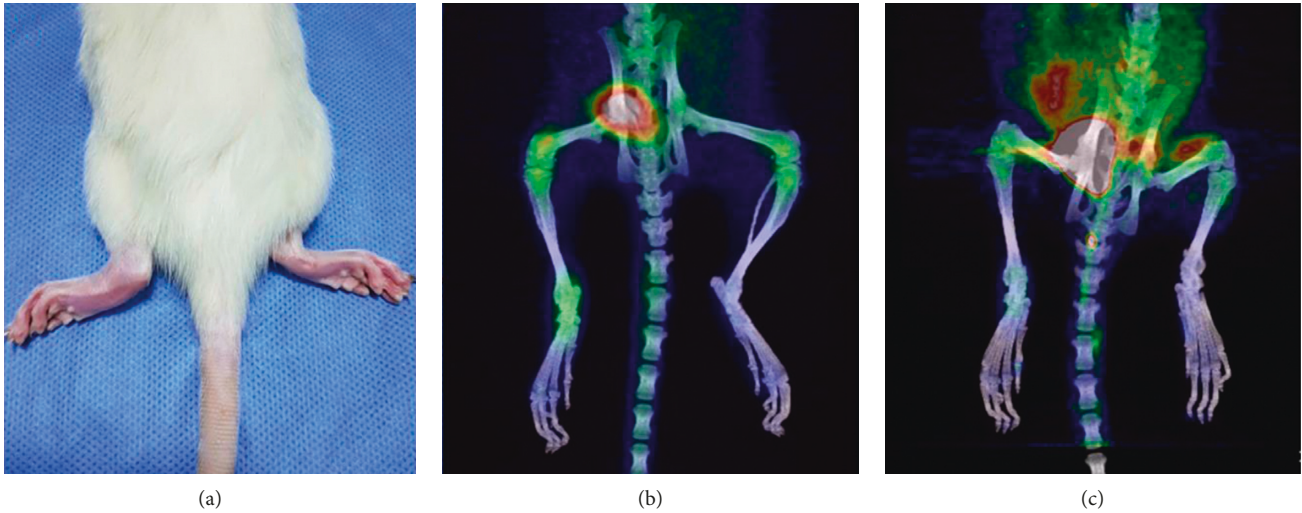


FIGURE 1: On the 23rd day, the AI score of one rat’s left paw was 2 and that of its right paw was 0. On PET/CT images,  $^{68}\text{Ga}$ -citrate showed high uptake in the left ankle joint ( $\text{SUV}_{\text{max}}, 2.2$ ) but low uptake in the right ankle joint ( $\text{SUV}_{\text{max}}, 1$ ). On  $^{18}\text{F}$ -FDG images, the left paw showed low uptake of the imaging agent ( $\text{SUV}_{\text{max}}, 1.4$ ), and the right ankle joint also showed low uptake ( $\text{SUV}_{\text{max}}, 0.96$ ).

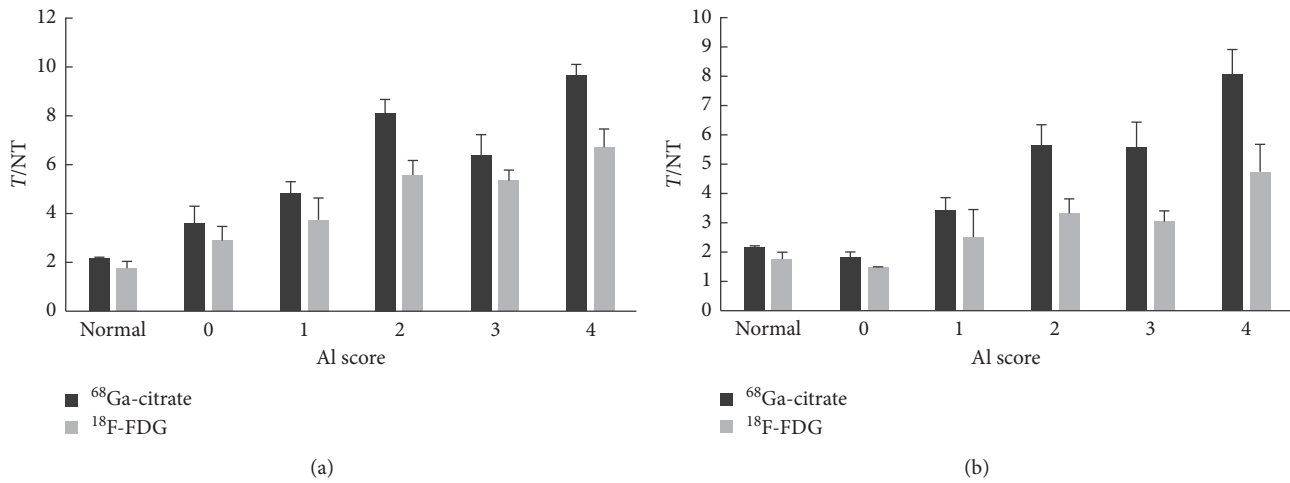


FIGURE 2: CIA rats were examined with  $^{68}\text{Ga}$ -citrate PET/CT and  $^{18}\text{F}$ -FDG PET/CT at 23 (a) and 40 days (b) after immunization to evaluate the ratio of the ankle joint (target area) to the muscle background (nontarget area) ( $T/NT$ ) of these rats. Normal rats were collected in advance as a control group.

TABLE 1: The  $T/NT$  of  $^{68}\text{Ga}$ -citrate and  $^{18}\text{F}$ -FDG in CIA rats.

	$N$	Day 23	Day 40
$^{68}\text{Ga}$ -citrate	22	$6.34 \pm 2.70$	$5.14 \pm 2.10$
$^{18}\text{F}$ -FDG	22	$4.71 \pm 1.77$	$3.15 \pm 1.26$
$t$		6.795	7.819
$P$		<0.001	<0.001

autoimmunity and is controlled by the major histocompatibility complex genes and related genes. The cellular and humoral immune changes are obvious. However, there are also some differences between CIA and human RA that cannot be ignored. First, the polymorphonuclear cells can be observed in the synovium of CIA rats in the early stage. However, in the early pathological changes of human RA,

although the synovium presents obvious hyperemia, edema, and synovial coating cells proliferation accompanied by plasma cells and lymphocyte infiltration, polymorphonuclear cells are abundant in synovial fluid and rare in synovium [13]. Second, CIA disease progresses rapidly and usually reaches the advanced stage within a few months, while human RA disease takes several years to progress [14].

The occurrence and development of CIA is a complex immune process that is jointly determined by T-cell-induced activation of the immune response, inflammatory factors, production of type II collagen antibody, and other links [14]. This model has typical signs of arthritis, and usually the ankle joint of the hind foot is the most frequently affected.

After immunization, joint involvement can occur as early as the 15th day in rats. Signs of early arthritis can be

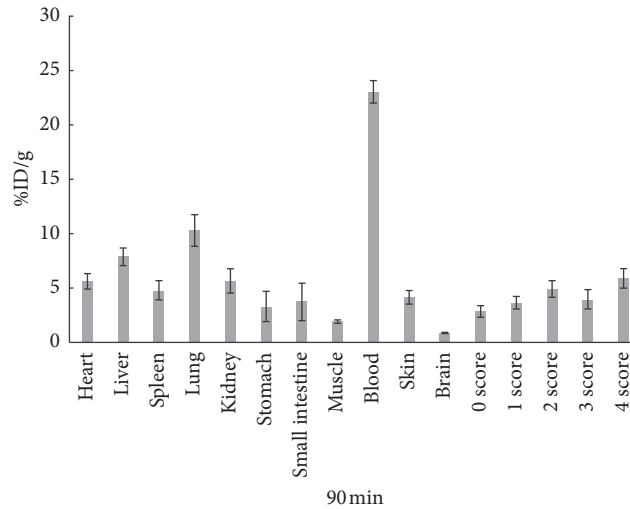


FIGURE 3: Distribution in vivo of arthritis in rats after injection of <sup>68</sup>Ga-citrate at 90 min.

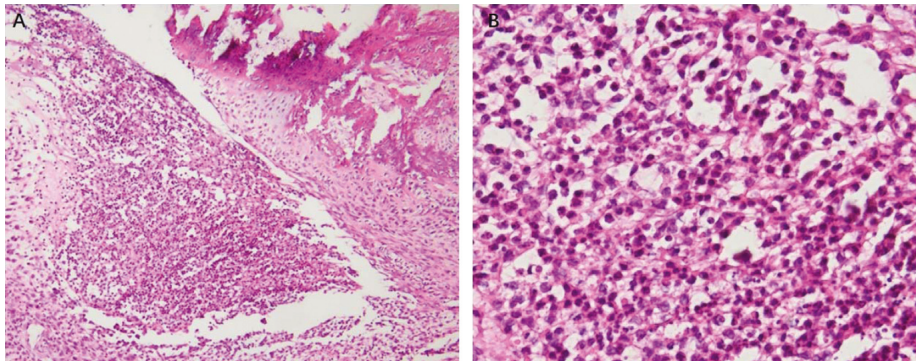


FIGURE 4: When the magnification is  $10 \times 10$  (a), some serous fluid in the joint cavity can be seen exuding, accompanied by a large number of neutrophils infiltrating the area, which is a manifestation of suppurative inflammation. When magnification is  $10 \times 40$  (b), neutrophils can be seen in the full field of vision, and lymphocytes and plasma cells are hardly visible.

observed with the naked eye at 21–28 days and include red and swollen joints, which can last for 5–8 weeks in general. We chose 23 days and 40 days as observation time points for early and late arthritis, respectively. The ankle joints of some rats that scored 0 at 23 days had microinflammation, but there was no obvious macroscopic evidence to prove the development of arthritis. In these rats, mild uptake of the imaging agent could be seen in the ankle joint with <sup>68</sup>Ga-citrate PET/CT, but little uptake was demonstrated <sup>18</sup>F-FDG PET/CT. Therefore, the *T/NT* ratio of rats with scores of 0 was higher than that of normal control rats. However, on the 40th day, there was only one rat with a score of 0. We think that this rat had not successfully developed arthritis. It is also understandable that the *T/NT* ratio of this rat was lower than that of normal control rats due to data scarcity for calculation. From 23 days to 40 days, although clinical arthritis gradually deteriorated, acute inflammatory manifestations, such as redness, swelling, and increased skin temperature, gradually decreased, and the macroscopic manifestations of arthritis were mainly joint rigidity and deformity. This situation was reflected in the uptake of <sup>68</sup>Ga-citrate and <sup>18</sup>F-FDG. The uptake of rats with scores of 0–4 at 23 days was

higher than that of rats with a score of 40 days. However, the two PET/CT imaging results showed that the uptake of rats with scores of 3 was lower than that of rats with scores of 2. We tried to explain this finding by HE staining; unfortunately, we do not have a reasonable explanation for this finding. Further experiments are necessary to analyze the reasons for this finding. However, the uptake of <sup>68</sup>Ga-citrate was significantly higher than that of <sup>18</sup>F-FDG in arthritic rats with each score, at both 23 and 40 days. Therefore, we think that <sup>68</sup>Ga-citrate is more valuable for arthritis imaging than <sup>18</sup>F-FDG. We recommend the use of <sup>68</sup>Ga-citrate PET/CT in the diagnosis of early RA, which may provide meaningful help for the early clinical treatment of patients.

A report has studied the distribution data of <sup>68</sup>Ga-citrate in normal rats at different time points (15 min, 30 min, 45 min, 60 min, and 120 min). In that study, blood always showed high uptake, which is consistent with our research results. It is possible that the high uptake is caused by the abundant transferrin in blood. However, the trend of uptake of some organs in that study is inconsistent with our research data. The reason for this difference may be that CIA is a systemic immune disease that may cause damage to

multiple organs or tissues. According to the severity of arthritis, the degree of damage to each organ is also different. The ankle joint tissues of the hind feet that we used for determination included bone and muscle tissue, and some of the bony tissue may not have been eroded by inflammatory cells, which may have decreased the %ID/g of the final arthritis tissue samples.

The pathology of the ankle joint observed in CIA model rats is similar to that observed in RA. Neovascularization in the synovium can be observed in the early stages [15]. Abundant blood flow may be the main reason for the increased uptake of  $^{68}\text{Ga}$ -citrate. These abundant blood vessels supply oxygen to the synovium and release inflammatory factors, causing the synovial tissue to begin to show the characteristics of hyperplasia and hypertrophy, eventually leading to the formation of pannus, erosion of the synovium, and damage to the cartilage and bone [13]. In the later stages of the disease, HE staining showed that there was fibrous tissue and exudative inflammatory cells in the synovial tissue. The medullary cavity of the joint disappeared, the cartilage surface collapsed, a large amount of granulation tissue and fibrous connective tissue filled in, and the bone and cartilage were damaged to varying degrees.

There are some limitations in this study. First, we have a small number of CIA samples; only 10 rats successfully developed arthritis. And the size of the micro-PET/CT acquisition matrix used at our institution was only  $128 \times 128$ , which made it impossible to acquire data on the forelimb joints of rats or to semiquantitatively evaluate metabolic changes in the internal organs of rats. Thus, the data from arthritic rats semiquantitatively analyzed by PET/CT may deviate from the real situation. Second, our research results support our recommendation to use  $^{68}\text{Ga}$ -citrate PET/CT to detect human RA. However, due to the high cost of PET/CT, this examination may be difficult to promote in some institutions that are not equipped with PET/CT.

## 5. Conclusion

In summary, in this study,  $^{68}\text{Ga}$ -citrate PET/CT was shown to reflect the inflammatory activity of affected joints in CIA rats earlier and more sensitively than  $^{18}\text{F}$ -FDG PET/CT, and this imaging advantage continues to the late stage of inflammation.  $^{68}\text{Ga}$ -citrate PET/CT may be helpful in detecting early RA, enabling RA patients to receive early clinical intervention, relieving their clinical symptoms, and reducing the disability rate. This examination method is worthy of clinical promotion and use.

## Abbreviations

RA:	Rheumatoid arthritis
CIA:	Type II collagen-induced arthritis
$^{18}\text{F}$ -FDG:	2-Deoxy-2-[ $^{18}\text{F}$ ]-fluoro-D-glucose
PET/CT:	Positron emission tomography/computed tomography
$\text{SUV}_{\text{max}}$ :	Maximum standardized uptake value
ROI:	Region of interest
HE:	Hematoxylin and eosin staining

AI:	Arthritis Index
MRI:	Magnetic resonance imaging.

## Data Availability

The data of this study are already presented in this paper.

## Ethical Approval

All studies were approved by the Ethics Committee of Southwestern Medical University.

## Conflicts of Interest

The authors declare that they have no conflicts of interest.

## Authors' Contributions

Zi Wang designed and carried out the whole experiment and drafted the manuscript. Liang Cai and Zi Wang established the CIA rat model together. Tingting Xu helped in the labeling of  $^{68}\text{Ga}$ -citrate. Dan Tang completed the HE staining of the tissue and described its microscopic performance. Lin Liu was responsible for the operation of small animal PET/CT in the experiment. Yue Chen provided scientific research ideas and paid for all research funding.

## References

- [1] F. H. Epstein and E. D. Harris Jr., "Rheumatoid arthritis. Pathophysiology and implications for therapy," *New England Journal of Medicine*, vol. 322, no. 18, pp. 1277–1289, 1990.
- [2] F. C. Arnett, S. M. Edworthy, D. A. Bloch et al., "The American Rheumatism Association 1987 revised criteria for the classification of rheumatoid arthritis," *Arthritis & Rheumatism*, vol. 31, no. 3, pp. 315–324, 1988.
- [3] N. Boutry, M. Morel, R.-M. Flipo, X. Demondion, and A. Cotten, "Early rheumatoid arthritis: a review of MRI and sonographic findings," *American Journal of Roentgenology*, vol. 189, no. 6, pp. 1502–1509, 2007.
- [4] G. A. W. Bruyn, P. Hanova, A. Iagnocco et al., "Ultrasound definition of tendon damage in patients with rheumatoid arthritis. Results of a OMERACT consensus-based ultrasound score focussing on the diagnostic reliability," *Annals of the Rheumatic Diseases*, vol. 73, no. 11, pp. 1929–1934, 2014.
- [5] H. J. J. M. Rennen, O. C. Boerman, W. J. G. Oyen, and F. H. M. Corstens, "Imaging infection/inflammation in the new millennium," *European Journal of Nuclear Medicine*, vol. 28, no. 2, pp. 241–252, 2001.
- [6] K. Kubota, H. Yamashita, and A. Mimori, "Clinical value of FDG-PET/CT for the evaluation of rheumatic diseases: rheumatoid arthritis, polymyalgia rheumatica, and relapsing polychondritis," *Seminars in Nuclear Medicine*, vol. 47, no. 4, pp. 408–424, 2017.
- [7] C. Beckers, C. Ribbens, B. Andre et al., "Assessment of disease activity in rheumatoid arthritis with ( $^{18}\text{F}$ )-FDG PET," *Journal of Nuclear Medicine: Official Publication, Society of Nuclear Medicine*, vol. 45, no. 6, pp. 956–964, 2004.
- [8] R. L. Burlison, M. C. Johnson, and H. Head, "Scintigraphic demonstration of experimental abscesses with intravenous  $^{67}\text{Ga}$  citrate and  $^{67}\text{Ga}$  labeled blood leukocytes," *Annals of Surgery*, vol. 178, no. 4, pp. 446–452, 1973.

- [9] A. Mirzaei, A. R. Jalilian, M. Akhlaghi, and D. Beiki, "Production of  $^{68}\text{Ga}$ -citrate based on a  $\text{SnO}_2$  generator for short-term turpentine oil-induced inflammation imaging in rats," *Current Radiopharmaceuticals*, vol. 9, no. 3, pp. 208–214, 2016.
- [10] S.-J. Chung, H.-J. Yoon, H. Youn et al., " $^{18}\text{F}$ -FEDAC as a targeting agent for activated macrophages in DBA/1 mice with collagen-induced arthritis: comparison with  $^{18}\text{F}$ -FDG," *Journal of Nuclear Medicine*, vol. 59, no. 5, pp. 839–845, 2018.
- [11] D. E. Trentham, A. S. Townes, and A. H. Kang, "Autoimmunity to type II collagen an experimental model of arthritis," *Journal of Experimental Medicine*, vol. 146, no. 3, pp. 857–868, 1977.
- [12] C. Xi, L. Tan, Y. Sun et al., "A novel recombinant peptide containing only two T-cell tolerance epitopes of chicken type II collagen that suppresses collagen-induced arthritis," *Molecular Immunology*, vol. 46, no. 4, pp. 729–737, 2009.
- [13] D. M. Lee and M. E. Weinblatt, "Rheumatoid arthritis," *The Lancet*, vol. 358, no. 9285, pp. 903–911, 2001.
- [14] W. B. van den Berg, "Animal models of arthritis. What have we learned?," *Journal of Rheumatology*, vol. 72, pp. 7–9, 2005.
- [15] A. E. Koch, "Angiogenesis as a target in rheumatoid arthritis," *Annals of the Rheumatic Diseases*, vol. 62, no. S2, pp. ii60–ii67, 2003.

## Research Article

# Dynamic Contrast-Enhanced MR with Quantitative Perfusion Analysis of Small Bowel in Vascular Assessment between Inflammatory and Fibrotic Lesions in Crohn's Disease: A Feasibility Study

**Davide Ippolito** <sup>1,2</sup>, **Sophie Lombardi**<sup>1,2</sup>, **Cammillo Talei Franzesi**<sup>1,2</sup>,  
**Silvia Girolama Drago**<sup>1,2</sup>, **Giulia Querques**<sup>1,2</sup>, **Alessandra Casiraghi**<sup>1,2</sup>, **Anna Pecorelli**<sup>1,2</sup>,  
**Luca Riva**<sup>1,2</sup>, and **Sandro Sironi**<sup>1,3</sup>

<sup>1</sup>School of Medicine, University of Milano-Bicocca, Milan, Italy

<sup>2</sup>Department of Diagnostic Radiology, San Gerardo Hospital H. S. Gerardo Monza, Via Pergolesi 33, 20900-Monza, MB, Italy

<sup>3</sup>Department of Diagnostic Radiology, Papa Giovanni XXIII Hospital H. Papa Giovanni XXIII, Piazza OMS 1, 24127 Bergamo, Italy

Correspondence should be addressed to Davide Ippolito; [davide.atena@tiscalinet.it](mailto:davide.atena@tiscalinet.it)

Received 23 June 2018; Revised 26 September 2018; Accepted 10 December 2018; Published 4 February 2019

Academic Editor: Anne Roivainen

Copyright © 2019 Davide Ippolito et al. This is an open access article distributed under the Creative Commons Attribution License, which permits unrestricted use, distribution, and reproduction in any medium, provided the original work is properly cited.

**Aim.** To assess the feasibility of dynamic contrast-enhanced perfusion-MRI in characterization of active small-bowel inflammation and chronic mural fibrosis in patients with Crohn's disease (CD). **Methods.** We analyzed a total of 37 (11 women; 23–69 years) patients with known biopsy proven CD, who underwent MR-enterography (MRE) study, performed on a 1.5 T MRI system (Achieva, Philips), using a phased array sense body multicoil, after oral administration of 1.5–2 L of PEG solution. MRE protocol included T1 weighted, SS T2, sBTfE, and gadolinium-enhanced THRIVE sequences acquired on coronal and axial planes. A dedicated workstation was used to generate perfusion color maps, on which we drawn ROI on normal bowel and on pathological segment, thus obtaining related perfusion parameters: relative arterial, venous, and late enhancement (RAE, RVE, and RLE), maximum enhancement (ME), and time to peak (TTP). **Results.** Quantitative perfusion analysis showed a good correlation with local degree of Crohn's inflammation activity. Twenty-nine out of 37 patients showed active inflammatory disease (reference standard of active disease: wall bowel thickness and layered enhancement) with following perfusion parameters: REA (%) = 116.1, RVE (%) = 125.3, RLE (%) = 127.1, ME (%) = 1054.7, TTP (sec) = 157. The same parameters calculated in patients with mural fibrosis were as follows: RAE (%): median = 56.4; RVE (%): 81.2; RLE (%): 85.4; ME (%): 809.6; TTP (sec): 203.4. A significant difference ( $p < 0.001$ ) between inflamed and fibrotic bowel wall vascularity, regarding all perfusion parameters evaluated, was found, with higher values in active CD localizations. **Conclusion.** Vascular assessment of perfusion kinetics of bowel wall by dynamic contrast perfusion-MR analysis may represent a complementary diagnostic tool that enables a quantitative evaluation of local inflammation activity in CD patients.

## 1. Introduction

In management of Crohn's disease (CD) patients, to assess the extent, severity and grade of activity is crucial for guiding therapeutic strategies.

Indeed, symptoms related to acute inflammation can benefit from anti-inflammatory drugs (such as corticosteroids, aminosalicylate, and immunomodulatory drugs), while fibrosis, which is an irreversible result of chronic

inflammation correlated with collagen deposition, causes a fixed luminal narrowing, is unresponsive to medical treatment, and requires mechanical intervention such as balloon dilation or stricturoplasty, or surgical resection [1, 2]. Diagnosis of CD and definition of inflammatory activity is made by a combination of clinical endoscopic, histological, biochemical, and radiological findings [3]. Several clinical methods are employed to investigate the nature of symptom's exacerbation, but they all present some limitations: endoscopy

is invasive and cannot evaluate the deeper bowel layers where collagen deposition may occur; video capsule does not provide histological sampling and is contraindicated in patients with suspected obstruction; CDAI (Crohn's disease activity index) includes subjective parameters such as pain, it is complex and time demanding, and serum markers do not completely correlate with disease activity [2, 4].

Recently, vascular biology has demonstrated the important relationship between neoangiogenesis and CD activity stages: it has been observed that acute inflammation is strictly correlated with an increase of vascular perfusion, while the advanced chronic stage is related to deposition of fibrotic tissue due to a decrease of vascularization, resulting in a reduction of tissue perfusion [5, 6].

The assessment of tissue perfusion, which is strictly related to neoangiogenesis, can be evaluated *in vivo*, thanks to dynamic contrast-enhanced MR (DCE-MR), that provides quantitative and semiquantitative measurements of tissues blood flow, by the acquisition of series of T1-weighted images before, during and after contrast material injection. This technique allows the evaluation of enhancement as a function of time and, therefore, to calculate several quantitative parameters related to functional tissues' perfusion aspects.

Some studies evaluated the possibility to investigate CD with DCE-MR, applying different acquisition protocols and perfusion models, in order to obtain objective measurements that could increase the accuracy of standard morphological MR sequences in the definition of disease activity and treatment response [7, 8].

Indeed, to assess the disease activity degree only on the basis of morphological sequences alone can be challenging, as it is partially based on subjective visual assessment.

On this basis, the aim of our study was to evaluate the possibility to determine the level of disease activity of small-bowel segment in CD patients applying a semiquantitative perfusion method using standard dynamic contrast-enhanced MR sequences.

## 2. Materials and Methods

**2.1. Study Population.** This prospective study was carried out in a single institution. The study protocol was approved by our institutional review board, and informed consent was obtained from each participant. From January 2016 to December 2017, a total of 37 patients with biopsy proven Crohn's Disease, who underwent a standard DCE-MR imaging examination for follow-up or for suspicion of relapse of disease, were retrospectively enrolled in the study.

The inclusion criteria were (a) a known CD biopsy proven in follow-up evaluation and (b) known CD with clinical suspicion of relapse. The exclusion criteria were (a) contraindications for MRI (electrically, magnetically, or mechanically activated devices; central nervous system haemostasis clips), (b) pregnancy, (c) renal insufficiency, and (d) documented adverse reaction to gadolinium-based contrast agent.

**2.2. MRI Technique.** MR-enterography (MRE) was performed by using a 1.5 T magnet (Philips, Achieva MR

system), with a phased array body coil. The exam was acquired with patients in prone position.

We followed the methods we applied in our previous paper in 2010 [9].

A polyethylene glycol (PEG) solution was given to the patients, with a total of 1500–2000 mL within 60 min prior to scanning, with the first 500 mL ingested over the first 15 min and two 500 mL aliquots consumed 25 and 15 min prior to scanning, respectively, to obtain a sufficient bowel luminal distension and to guarantee an accurate detection of the lesions. To reduce bowel peristalsis and related motion artifacts, 20 mg of *N*-butyl-scopolamine (Buscopan; Boehringer, Ingelheim, Germany) were intravenous (i.v.) administered immediately before contrast imaging.

After acquiring standard three-plane scout images, the precontrast protocol included the following sequences: axial and coronal single shot fast SE with fat saturation acquired during breath hold, coronal and axial BTFE sequences, and axial T1w in phase sequences (Table 1).

The contrast dynamic images were acquired on coronal plane by applying 3D T1 THRIVE (T1 high resolution isotropic volume examination) gradient echo sequences with fat saturation (slice thickness: 2 mm; TE: 2.9 ms; TR: 4.1 ms; matrix 256 × 196; 21 seconds for each dynamic sequence; FOV: 400; number of slices: 80) before and after intravenous injection of 0.1 mL/kg of gadoteric acid (Gadobutrol, Gadovist, Bayer, Leverkusen, Germany), with a flow rate of 1.5 mL/sec and followed by a 30 mL saline flush at the same rate, using a power injector. The volume of the contrast agent was calculated on the basis of patient's body weight.

A real-time display, by using fluoroscopic technique, returned low-resolution images every second to permit breath-held coordination with contrast arrival at the level of descending aorta. The arterial phase MR imaging was acquired immediately after the visual detection of contrast material at descending aorta by using a real-time bolus displayed method; the venous phase was performed with a fixed image delay of 80 s, followed by delayed coronal imaging at 4 min after contrast agent injection.

The timetable for an MR enterographic examination was about 20 min for all of the cases.

**2.3. DCE-MRI Technique.** The mechanism of tissue enhancement observed on T1-weighted images is based on T1 relaxation time shortening caused by the contrast medium.

Multiphase dynamic contrast-enhanced MR, performed using standard contrast dynamic acquisitions of three-dimensional spoiled gradient echo sequences with fat suppression (THRIVE) on the coronal plane, were used to perform the quantitative analysis.

Afterwards, DCE raw data sets were transferred from MR scanner to an independent image workstation with dedicated perfusion software (Viewforum; Philips Medical Systems) that generate color perfusion images map, time-intensity curves, and calculate perfusion parameters of selected areas.

Functional perfusion maps were generated by means of a dedicated perfusion software (T1 Perfusion Package, Philips

TABLE 1: Descriptive parameters of acquisition protocol for the study of abdomen employed.

Sequences	Acquisition parameters					
	FA	Thickness	TR (msec)	TE (msec)	NSA	Matrix size
SSh T2 ax	90°	6 mm	8901	103	1	336 × 227
BFFE M2D ax	60°	6 mm	3.1	1.57	1	224 × 228
BTFE SPAIR ax	60°	6 mm	3.9	1.47	1	204 × 178
T1W in-phase ax	80°	6 mm	206	4.6	1	236 × 167
SSh T2 SPAIR ax	90°	6 mm	8736	96	1	308 × 220
T2W TSE BH cor	90°	5 mm	8956	100	1	292 × 254
BTFE M2D cor	60°	5 mm	3.7	1.84	1	264 × 265
ShT2 SPAIR cor	90°	5 mm	11336	127	1	392 × 309
THRIVE cor (4 dynamic phases)	10°	4 mm	4	1.91	1	292 × 294
THRIVE ax	10°	4 mm	3.5	1.67	1	236 × 212

Note. FA = flip angle; TR = repetition time; TE = echo time; NSA = number of signals acquired; AX = axial plane; SSh = single shot; BTFE = balanced turbo field echo; BFFE = balanced fast field echo; COR = coronal plane; ax = axial; cor = coronal.

Medical Systems) and were displayed in a color scale ranging from blue to red, blue being the lowest range of display.

The functional color map was used in combination with contrast-enhanced images to select the pathological segment where an ROI (region of interest) was manually drawn in the thickest part of the bowel wall, avoiding to include the lumen; a second ROI was drawn in a normal small-bowel segment.

For each ROI the following quantitative parameters were calculated: maximum enhancement (ME, %), relative arterial enhancement (RAE, %), relative venous enhancement (RVE, %), relative late enhancement (RLE, %), relative enhancement (RE, %), and maximum relative enhancement (MRE, %), and time to peak (s).

RAE, RVE, and RLE represent the percentage of intensity signal of contrast material concentration in the three different enhancement phases; ME represents the highest absolute values of intensity signal, and TTP corresponds to the time to reach the maximum value of contrast material concentration.

The relative enhancement (RE) (%) was derived from the signal enhancement of a pixel of specific (arterial, venous, or delayed) dynamic relative to that same pixel in the reference dynamic. The reference dynamic is normally the first, pre-contrast dynamic. The reference dynamic can be set to another dynamic, where  $I(D)$  stands for pixel intensity of current dynamic and  $I(D_{ref})$  stands for pixel intensity of reference dynamic created with the following formula:  $\text{relative enhancement} = (I(D)/I(D_{ref}) - 1) \times 100$ , where  $I(D)$  stands for pixel intensity of current dynamic and  $I(D_{ref})$  stands for pixel intensity of reference dynamic [10, 11].

## 2.4. Image Analysis

**2.4.1. Morphological Image Analysis.** A dedicated radiologist, expert in abdominal imaging, evaluated the presence of mural and extramural CD findings in the bowel wall to determine the degree of activity of the pathological segment. When more than one involved segment was present, the most evident was considered. The radiological features considered as disease localization in the bowel wall were wall thickening, increased enhancement, layered enhancement (bilaminar or trilaminar appearance), or transmural enhancement. The

extraluminal features and complications evaluated were regional dilation of vasa recta (comb sign), enlargement of mesenteric lymph nodes, fat stranding, small-bowel obstruction, abscesses, fistulas, and free abdominal fluid. Active disease was defined by the presence of mural thickening and increased layered enhancement along with perivisceral inflammatory changes (fat stranding and vascular congestion). Chronic disease was determined by the presence of transmural homogeneous enhancement, small-bowel stricture, and no association of extramural acute findings (vascular congestion and enlarged lymph nodes) [12].

**2.4.2. Perfusion Analysis.** For each patient, we have drawn an ROI in a normal small-bowel segment and one in the more evident pathological segment, to obtain perfusion information (time-intensity curves and perfusion values) of both those two segments.

Time-signal intensity curves were obtained automatically for every patient on the dedicated workstation by applying an automatic realignment of dynamic series in order to minimize potential ROI sampling inaccuracies due to the patient's motion or residual peristalsis.

Time-intensity curves generated by the perfusion software were classified in type I for those presenting a progressive increasing trend of the curve, and type II for those presenting a plateau of enhancement (Figure 1).

The perfusion values of ME, RAE, RVE, RLE, and TTP relative to each curve were then recorded. Analysis of data set took about 10–15 minutes for quantitative evaluation, determination of perfusion kinetics parameters, and perfusion curve creation.

To test the reproducibility of the study a second radiologist, blinded to previous results, reviewed the images and determined the degree of activity of pathological bowel segment, as active or chronic, and performed the perfusion analysis by drawing ROI in a normal small-bowel loop and in the most pathological bowel segment.

**2.5. Statistical Analysis.** All statistical analyses were performed using commercially available software (Med Calc, Med Calc Software 14.8.1, Mariakerke, Belgium) and SPSS 21.0 statistical package (SPSS Incorporated, Chicago, Illinois, USA).

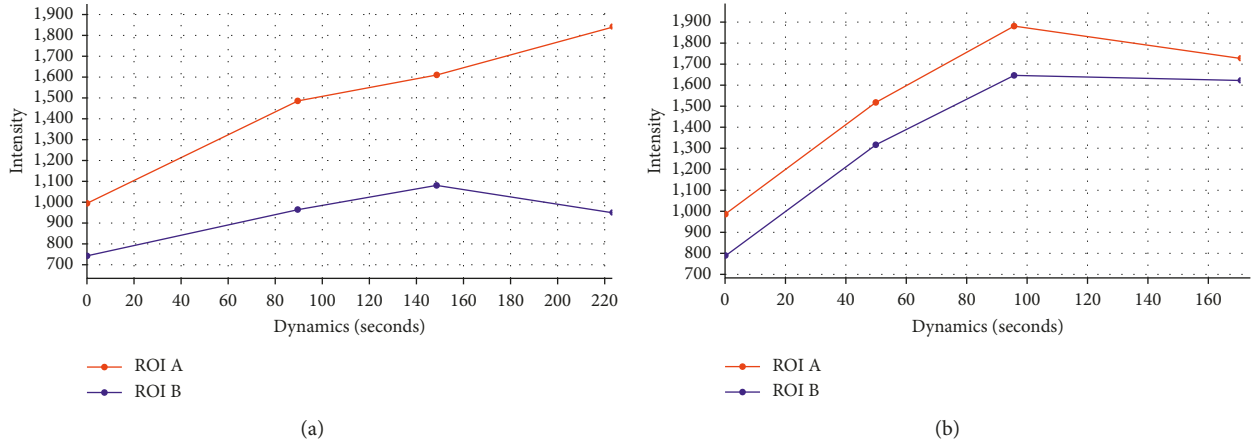


FIGURE 1: Time-intensity curve describing active lesion: (a) Type I presented increasing trend of the curve (ROI A); (b) curve describing chronic lesion (ROI A) were more similar to normal bowel and presented plateau of enhancement.

Presence or absence of each conventional MR finding in terminal ileum or in small bowel was recorded and summarized.

Average values and standard deviations were calculated for quantitative MRE parameters (DCE-MRI parameters (RE, RLE, and ME values)) for normal and pathological segments (active and chronic) localization.

Quantitative perfusion parameters were compared between the terminal ileum and normal ileal loop of active CD patients by using the two-sample *t*-test.

Cohen's kappa was run to test the agreement between the two radiologists in the assessment of active or chronic bowel disease. Agreement was considered excellent if kappa was more than 0.80, good if it ranged from 0.61 to 0.80, moderate if it ranged from 0.41 to 0.60, and poor if it was 0.40 or less. The reliability of perfusion parameters derived from the two different radiologists was measured by means of interclass correlation coefficient (ICC) and its corresponding 95% confidence interval (95% CI). The ICCs were classified as follows: excellent  $>0.90$ ; good between 0.75 and 0.90, moderate between 0.50 and 0.75, poor  $<0.50$ .

The prognostic accuracy of RAE, RVE, RLE, ME, and TTP values in the assessment of acute bowel inflammation were assessed through the calculation of the areas under the receiver operator curve (AUROC), where values close to 1.0 indicate an ideal parameter and values below 0.5 indicate a parameter without prognostic significance. Confidence intervals at 95% (95%CI) are also shown. The best cutoff for each parameter was chosen to maximise sensitivity and specificity.

Statistical significance was assessed at  $p$  value  $<0.05$ .

### 3. Results

A total of 23 out of 37 patients presented the typical signs of active disease in the morphological study (reference standard disease activity: wall bowel thickness, hyperenhancement, and layered enhancement). Those patients showed the following perfusion parameters at perfusion analysis: RAE (%): median = 116.1 (1st qt = 97.1, 3rd qt = 110.8); RVE (%)

median = 125.3 (1st qt = 113.4, 3rd qt = 136.9); RLE (%): median = 127.1 (1st qt = 116.2, 3rd qt = 141.0); ME (%): median = 1054.7 (1st qt = 978.6, 3rd qt = 1098.4); and TTP (sec): median = 157 (1st qt = 141.3, 3rd qt = 176.2) (Table 2).

A total of 10 patients presented typical signs of chronic disease (reference standard disease activity: wall bowel thickness and transmural hyperenhancement). In those patients the following perfusion parameters were obtained: RAE (%): median = 56.4 (1st qt = 46.9, 3rd qt = 71.2); RVE (%): 81.2 (1st qt = 73.3, 3rd qt = 94.1); RLE (%): 85.4 (1st qt = 79.7, 3rd qt = 103.1); ME (%): 809.6 (1st qt = 720.3, 3rd qt = 861.2); and TTP (sec): 203.4 (1st qt = 182.4, 3rd qt = 214.5) (Table 2).

A significant difference ( $p < 0.001$ ) between inflamed and fibrotic bowel wall vascularity was found for all perfusion parameters evaluated, with higher values in active lesions, with the exception of time to peak, which instead was significantly higher in the chronic forms, as expected from a fibrotic tissue (Table 2).

In all 23 patients with morphological diagnosis of active disease, the time-intensity curve presented a type I curve (increasing trend), and the activity of CD was confirmed by standard morphological MRI findings of previous and following examinations of the same patient.

While in all 10 patients with morphological findings of chronic disease, a type II curve (plateau of enhancement) was obtained and the diagnosis was confirmed by follow-up exams.

The corresponding perfusion values calculated in normal bowel segment were as follows (Table 2): RAE (%): median = 44 (1st qt = 39.7, 3rd qt = 52.9); RVE (%): median = 71 (1st qt = 56.9, 3rd qt = 79.7); RLE (%): median = 57.9 (1st qt = 51, 3rd qt = 64.1); ME (%): median = 749.8 (1st qt = 633.3, 3rd qt = 809.09); MRE (%): median = 69 (1st qt = 56.8, 3rd qt = 85.5); and TTP (sec): median = 162.3 (1st qt = 169.1, 3rd qt = 185.8) (Table 2).

Using the univariate unpaired Wilcoxon rank test, no significant differences ( $p < 0.001$ ) were found for all the perfusion parameters calculated in segment with chronic localizations and those segments not affected by CD (Table 2).

TABLE 2: The functional data obtained in bowel wall for active inflammation and chronic inflammation and normal findings by semi-quantitative analysis of DCE-perfusion study.

Functional parameters	Active inflammation (26 patients)	Chronic inflammation (11 patients)	Normal bowel (37 patients)	<i>p</i> value ( <i>p</i> < 0.05)
RAE (%)				<0.001
1st qt	97.1	46.9	39.7	
Median	116.1	56.4	44	
3rd qt	110.8	71.2	52.9	
RVE (%)				<0.001
1st qt	113.4	73.3	56.9	
Median	125.3	81.2	71	
3rd qt	136.9	94.1	79.7	
RLE (%)				<0.001
1st qt	116.2	79.7	51	
Median	127.1	85.4	57.9	
3rd qt	141.0	103.1	64.1	
TTP (sec)				<0.029
1st qt	141.3	182.4	169.1	
Median	157	203.4	162.3	
3rd qt	176.2	214.5	185.8	
ME (%)				<0.039
1st qt	978.6	720.3	633.3	
Median	1054.7	809.6	749.8	
3rd qt	1098.4	861.2	809.09	

RAE: relative arterial enhancement; RVE: relative venous enhancement; RLE: relative late enhancement; TTP: time to peak; ME: maximum enhancement.

A group of 4 patients could not be classified as active nor chronic CD only on the basis of standard morphological sequences, for incomplete or not reliable presence of typical luminal and extraluminal signs related to one of the two forms.

In 3 of those patients (i.e., nontypical pattern of enhancement, mild extravascular congestion, no submucosal edema, no enlarged lymph nodes, or perivisceral fat stranding), the perfusion analysis demonstrated significantly higher perfusion values than normal bowel and a type I time-intensity curve (Figure 2).

In 1 patient, the perfusion analysis demonstrated perfusion values similar to those of normal bowel and type II time-intensity curve.

In those 4 patients with undefined CD localizations, an endoscopic study was performed to define the activity degree and better determine the correct medical approach.

The three patients that presented type I curve had an endoscopic diagnosis of acute disease, while the patient with type II curve presented a diagnosis of chronic disease.

**3.1. Test Reproducibility.** According to the second radiologist who reviewed the images, 26 patients had active and 11 chronic bowel disease, showing an excellent agreement with the first radiologist, in the assessment of bowel disease activity ( $\kappa = 0.810$ ;  $p < 0.0001$ ).

The ICC of the perfusion parameters derived by the two different radiologist were as follows: RAE = 0.931 (95% CI = 0.871–0.); RVE = 0.990 (95% CI = 0.981–0.995); RLE = 0.988 (95% CI = 0.976–0.994); ME = 0.999 (95% CI = 0.998–0.999); and TTP (sec) = 0.988 (95% CI = 0.977–0.994).

**3.2. Diagnostic Accuracy of Perfusion Values.** The ability of RAE, RVE, RLE, and ME in the assessment of acute bowel inflammation was very good, with an AUC of 0.932 (95% CI: 0.850–1.000), 0.955 (95% CI: 0.892–1.000), 0.949 (95% CI: 0.883–1.000), and 0.909 (95% CI: 0.807–1.000), respectively (Figure 3). The optimal cutoff level for each value was as follows: 108.9 (sensitivity = 88.46%, specificity = 100%) for RAE, 119.5 (sensitivity = 88.46%, specificity = 100%) for RVE, 119.2 (sensitivity = 88.46%, specificity = 100%) for RLE, and 1046.5 (sensitivity = 88.46%, specificity = 100%) for ME. Instead, the ability of TTP in discriminating acute versus chronic bowel inflammation was very poor, with an AUC of 0.075 (95% CI: 0.000–0.219).

## 4. Discussion

In Crohn's disease management, stage-adjusted treatment relies on accurate evaluation of the degree of inflammation; in fact, it is crucial to differentiate inflammatory from fibrotic strictures as the inflammatory strictures can benefit from medical therapy, whereas fibrotic strictures may require surgical resection or mechanical therapy [13].

Moreover, it is of outstanding importance to objectively measure CD inflammatory activity to select the patients that are suitable for new therapeutic drugs and to evaluate the effectiveness of those new treatments [4].

Different clinical and instrumental tools (such as the CDAI, biologic indices, and endoscopic and imaging studies) have been used to monitor the disease activity and the response to treatment, but all of them presents limits and cannot alone assess the level of disease [13]. Exacerbation of symptoms caused by a stenosis, with a persisting luminal narrowing and upstream bowel dilatation, may result from

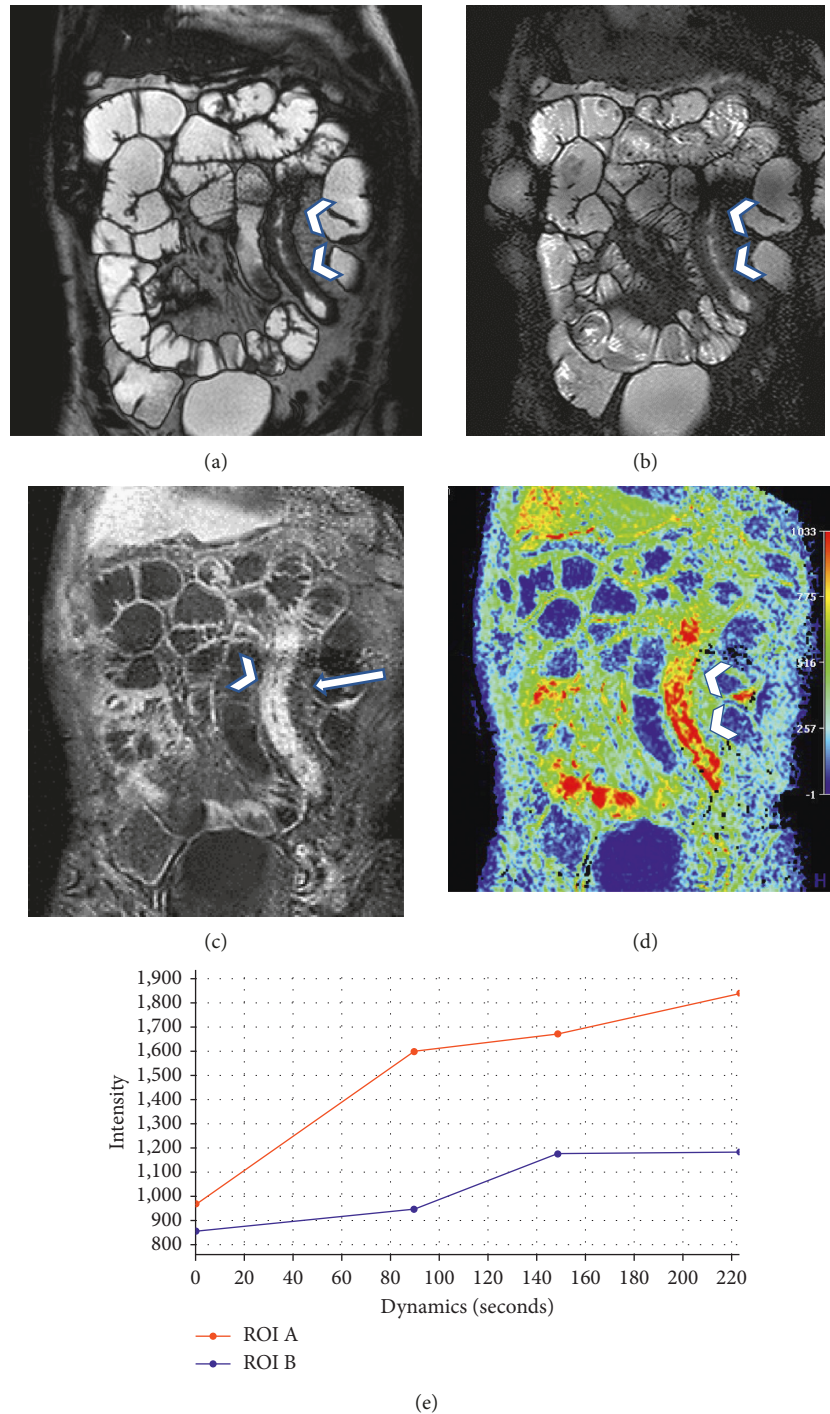


FIGURE 2: A case presenting with findings that do not allow classifying the disease as active or chronic; on the basis of the morphological sequences alone, there is an evident thickening of bowel ileal loop, not presenting hyperintensity in T2-weighted sequences (arrowhead in (a) and (b)), but with a slight vascular congestion (arrow in (c)) and a strong enhancement in dynamic study (arrowhead in (c)), that does present a very typical layered enhancement. The perfusion analysis demonstrates a time-intensity curves with an increasing trend of enhancement and higher perfusion values than those of the normal bowel, suggesting the presence of acute disease.

active inflammation, fibrosis, or a combination of the both. In fact, CD exhibits a progressive, destructive course and can consequently result in a progression and overlap of active and chronic lesions [14].

MR-enterography is one of the most used imaging techniques, together with CT-enterography, and it can help to

differentiate active from chronic lesion. Indeed, a mural thickening of the small bowel associated with wall edema on T2-weighted images and an intense layered enhancement, associated with extraparietal findings of active disease (mesenteric fat stranding, comb sign, and enlarged lymph nodes), suggests the presence of an active inflammation, while

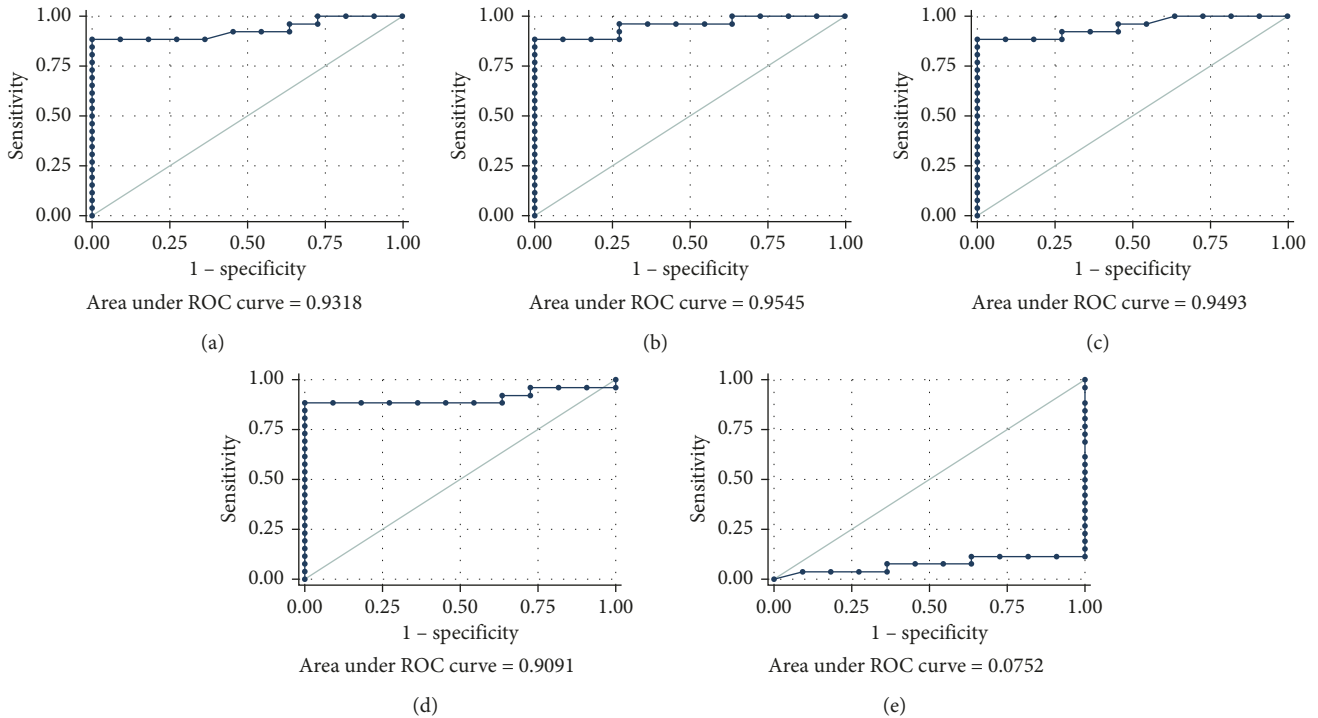


FIGURE 3: ROC curves and AUC of perfusion parameters. Sensitivity and Specificity of the 5 perfusion parameters evaluated: (a) RAE (cutoff value of 108.9), (b) RVE (cutoff value of 119.5), (c) RLE (cutoff value of 119.2), (d) ME (cutoff value of 1046.5), and (e) TTP (not statistically significant).

mural thickening with low signal intensity on T2-weighted sequences, a relatively low homogenous enhancement and the lack of extraluminal inflammation are related to nonactive disease. Moreover, the homogenous enhancement is not specific, as it can be associated either to active disease when intense or to chronic when less intense [3].

Therefore, distinguishing the pattern of enhancement is a main clue, but the major limitation of standard morphological sequences is that the evaluation of the enhancement intensity is largely subjective, so more objective parameters evaluating enhancement of pathological bowel may be needed as a complement to visual assessments of bowel wall enhancement [15].

Angiogenesis consists in new capillary formation from preexisting vasculature, and it is involved in many complex biological processes, including growth, development, and repair of tissue. It has an essential role in the growth of tumors, and it is the target of the new antiangiogenic drugs in cancer therapy. Moreover, vascular biology has demonstrated the role of neoangiogenesis also in different inflammatory disease and malignant tumors, showing generally an early and increased enhancement in inflammation versus fibrosis [4, 16, 17, 18]. In particular, in the early stages of CD, acute inflammation has been related to an increase of vascular perfusion correlated with an abnormal distribution of arteries with small luminal irregularities in the peripheral branches. On the contrary, in the advanced stages of CD, a decrease of vessel diameter and vascular density and a reduction of regional blood flow have been documented [5, 18]. DCE-MR imaging is based on the acquisition of serial fast T1-weighted images before, during, and after administration of contrast agent, and it provides

functional parameters about the perfusion of tissues. DCE-MRI functional parameters can be obtained with a quantitative or a semiquantitative method; the semiquantitative approach is easier and faster to calculate and takes into account parameters directly derived by the time-enhancement curve [19, 20].

The perfusion parameters have been extensively used as imaging surrogate biomarkers of tissues inflammation and evaluation of oncologic drugs effectiveness. So, these parameters can potentially be useful for assessing inflammation activity and follow-up of patients with CD.

Indeed, DC-MRI provides quantitative, spatially encoded information about the walls of the entire bowel segment that enables to obtain objective measures of CD inflammatory activity, which can be used to evaluate the effectiveness of recently introduced therapies, as well as to improve the interpretative accuracy.

In our results, we obtained two different set of perfusion parameters values and curves, related, respectively, to acute and chronic CD morphological MRI findings, that are in line with the physiopathological patterns of CD manifestations.

In fact, in cases that presented with characteristics of acute disease at standard morphological sequences, we observed significantly higher perfusion values than that of normal bowel, for all the parameters considered. The related time-intensity curves presented an important upslope with a high peak of enhancement, due to early, rapid, and marked increasingly contrast enhancement that is the expression of increased vascularity and late increased capillary permeability of contrast material, typical of active inflammation. We defined that kind of curve as type I (Figure 4).

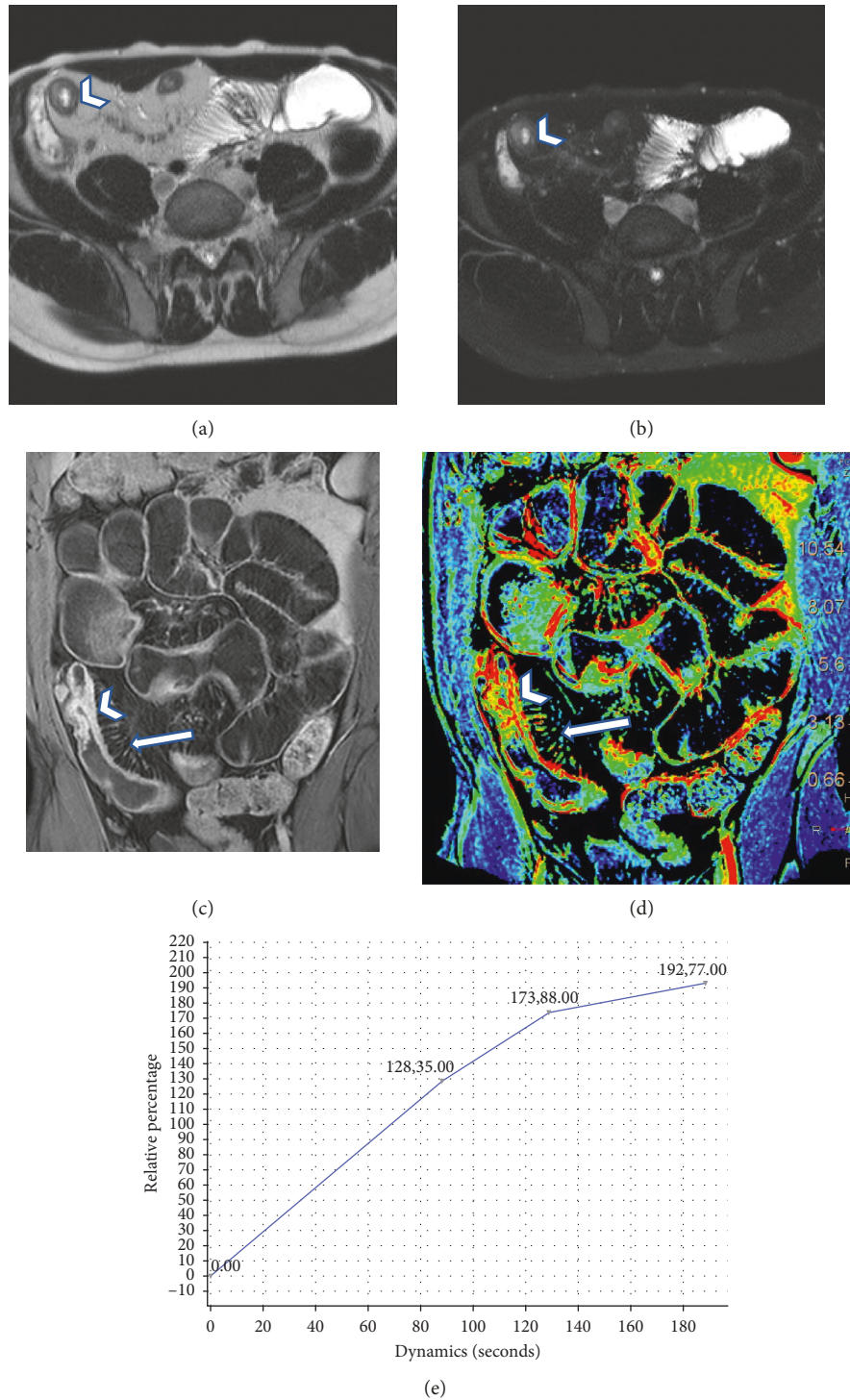


FIGURE 4: A 45-year-old man with known active disease characterized by the presence of mural thickening of last ileal bowel loop characterized by mild hyperintensity in the T2-weighted images (arrowhead in (a) and (b)), layered enhancement in dynamic study (arrowhead in (c)), and vascular congestion associated (arrow). The perfusion analysis allows highlighting the pathological segment in the color map (d), and the time-intensity curves demonstrate an increasing trend of enhancement for pathological loops.

Instead, in patient presenting with morphological findings of chronic disease, we observed perfusion values similar to that of the normal bowel; the time-intensity curve were characterized by lower upslope of enhancement followed by a plateau due to the late accumulation of contrast agent in the interstitial space as a consequent increased of

capillary permeability, typical of chronic and inactive CD localizations, where logistic phenomenon are less represented. We defined those curves as Type II (Figure 5).

In 4 cases of our series where the morphological findings were not univocal (for not complete or reliable presentation luminal and extraluminal findings) and the observer could

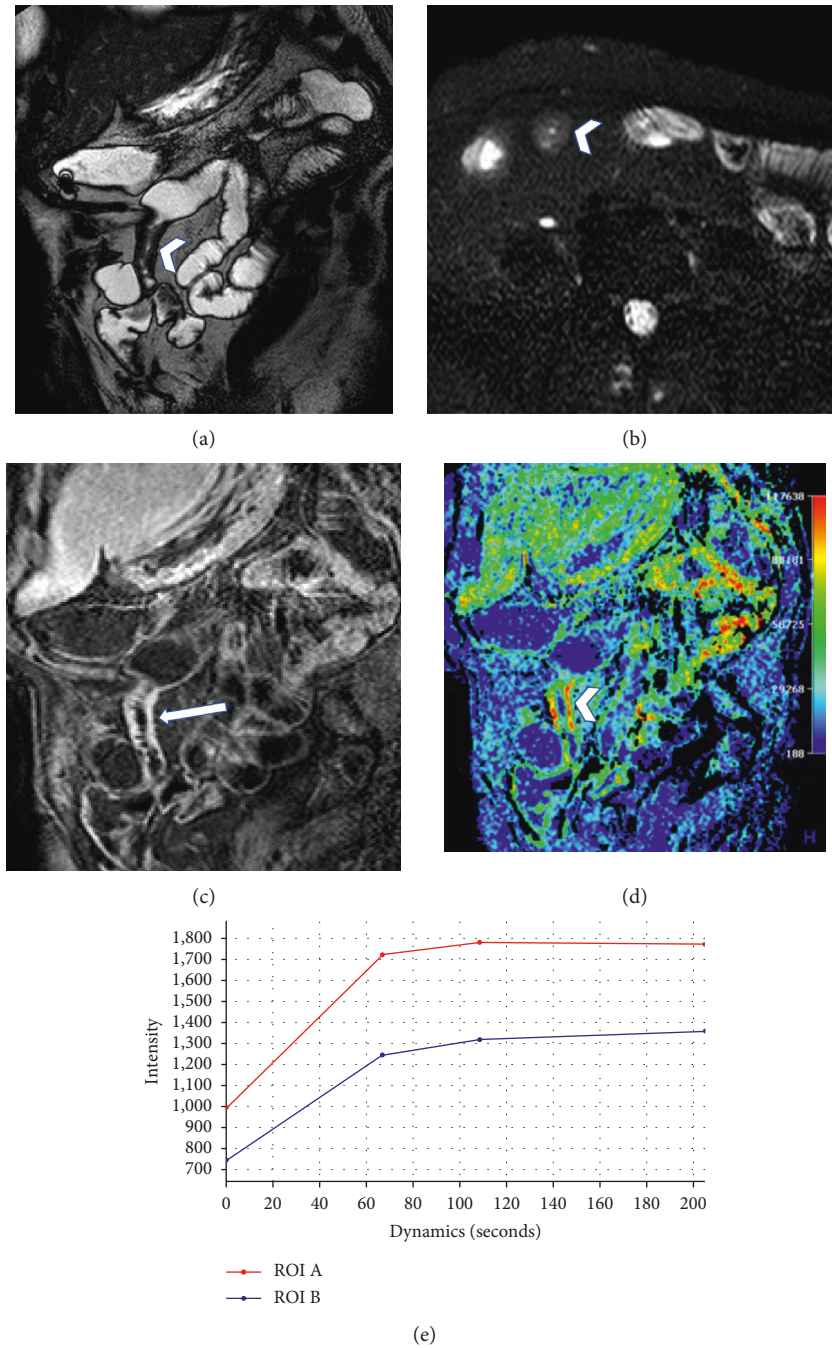


FIGURE 5: A 32-year-old female with known chronic disease presenting with fibrostenotic mural thickening of ileal segment (arrowhead in (a)), without T2 hyperintensity (arrowhead in (b)), and typical homogenous transmurial enhancement (arrow in (c)). The perfusion analysis highlights the pathological segment in the color map (arrowhead in (d)). In this case, the time-intensity curves are characterized by plateau of enhancement (e), with a curve similar to that of the normal bowel.

not confidently classify them as acute or chronic, the perfusion analysis presented characteristic of perfusion values and curves of acute or chronic lesions.

In the CD context, local vascularization is known to increase with the severity of the disease and a correlation between degree of tissue enhancement and inflammation severity has been found by other authors [17, 21]. Based on these pathophysiological grounds, a strong and early increase of contrast enhancement after intravenous injection

of a bolus of paramagnetic contrast material may be interpreted as a vivo marker of inflammation of small-bowel loops affected by active CD.

Distention of bowel loops with oral contrast and use of an antiperistaltic agent before the study helped decrease the motion related artifacts and improved the delineation of the bowel wall. Therefore, we could perform DCE-MRI analysis for the terminal ileum and normal ileal wall in all of the patients.

Our conclusions are in line with the results of Giusti et al.; they used DCE-MRI with a semiquantitative approach to differentiate activity stage of CD, observing that this method allows reliable differentiation between active and inactive CD, with a correspondence of perfusion parameter and of time-intensity curves. Even if they applied a semi-quantitative method, there are many differences in the technique applied: they used a GE 1.5 T scanner, acquiring nine dynamic series, with a total acquisition time of 6 minutes and 28 seconds.

They considered different perfusion parameters from those that we used in our study, with the exception of maximum enhancement (ME), as they used the ratio between latest enhancement value (6 min 28 s) and ME (LE/ME) and enhancement upslope (US). Anyway, considering the overall values, our results confirm this work, as in both cases values of perfusion related to active disease were significantly higher than in chronic disease. They described a type I curve related to active disease, with high early upslope and late plateau and a type II curve describing chronic curve with smoother upslope with gradual late washout of contrast material. The differences in the trends of the curves obtained can be explained by the different timing and method of acquisition of the dynamic contrast images due to the first pass perfusion study used in our series, in which only the first part of the enhancement is evaluated; this approach can determine different shape of the curves [17].

Röttgen et al. performed DCE-MRI analysis on patients with known active CD and correlated their results with ileocolonoscopy grading of active disease. They performed MR acquisition with enteroclysis technique, acquired 150 contrast dynamic images in 109 s, and selected different perfusion parameters from those we selected (slope of the contrast enhancement curve, AUC, and peak maximum).

Even if the analysis was made on a different kind of population (only acute patients) with a different DCE-MRI technique, their conclusions are in line with our results pointing out the correlation between semiquantitative perfusion parameters and degree of activity in CD [4].

Oto et al. performed DCE-MRI and DWI analysis on patient with known active disease to identify inflamed small-bowel segment and to differentiate it from normal bowel. They applied a quantitative perfusion method (evaluating  $K_{trans}$  and  $V_e$ ) obtaining significant difference between active and normal bowel, and they also obtained a good correlation between perfusion and ADC values in identifying active disease.

They demonstrated that, also with the quantitative perfusion method, it is possible to obtain a correlation between quantitative perfusion analysis and endoscopic and histologic findings and with ADC measurement as well [16].

One of the major limitations of our study is that, due to the retrospective nature of the study, we did not compare MRI findings with clinical scoring or histological results, so the comparison was limited to the findings of morphological MR sequences and the results of perfusion analysis. Another issue is that the dynamic MR acquisition was interrupted at 240 seconds after intravenous contrast material injection, thus not obtaining information about more delayed phase of

enhancement. In fact, we retrospectively performed the perfusion analysis on patients that underwent a standard four phase contrast study, with standard delayed phase: arterial (40 s), venous (80 s), and delayed (240 s) phase, which is our standard MR contrast protocol for CD patients. However, even if we did not acquire more delayed phase, we were still able to differentiate active from chronic pattern of perfusion, with the advantage of not modifying our standard routine protocol and not implementing scanning time with a possible discomfort for patients. The temporal resolution between different signal intensity measurements on dynamic contrast-enhanced images is rather low allowing to measure a relatively limited set of semiquantitative information. But this restriction has prevented us from performing a more complex analysis about dynamic behavior of contrast enhancement, being more reliable in clinical practice, and less time demanding. The pattern of the time-intensity curve that we obtained was different from that of other similar studies, but it is known that one of the main issues of DCE-MR imaging is a weak reproducibility of signal measurement between different observers, as results are strongly influenced by differences of equipment, acquisitions protocols, and perfusion model used.

Due to the small size of the study population, we were not able to confidently set a cutoff value of perfusion values between active and chronic lesions, also because the number of patients with chronic lesion was limited in comparison with the number of acute and chronic patients corresponds to the increasingly need to study patient who are symptomatic or with recurrence, that occurs more often in patient with acute disease.

As this has to be considered a feasibility study, we did not evaluate the reproducibility of quantitative measurements performed, which should be considered for a further clinical use of this perfusion analysis method.

## 5. Conclusion

Dynamic contrast-enhanced MRI is a promising technique that may be included in the clinical routine evaluation of patients with Crohn's disease, to implement the diagnostic reliability of MR in identifying pathological segments and differentiating between active and chronic CD of small bowel, and by offering objective quantitative parameters (absolute perfusion values and time-intensity curves). Those information can be used as a complementary tool to confirm the observation made on the morphological sequences.

## Data Availability

The data used to support the findings of this study are available from the corresponding author upon request.

## Additional Points

*Core Tip.* Recently, vascular biology has demonstrated the important relationship that exist between neoangiogenesis

and Crohn's disease (CD) activity stages, and it has been observed that acute inflammation is strictly correlated with an increase of vascular perfusion. Therefore, beside traditional radiological techniques, new functional imaging tools have been introduced in clinical practice in order to provide not only morphological information but also quantitative functional data, strictly related to the vascularization of tissue. The tissue perfusion can be evaluated in vivo thanks to dynamic contrast-enhanced MR (DCE-MR), which provides quantitative and semiquantitative measurements of tissues blood flow, offering comprehensive information about CD.

## Disclosure

The preliminary results of this manuscript were presented as oral communication (S.S. 6.4) during the 28th Annual Meeting and Postgraduate Course ESGAR 2017/June 20–23/ Athens, Greece.

## Conflicts of Interest

All the authors are aware of the content of the manuscript and have no conflicts of interest.

## Authors' Contributions

DI is the guarantor of integrity of the entire study; DI and SL designed the study concepts; DI, SL, and CTF designed the study; CTF, SGD, and LR performed the literature research; DI, SL, GQ, and AP performed the clinical studies; SL and DI were responsible for data acquisition; SL, DL, and AP performed data analysis/interpretation; DI performed statistical analysis; SL, DI, and CTF were responsible for the manuscript preparation; DI and SS were responsible for manuscript definition of intellectual content; DI and CTF edited the manuscript; all the authors revised and reviewed the manuscript; DI approved the final version of the manuscript.

## Acknowledgments

We wish to thank Prof. Adam Cassels for his contribution in amending and polishing the language of this manuscript. We thank Dr. Alessandra Casiraghi for assistance and support in addressing the preliminary results of this manuscript.

## References

- [1] A. A. Plumb, A. Menys, E. Russo et al., "Magnetic resonance imaging-quantified small bowel motility is a sensitive marker of response to medical therapy in Crohn's disease," *Alimentary Pharmacology and Therapeutics*, vol. 42, no. 3, pp. 343–355, 2015.
- [2] K. B. Quencer, K. Nimkin, M. Mino-Kenudson, and M. S. Gee, "Detecting active inflammation and fibrosis in pediatric Crohn's disease: prospective evaluation of MR-E and CT-E," *Abdominal Imaging*, vol. 38, no. 4, pp. 705–713, 2013.
- [3] J. H. Yacoub, P. Obara, and A. Oto, "Evolving role of MRI in Crohn's disease," *Journal of Magnetic Resonance Imaging*, vol. 37, no. 6, pp. 1277–1289, 2013.
- [4] R. Röttgen, T. Grandke, C. Grieser, L. Lehmkuhl, B. Hamm, and L. Lüdemann, "Measurement of MRI enhancement kinetics for evaluation of inflammatory activity in Crohn's disease," *Clinical Imaging*, vol. 34, no. 1, pp. 29–35, 2010.
- [5] F. Maccioni, M. A. Patak, A. Signore, and A. Laghi, "New frontiers of MRI in Crohn's disease: motility imaging, diffusion-weighted imaging, perfusion MRI, MR spectroscopy, molecular imaging, and hybrid imaging (PET/MRI)," *Abdominal Imaging*, vol. 37, no. 6, pp. 974–982, 2012.
- [6] S. A. Taylor, S. Punwani, M. Rodriguez-Justo et al., "Mural Crohn disease: correlation of dynamic contrast-enhanced MR imaging findings with angiogenesis and inflammation at histologic examination-pilot study," *Radiology*, vol. 251, no. 2, pp. 369–379, 2009.
- [7] G. Bhatnagar, N. Dikaios, D. Prezzi, R. Vega, S. Halligan, and S. A. Taylor, "Changes in dynamic contrast-enhanced pharmacokinetic and diffusion-weighted imaging parameters reflect response to anti-TNF therapy in Crohn's disease," *British Journal of Radiology*, vol. 88, no. 1055, article 20150547, 2015.
- [8] J. Zhu, F. Zhang, Y. Luan et al., "Can dynamic contrast-enhanced MRI (DCE-MRI) and diffusion-weighted MRI (DW-MRI) evaluate inflammation disease," *Medicine*, vol. 95, no. 14, p. e3239, 2016.
- [9] D. Ippolito, F. Invernizzi, S. Galimberti, M. R. Panelli, and S. Sironi, "MR enterography with polyethylene glycol as oral contrast medium in the follow-up of patients with Crohn disease: comparison with CT enterography," *Abdominal Imaging*, vol. 35, no. 5, pp. 563–570, 2009.
- [10] D. Ippolito, O. Minutolo, A. Cadonici et al., "Endometrial cancer: diagnostic value of quantitative measurements of microvascular changes with DCE-MR imaging," *Magnetic Resonance Materials in Physics, Biology and Medicine*, vol. 27, no. 6, pp. 531–538, 2014.
- [11] D. Ippolito, C. Trattenero, C. Talei Franzesi et al., "Dynamic contrast-enhanced magnetic resonance imaging with gadolinium ethoxybenzyl diethylenetriamine pentaacetic acid for quantitative assessment of vascular effects on hepatocellular carcinoma lesions treated by transarterial chemoembolization or radiofrequency ablation," *Journal of Computer Assisted Tomography*, vol. 40, no. 5, pp. 692–700, 2016.
- [12] A. Furukawa, T. Saotome, M. Yamasaki et al., "Cross-sectional imaging in Crohn disease," *Radiographics*, vol. 24, no. 3, pp. 689–702, 2004.
- [13] D. H. Kim, L. R. Carucci, M. E. Baker et al., "ACR appropriateness criteria Crohn disease," *Journal of the American College of Radiology*, vol. 12, no. 10, pp. 1048–1057, 2015.
- [14] M. Al-Hawary and E. M. Zimmermann, "A new look at Crohn's disease: novel imaging techniques," *Current Opinion in Gastroenterology*, vol. 28, pp. 334–340, 2012.
- [15] S. M. Lee, W. S. Kim, and Y. H. Choi, "Pediatric magnetic resonance enterography: focused on Crohn's disease," *Pediatric Gastroenterology, Hepatology and Nutrition*, vol. 18, no. 3, pp. 149–159, 2015.
- [16] A. Oto, A. Kayhan, J. T. B. Williams et al., "Active Crohn's Disease in the small bowel: evaluation by diffusion weighted imaging and quantitative dynamic contrast enhanced MR imaging," *Journal of Magnetic Resonance Imaging*, vol. 33, no. 3, pp. 615–624, 2011.
- [17] S. Giusti, L. Faggioni, E. Neri et al., "Dynamic MRI of the small bowel: usefulness of quantitative contrast-enhancement parameters and time-signal intensity curves for differentiating between active and inactive Crohn's disease," *Abdominal Imaging*, vol. 35, no. 6, pp. 646–653, 2010.

- [18] O. A. Hatoum, J. Heidemann, and D. G. Binion, "The intestinal microvasculature as a therapeutic target in inflammatory bowel disease," *Annals of the New York Academy of Sciences*, vol. 1072, no. 1, pp. 78–97, 2006.
- [19] V. A. Pupillo, E. Di Cesare, G. Frieri, N. Limbucci, M. Tanga, and C. Masciocchi, "Assessment of inflammatory activity in Crohn's disease by means of dynamic contrast-enhanced MRI," *La radiologia Medica*, vol. 112, no. 6, pp. 798–809, 2007.
- [20] J. Florie, M. N. J. M. Wasser, K. Arts-Cieslik, E. M. Akkerman, P. D. Siersema, and J. Stoker, "Dynamic contrast-enhanced MRI of the bowel wall for assessment of disease activity in Crohn's disease," *American Journal of Roentgenology*, vol. 186, no. 5, pp. 1384–1392, 2006.
- [21] J. A. W. Tielbeek, M. L. W. Ziech, Z. Li et al., "Evaluation of conventional, dynamic contrast enhanced and diffusion weighted MRI for quantitative Crohn's disease assessment with histopathology of surgical specimens," *European Radiology*, vol. 24, no. 3, pp. 619–629, 2013.